Adhesive mechanisms and the role of positional adjustment on tree frog toe pads

Rick Copier

in partial fulfilment of the requirements of

Master of Science
Mechanical Engineering
Track BioMechanical Design

at Delft University of Technology,
to be defended on Friday April 23, 2021 at 14:00

Supervisors:

Dr. D. Dodou
Dr. ir. A. Sakes
J. Langowski PhD

Graduation Committee:

Dr. D. Dodou
Dr. ir. A. Sakes
Dr. ir. R. van Ostayen
J. Langowski PhD

TU Delft

Paper

Adhesive mechanisms and the role of positional adjustment on tree frog toe pads

Rick Copier

Abstract*—*Objective: **this paper aims to evaluate the adhesive and frictional properties of the keratinised epithelium on the adhesive pads of tree frogs.** ***Modeling methods:*** **two modeling methods have been developed. One of these methods involves the implementation of discrete fibres in a relatively compliant material matrix while the other method involves an anisotropic hyperelastic material model developed by Holzapfel et al. (HGO model). The adhesional and frictional behaviour of an epithelial cell is evaluated for the contact forces at the interface between the adhesive pads and the interface. These forces are dependent on the tree frog behaviour, which consists of proximal pulling on the limbs and adjustments in the body posture and the position of the limbs.** ***Modeling results:*** **a higher fibre density and fibre-matrix bonding is found to increase adhesive performance. An increase in the fibre-matrix stiffness ratio is found to be beneficial for adhesional performance, while an optimum value for this ratio is found for the frictional performance. The modeling results show that the proximal pulling on the limbs by the tree frog without positional adjustment has no significant effect on the adhesive and frictional performance. An adjustment in the body posture and the position of the limbs, however, is found to significantly increase the adhesive and frictional performance.** ***Experimental methods:*** **samples that mimic the tree frog epithelial composite structure are fabricated. These samples consist of a polydimethylsiloxane (PDMS) material matrix in which acrylonitril-butadieen-styreen (ABS) fibres are embedded. Experiments are performed to measure the frictional and adhesive performance of these samples. The experimental results are used to confirm the modelled results on the influence of the fibre-matrix stiffness ratio and the fibre density.** ***Experimental results:*** **for adhesion, the model results are in agreement with the experimental results. For the frictional response, the agreement between the model results and experimental results is less strong.**

Keywords **- biomimetics, bio-inspired adhesives, tree frog, discrete model, HGO model, fibre-matrix composite, fibre-matrix stiffness ratio, fibre density**

I. Introduction

Wall climbing robots have potential applications for tasks at locations that are hard to reach or inaccessible for humans. These robots depend on surface adhesion for locomotion on vertical and inverted surfaces and are often inspired by reversible adhesives found in nature. A well-known example of an animal that makes use of dry adhesion for locomotion is the gecko. Other animals like tree frogs and newts make use of secretion fluids which enable them to use capillary adhesional forces. This paper explores the state of the art of adhesives used for adhesion for robotic applications and explores the adhesive and frictional properties of the adhesive pads of the tree frog which uses wet adhesion. The mechanical properties of the adhesive pads are implemented in a set of models. Furthermore, a set of samples is fabricated in which the same mechanical properties are implemented. At last, the modeling and experimental results are compared to validate the modeling results.

A. Dry adhesion

Robots that utilise bio-inspired adhesives employ mechanical legs, rotating levers or continuous belts on which the adhesive materials are placed. Some of the existing climbing robots are vacuum powered [1]. Other robots, as RiSE [2] Spinybot [3], DROP and LEMUR [4], utilise claws or spines to establish mechanical interlocking with a substrate. Others use magnetic forces [2] or electrostatic forces to achieve adhesion [5]. Most robotic applications make use of Van der Waals forces which requires very close contact between the adhesive pad and substrate. Close contact is achieved using compliant materials such as silicone [6]–[10] or polyurethane rubber [10]–[13], often with a structured or 'hairy' surface to make use of the principle of contact splitting [12], [14], [15]. These adhesives are also direction dependent, which means that they adhere well under shear but easily detach when the adhesive is pulled normal to the substrate [9], [12].

Robotic applications using magnetic, electrostatic or vacuum adhesive pads have a very high power consumption, which limits their usability [4], [8]. Furthermore, suction mechanisms are very sensitive to surface roughness [8], and electrostatic adhesives attract contamination, which reduces adhesional effectiveness. Other adhesives made from soft materials like silicone quickly degrade due to contamination or wear [6], [8], [16].

B. Wet adhesion

The mechanism of wet adhesion has been applied less often in robotic applications. This type of adhesion relies mainly on capillary forces which have a larger working range than Van der Waals forces and thus allow for larger tolerances in the distance between adhesive pad and surfaces. These larger tolerances reduce the need for a pre-load which is often used in dry adhesional applications to reduce the distance between substrate and adhesive [17]. The adhesional liquids involved

in wet adhesion are also described [18], [19] to 'flush' the surface of adhesive pads which reduces pad degradation due to contamination.

Other applications are inspired on the adhesive pads of insects [17], [20], tree frogs [21] or newts [22]. The biomimetic pads of these applications are made from compliant materials to increase the surface area of the pads and some applications incorporate channels in the pad surface to drain excess liquids [21], [22]. Other applications [20] incorporate internal fibres to increase compliance and stress transfer.

C. Tree frog adhesion

To implement the adhesional mechanics of the tree frog in the models and samples described in this paper, it is important to be acquainted with the morphology and material properties of the tree frog adhesive pads. Furthermore, the positional adjustments of the tree frog which are argued to contribute to the adhesive performance, are also described. At last, a tree frog inspired adhesive is discussed which is used to validate the modeling result described in Section III.

C.I. Morphology

Tree frogs secrete a watery mucus which contributes to their adhesional performance [18], [23]. Studies show that both viscous forces and surface tension are likely to contribute to the adhesional performance of the tree frog [24]–[26]. Adhesional performance is also dependent on the compliance of the adhesional pads [27], [28]. Adhesional pad compliance is dependent on the morphological properties of the adhesive pads. The morphological properties of the terminal digits for various species of tree frogs described in the literature are very similar: it is usually not possible to identify the tree frog species from the appearance of the toe pads [29]. The morphological properties considered in this paper are from observations on the *Litoria Caerulea White* by Scholz, Barnes and Nakano et al. [29]–[31], on the *Osteopilus Septentrionalis* by Hanna et al. [24], on the *Hyla Cinerea* by Ernst and Langowski et al [32], [33] and on the *Staurois Parvus* by Drotlef et al. [34].

The specialised adhesive pad epithelium of the *Hyla Cinerea* is 10-15 [μm] thick and delineated from the normal skin by distinct grooves [27], [32], [33]. The epidermis consists of 4-6 layers of columnar epithelial cells. The outermost layer is non-living and consists of polygonal epithelial cells [24], [35], [36]. Most of these are hexagonal but pentagonal, heptagonal and octagonal epithelial cells are also observed [34]. Between these cells, a network of channels exists [31], [33], [34]. The channels measure about 1-2 [μm] in width and 10 [μm] in depth. These channels have been hypothesized to drain excess liquids. Another channel runs around the adhesive pad and is argued to drain excess ambient liquids around the pad to prevent excessive wetting of the pad [37].

The structure of the second cell layer is very similar to the structure of the outer cell layer [32], [33]. This layer becomes the outer layer when the first layer has worn of. An epithelial cell as shown in Figure 2 has a diameter of approximately 13 [μm] [27] and contains keratin fibrils which are oriented distally for most tree frog species. It has been argued that the angling of the keratin fibris provides directional dependent properties [32]. The nanopillars on top of the epithelial cells are formed from the end of the keratin filaments and (partly) fill these structures. The keratin filaments arguably increase the stiffness and the wear resistance of the epithelial cells [38].

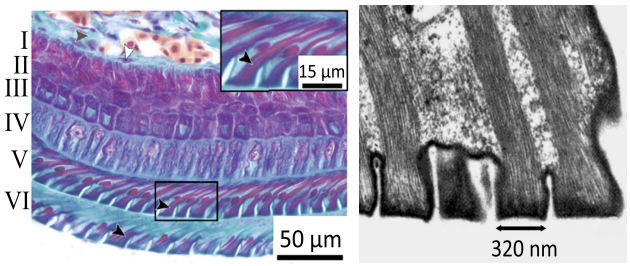

(a) (b)

Fig. 1: The epidermal structure to the level of the epithelial cells. In (1a), a magnified view of the ventral epidermis is shown in which the cellular layers are numbered with I-VI. The fibrillar structures have a reddish colour and are indicated with black arrows. In (1b), a micro-pillar with the internal keratinous structure is shown. Adapted from Langowski et al. and Ernst et al. [32], [33]

The surfaces of the epithelial cells are covered with closely packed columnar nanopillars as is shown in Figure 1b. These pillars measure 200-350 [nm] in diameter and 300-500 [nm] in height for the frog species *Osteopilus Septentrionalis* and *Staurois Parvus* [24]. The nanopillars of the *Litoria Caerulea* measure approximately 22 [nm] in diameter and in height [29], [31]. The top surface of the nanopillars is described to have a slight depression or 'dimple' [30], [39] which

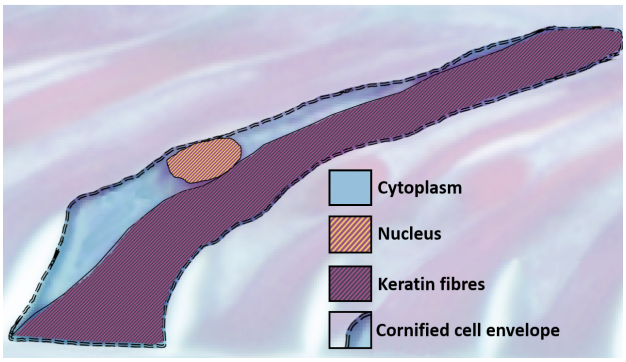

Fig. 2: Epithelial cell with cell components. Adapted from Langowski et al. [32]

measures 6-8 [nm] in depth. The edges of these dimples are interrupted with channels which connect the dimples with channels between the nanopillars. These channels are connected with the channel network between the epithelial cells. The nanopillars are described to contribute to the frictional and adhesive properties of the adhesive pads [18], [30], [35], [40], [41] by the establishment of close conformation to substrate irregularities.

C.II. Material properties of the adhesive pad

The properties of the materials present in the epidermal structure of the tree frog are reported to be dependent on the age of the animal [29] and are likely to be dependent on the species and living environment [42]. Actual measurements of the mechanical properties of the tree frog adhesive are described in several studies [27], [29], [30], [38], [39] as is shown in Table I. The deviation between the values in this table, however, is significant. The stiffness values reported by Barnes et al. are considered the most reliable because:

- The stiffness values reported in the three papers by Barnes et al. are all in the same range while each paper reports another theoretical model to calculate the stiffness values from the measured data.
- The paper published in 2011 describes that the tested samples were tested at an indentation frequency that was low enough to eliminate viscoelastic effects.
- The paper published in 2013 gives the stiffness of the epithelial layer of two different frog species. These stiffness measurements are of the same order of magnitude for both species.

The stiffness measurements from the studies of Barnes et al. give an order of magnitude for the stiffness of the epithelial layer of the tree frog. These stiffness measurements, however, need to be approached carefully because some of the measurements are obtained for relatively small indentation depths (0.2 [μm]) which makes them sensitive to surface irregularities. Furthermore, the indentation measurements do not apply tensile loading to the keratinous fibres which arguably decreases the measured stiffness compared to a stiffness measurement that applies a tensile load on the fibres.

The stiffness measurements on the tree frog can be compared to other stiffness measurements performed on animal tissue. These mechanical properties of tissue depend on the type of protein from which the tissue is composed and the level of hydration. The space between the keratinous fibres is probably filled with connective tissue. Common components of connective tissue in bio-structures are collagen and elastin [43], [44]. The material properties of collagen and elastin are listed in Table II.

TABLE II: Stiffness values for animal connective tissue.

Origin	Elastic modulus [GPa]	Source
Collagen, rat tail tendon	3.75	[45]
Collagen, bovine Achilles tendon	9.0	[46]
Collagen, rat tail tendon	0.1-0.36	[47]
Collagen, bovine Achilles tendon	0.002-0.2	[44]
Bovine elastin	0.00041	[48]
Bovine elastin	0.0011	[49]

The fibres in the epithelial cells are composed of keratin. Table III provides an overview of some stiffness values found in the literature for this material. Keratin can be classified as α-keratin which is found in mammals or as β-keratin which is found in birds and reptiles [50]. The properties of keratin in birds and reptiles are therefore considered representative of the keratin properties of the fibres in the epithelial cells.

TABLE III: Stiffness values for animal and human keratin. The lower three rows give the stiffness values of β-keratin.

Origin	Elastic modulus [GPa]	Source
Horse-hoof	0.41-14.6	[51]
Sheep wool	7-47	[52]
Human keratinocyte cytoskeleton	1.2e-4 3.4e-4	[53]
Birds claw	1.84	[50]
Birds feathers	2-5	[54]
Gecko setae	1.5	[55]

The stiffness values found in the literature for collagen are relatively close to the stiffness values found for keratin. The stiffness of these materials, however, can be severely

TABLE I: Measurements and results from indentation experiments described in literature. Adapted from Langowski et al. [28].

Species	Setup	Diameter indentor [μm]	Indentation depth [μm]	Frequency [Hz]	Indentation velocity [μm]	Stiffness mean value [kPa]	Work of adhesion [J/m^2]	Source
Litoria Caerulea	Whole frog with restricted limbs, temporally anesthetized		1.6	1-2	3.2-6.4	5.7e3		Scholz 2009
Litoria Caerulea			50-350			12		Barnes 2005
Litoria Caerulea	Whole frog with restricted limbs, temporally anesthetized	1500	350	1/35, 5 s relaxation time	23	4.45	0.08	Barnes 2011
Litoria Caerulea	Toes removed from frogs	0.04	0.2	0.5		33.5		Barnes 2013
Rhacophorus Prominanus	Toes removed from frogs	0.04	0.2	0.5		28.7		Barnes 2013

influenced by the degree of hydration. Grant et al. describes a range of 2-200 [MPa] for bovine collagen in varying solution conditions [44] and Bertram et al. [51] describes a range of 0.41-14.6 [GPa] for the stiffness of horse-hoof keratin. The stiffness measurements on hairs, claws, feathers and setae as shown in Table III are all obtained from dead and relatively dry materials. The difference in stiffness between these materials and the keratinocytes can also be explained by the difference in hydration between the living keratinocytes and the dead keratinous materials. The keratinous fibres in the epithelial cell consist of concentrated keratinous material in which no cellular structures are visible which would indicate the presence of keratinocytes. The stiffness of the keratinous fibres is therefore expected to be in the range of 1-10 [GPa].

The exact composition of the connective tissue between the fibres in the tree frog epithelial layer is not reported in the literature. Based on the stiffness values shown in Table II, the stiffness of the connective tissue between the keratin fibres is probably somewhere in between the stiffness values measured on well-hydrated collagen and elastin. The effective stiffness of the connective tissue is estimated at a range of 1-10 [MPa].

C.III. Behavioural analysis

A study performed by Endlein et al. [35] shows that tree frogs actively change their position to a sprawled position by lateral extension of the legs when higher adhesional performance is required. Positional adjustment is described to involve two stages as is shown in Figure 3 and is argued to reduce the substrate-pad contact angle and to increase the lateral forces at the contact interface. The magnitude of the forces involved in the proximal pulling is described to reach a maximum value of approximately one-fifth of the tree frog body weight, measured after the second spread of the tree frog.

(a) (b) (c)

Fig. 3: Stages in the limb spreading of the tree frog on inclined surfaces with in (3a) the initial position of the resting frog. The first spread of the frog is shown in (3b) and the second spread of the frog in (3c). The marks in (3c) show the attachment points. Adapted from Endlein et al. [35].

C.IV. Tree frog inspired adhesive

From all the biomimetic adhesives described in the literature, the adhesive described by Xue et al. [56] is found to be the only tree frog inspired adhesive in which relatively stiff fibres are embedded in a compliant material matrix. Xue et al. found a lower stress magnitude at the interface between adhesive pad and substrate for a composite material in which the base material and the fibres are strongly bound compared to a composite material with lower fibre-matrix bonding. Furthermore, the maximum interface stress for the well-bounded composite was found to be located a certain distance (1-2 rows of pillars) from the material edge, as shown in Figure 4. A composite material in which the fibres are not bound to the base material was found to have a maximum interface stress magnitude on the edge of the geometry as is also the case for homogeneous materials. For a certain magnitude of the stress peak, the adhesive bond between the substrate and the material breaks. The adhesive bond therefore benefits from an equal stress distribution at the material-substrate interface.

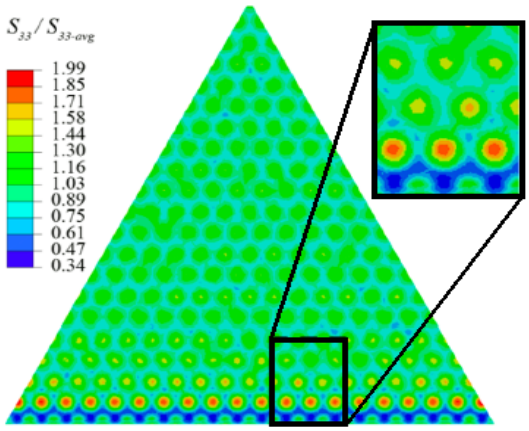

Fig. 4: The stress distribution as a result of good fibre-matrix bonding. The largest stress magnitude was found at the tips of the fibres. Adapted from Xue et al. [56]

D. Goal & Approach

This study focuses on recreating the mechanical behaviour present in the epithelial cell of the tree frog. The research question is *'Do the tilted embedded keratin fibres in the epithelial cells and nanopillars prevent the development of stress concentrations on the adhesive pads of the tree frog?'*

To investigate how the stress is distributed in an epithelial cell and how this distribution affects the stress distribution at the pad-substrate interface, the mechanical properties of the epithelial are evaluated for variations in the fibre-matrix stiffness ratio, the fibre-matrix bonding and the fibre density. To model the mechanical behaviour of the epithelial cell and the micro-pillars, a set of models is implemented in Comsol Multiphysics. The properties and purpose of the different models used are shown in Table IV.

The implementation of the modeling steps shown in Table IV is discussed in Section II. The results of these models are described in Section III. The modeling results are validated

with a set of experimental results. The fabricated samples and the experimental setup used to obtain these results is discussed in Section IV. The experimental results are discussed in Section V.

TABLE IV: Different models, model purposes, boundary conditions and loading configurations used to model the frictional and adhesive performance of the epithelial cell.

Model	Model purpose	Loading & boundary conditions
I: Simplified geometry, discrete fibres	Evaluate influence of: - The fibre-matrix stiffness ratio - The fibre-matrix bonding - The fibre density	Simplified normal & tangential loads
II: Fabricated sample geometry, discrete fibres	Evaluate influence of experimental boundary conditions & predict experimental results	Experimental loading conditions
III: Simplified geometry, HGO model	Validate HGO model	Simplified normal & tangential loads
IV: Epithelial cell geometry, HGO model	Evaluate stress distribution in epithelial cell	Loads derived from tree frog weight and posture

II. Modeling: methods

This section first discusses the implementation of a simplified model with a discrete fibre geometry (model I from Table IV) which was used to evaluate the effect of the fibre-matrix stiffness ratio, the fibre-matrix bonding and the fibre density on the frictional and adhesive performance. The implementation of model II also involved a discrete fibre geometry but required another set of boundary conditions to predict the outcome of the experimental results.

For model III, the same simplified geometry as used for model I was implemented. Model III used the HGO material model and validated the use of the HGO material model for further use in model IV. The purpose of model IV was to evaluate the adhesional and frictional performance of the epithelial cell under loading conditions which were dependent on the tree frog behaviour. An analysis on the effect of the frog behaviour on the substrate-pad interface forces was carried out to determine these loading conditions.

A. Discrete fibre models: model I

Model I was used to evaluate the effect of the fibre-matrix stiffness ratio, the fibre-matrix bonding and the fibre density on the frictional and adhesive performance.

A.I. fibre-matrix bonding

The inter-fibre space in the tree frog epithelium is filled with connective tissue. The exact composition of this tissue and the degree of bonding with the fibres is not exactly clear. Given the well-hydrated nature of the epithelial layer, however, the connective tissue can be safely assumed to be relatively compliant compared to the keratinous fibres [44] which would result in relatively low resistance to inter-fibre sliding.

A thin elastic layer was added at the fibre-matrix interface. The stiffness of this layer was determined with the ratio $R_k = \frac{k_i}{k_f}$ with k_i for the stiffness of the thin elastic layer and k_f for the fibre stiffness. For $R_k = 1$ the thin layer had the same stiffness as the fibres while for $R_k << 1$, the thin layer was relatively compliant compared to the surrounding materials.

The bonding of the fibres to the surrounding tissue can also be discontinuous along the fibre length. This effect was introduced by fixing the fibre-matrix bonding at the tips of the fibres at $R_k = 1$ while varying the fibre-matrix bonding along the rest of the fibre-matrix interface.

A.II. fibre-matrix stiffness ratio

The fibre-matrix stiffness ratio R_s was varied in three steps from $R_s = 1$ to $R_s = 100$. The Young's modulus of the fibres in the discrete fibre model, E_f was set to $E_f = E_m + R_s E_m$ with E_m for the Young's modulus of the matrix material.

A.III. Boundary conditions

To obtain modeling results that match the mechanical behaviour of the micro-pillars under the epithelial cell, a set of boundary conditions was incorporated in the simplified fibrous model as shown in Figure 5:

- The lower boundary of the domain was fixed since the model assumes static contact with the substrate.
- Forces were applied on the upper boundary as would be the case when the micro-pillars are loaded by the tree frog.
- The upper boundary was free in translation in the x and the y-direction but constrained in rotation. This rotational constraint was derived from the observation that the epithelial cells and their micro-pillars are concatenated and would therefore resist rotation. The rotational constraint introduced a moment that is dependent on the distance H_g between the lower boundary and the plane of the force application.
- Based on the observation that the micro-pillars are separated from their surroundings by a channel network, the left and right sides of the geometry were left unconstrained. The interaction with the mucus present in these channels was not expected to significantly influence the mechanical properties of the micro-pillars.
- The stiffness of the individual epithelial cell components as discussed in Section I-C2 were implemented in the discrete fibre model.
- The simplified fibrous model used a linear elastic material model for the fibres and the base material.
- The size of the gap H_e between the fibre tips and the substrate ensured that contact with the substrate

was established with a continuous domain. This was a simplification of the real situation in which contact is established with the thin cornified cell envelope which is also shown in Figure 2.

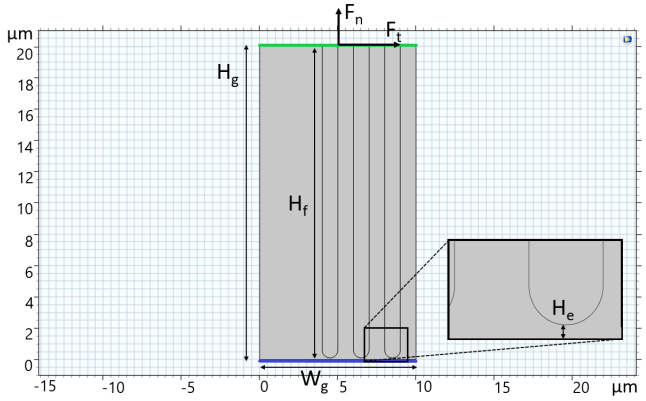

Fig. 5: Geometry and dimensions of the simplified discrete fibre model. The lower boundary is coloured blue, the upper boundary is coloured green and the forces $F_n \& F_t$ represent the normal and the tangential force respectively. The insert shows a close-up of one of the fibre tips. The influence of the degree of fibre-matrix bonding was evaluated with a much denser distribution of thinner fibres than shown in this figure.

A.IV. Model sensitivities

The linear elastic material properties of this model allowed for good model convergence. The smoothness of the solution was dependent on the number of mesh elements, which was set such that the smoothness of the solution was not affected by a further increase in the mesh density.

A.V. Data processing

The frictional and adhesional performance was evaluated in a cut-line just above the lower boundary of the geometry at y = 0.001 [μm]. The data obtained from the model was smoothed with a moving average in the post-processing of the results.

B. Discrete fibre models: model II

The purpose of model II was to approach the experimental setup as close as possible while the other models were focused on approaching the mechanical behaviour in the cells and micro-pillars of the epithelial layer. The mechanisms found with models I, III and IV should also be visible in the mechanical behaviour of model II to use the experimental results for validation of the modeling results.

B.I. Boundary conditions

The main differences between the boundary conditions of model I and model II were:

- The material properties of the fibres and base material were set to realistic values for the ABS fibres and PDMS matrix material. The ABS fibre mechanics were implemented with a linear elastic material model with a Young's modulus of E = 1.19 [GPa], a Poisson's ratio of ν = 0.35 and a density of ρ = 1070 [kg/m^3]. For the PDMS matrix, a two-parameter Ogden hyperelastic material model with nearly incompressible material properties was implemented.
- The shear load on the samples was implemented with a load distribution which equaled the sum of the applied pulling force and the moment caused by this pulling force.

B.II. Model sensitivities

The implemented non-linear material model and the loading configurations led to geometric non-linearity for this model. To prevent convergence issues, the estimates for the initial values of the dependent variables were first determined by implementing an initial modeling step in which relatively small loads were implemented. The response of this initial modeling step was then used to estimate the values of the dependent variables. The non-linear solver configuration was set up with an auxiliary sweep for a step-by-step introduction of the variables which caused the non-linear mechanics.

B.III. Data processing

The results of this model were measured and processed in the same way as for model I.

C. HGO models: model III

The HGO material model allowed the implementation of directional dependent properties and was used to implement the properties of a composite material in a homogeneous domain. The HGO model reduced the number of mess elements needed compared to a discrete fibre model and with that, considerably reduced the computational demands of the model.

C.I. Background: HGO model fundamentals

Fibres in biological materials are often stiffer in tension than in compression [57] and can display strain-dependent or other non-linear material properties. Hyperelastic biological material properties can be described with several material models. Examples of such models are the Neo-Hookean material model [58] and the Mooney–Rivlin model [59].

To implement the properties of the materials present in the epithelial cell of the tree frog, a material model was needed that incorporates the properties of the fibres and the matrix material. The fibre orientation in the keratinous domain of the epithelial cell is location dependent. The material properties are thus direction and location dependent. The HGO model introduced by Holzapfel et al. [60] was used to implement these properties.

The isochoric strain energy density W_s, is defined in Equation 1. The contribution of the matrix and the fibre material is represented by W_1 & W_4 respectively. The contribution of the matrix material is dependent on the stiffness and on the invariant describing the incompressible hyperelastic material behaviour which are represented by C_m and $\overline{I_1}$ respectively.

$$W_s = W_1 + W_4 = \frac{C_m}{2}(\overline{I_1}) - 3) + \frac{k_1}{2k_2}(e^{k_2(I_4-1)^2} - 1) \quad (1)$$

The parameter W_4 is dependent on the stiffness and on the amount of strain stiffening which are represented by k_1 and k_2 respectively. The invariant I_4 which is shown in Equation 2 is dependent on the direction of the fibres and on the local deformation gradient which are represented with the vector field $\mathbf{a} = \begin{bmatrix} a_1 & a_2 & a_3 \end{bmatrix}^T$ and the isochoric elastic Cauchy-Green tensor $\overline{C_{el}}$ respectively.

$$\begin{aligned} I_4 = a_1\overline{C_{el_{11}}}a_1 + 2a_1\overline{C_{el_{12}}}a_2 + 2a_1\overline{C_{el_{13}}}a_3 \\ + a_2\overline{C_{el_{22}}}a_2 + 2a_2\overline{C_{el_{23}}}a_3 + a_3\overline{C_{el_{33}}}a_3 \end{aligned} \quad (2)$$

C.II. fibre-matrix stiffness ratio

The fibre-matrix stiffness ratio for the HGO model was implemented with the parameter $R_{HGO} = \frac{k_1}{C_m}$ and varied using R_{HGO} = 1, 10 & 100.

C.III. Boundary conditions

The boundary conditions of model III were similar to the boundary conditions implemented for model I as shown in Figure 5.

C.IV. Model sensitivities

The HGO material model introduced non-linear behaviour which is countered as described for model II. The results were also influenced by numerical instability which is known as the Runge's phenomenon [61] which causes oscillation at the edges of an interval when a polynomial interpolation is used. To counter this phenomenon, the discretization order of the displacement field was increased.

C.V. Data processing

The results of this model were measured and processed in the same way as for model I.

D. HGO models: model IV

The last model involved a geometry that resembled an epithelial cell. The implemented loads were dependent on the behaviour of the tree frog as discussed below.

D.I. Background: Tree frog behaviour analysis

The forces acting on the epithelial layer of the adhesive pad can be decomposed in normal and tangential forces as shown in Figure 6. The normal forces ($F_{n,1}$&$F_{n,2}$) are determined by the weight and the posture of the frog while the tangential forces ($F_{t,1}$&$F_{t,2}$) are also dependent on the proximal pulling exerted by the frog. The proximal pulling forces are shown in Figure 7.

$F_{n,1}$ and $F_{n,2}$ were defined using static equilibrium. The tangential forces, however, could not be easily determined, because the situation shown in Figure 6 was statically over-constrained. To determine the tangential force components, the mechanical properties of the body which connects the lower and upper attachment points (shown in Figure 6) needed to be known. The tree frog can also manipulate the tangential forces with proximal pulling as discussed in Section I-C3.

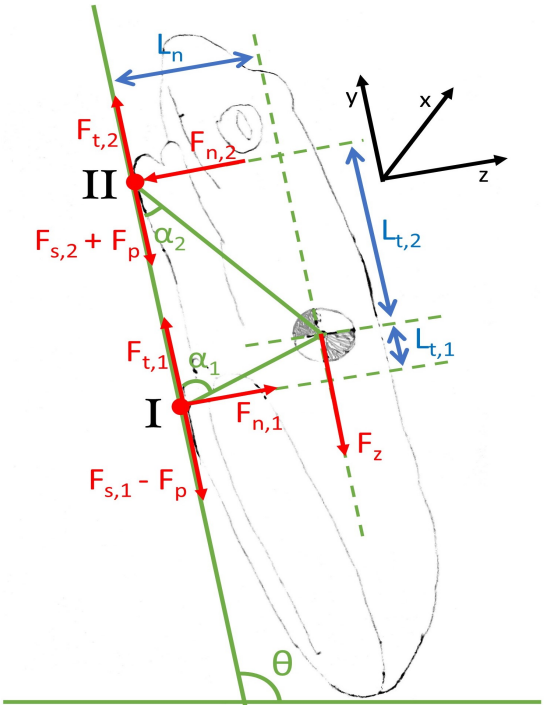

Fig. 6: Diagram of the forces on a tree frog in resting position. The lower and upper attachment points where the frog is attached to the substrate are marked with numbers I and II respectively. The forces are colored red, the angles are colored green and the dimensions are colored blue.

Limb spreading and positional adjustment did also influence the angles of attachment α_1 and α_2 as shown in Figure 6. The tangential forces on the adhesive surfaces of the frog were split up in a component representing the proximal pulling F_p, and in components representing the rest of the tangential force, $F_{s,1}$ and $F_{s,2}$. The relations between these various force components are given by Equations 3-5.

$$F_{t,1} = F_{s,1} - F_p \quad (3)$$

$$F_{t,2} = F_{s,2} + F_p \quad (4)$$

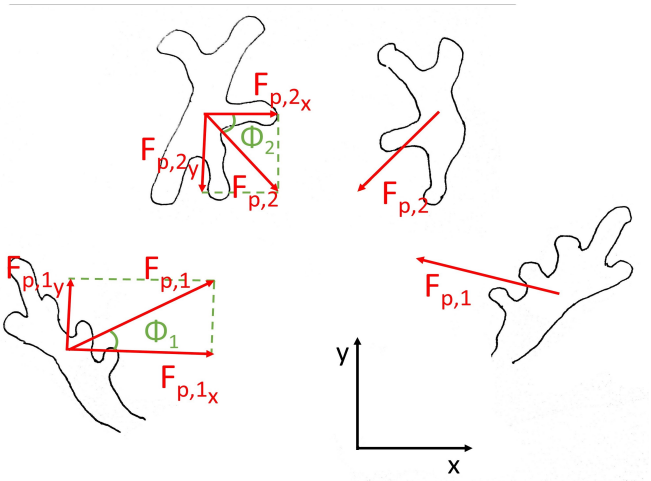

Fig. 7: Forces involved in the proximal pulling of the tree frog for the front limbs ($F_{p,2}$) and the hind limbs ($F_{p,1}$). The proximal pulling forces are decomposed in the x and y-components.

$$F_z = F_{t,1} + F_{t,2} \tag{5}$$

The influence of proximal pulling and positional adjustment was modelled using three different cases which resembled the stages in limb spreading as shown in Figure 3:

- **Case 1** considered the resting position of the frog. The mechanical properties of the frog body connecting the two points of attachment were assumed such that the tangential forces were both equal to half of the tangential component of the gravitational force $F_{t,1} = F_{t,2} = \frac{F_z}{2} cos(\frac{\pi}{2} - \theta)$. The normal forces were calculated using the relations given in Equations 6 & 7.

$$F_{n,1} = \frac{F_z cos(\frac{\pi}{2} - \theta) L_n - L_{t,2} F_{n,2}}{L_{t,1}} \tag{6}$$

$$F_{n,2} = \frac{F_z (L_n cos(\frac{\pi}{2} - \theta) + L_{t,1} cos(\theta))}{L_{t,1} + L_{t,2}} \tag{7}$$

- **Case 2** involved proximal pulling. The magnitude of these pulling forces was derived from the work of Endlein et al. [35] which gives different pulling forces for the first and second spread. The angling of the substrate for which the spreading behaviour was set to occur were θ_1 = 106 [deg] and θ_2 = 131 [deg] for the first and second spread respectively.

- **Case 3** considered a combination of proximal pulling and positional adjustment. The forces for this case are shown in Equations 8-10. As shown in Figure 3, the impact of the positional adjustment was dependent on the angle θ of the substrate. From the observed positional adjustments, an estimate was derived for the change in the dimensions L_{t1} & L_{t2} which determined the position of the tree frog. The dimensions L_{t1} & L_{t2} were multiplied with a factor $\frac{3}{2}$ and parameter L_n was multiplied with a factor $\frac{3}{4}$ for $\theta_1 \leq \theta \leq \theta_2$. For $\theta > \theta_2$, L_{t1} & L_{t2} were multiplied with a factor 2 and the parameter L_n was multiplied with $\frac{1}{2}$. The parameter $R = \frac{1}{5}$ resembles the ratio between the body weight of the frog and the magnitude of the proximal pulling force as discussed in Section I-C3. The parameter ϕ_1 is the angle of the proximal pulling force as shown in Figure 7.

For $\theta < \theta_1$,

$$F_{p,1_x} = F_{p,2_x} = F_{p,1_y} = F_{p,2_y} = 0 \tag{8}$$

For $\theta_1 \leq \theta \leq \theta_2$,

$$F_{p,1_x} = F_{p,1_x} = F_z \frac{R}{4},$$

$$F_{p,1_y} = tan(\phi_1) F_{p,1_x} \quad \& \quad F_{p,2_y} = tan(\phi_1) F_{p,2_x} \tag{9}$$

For $\theta > \theta_2$,

$$F_{p,1_x} = F_{p,1_x} = F_z R,$$

$$F_{p,1_y} = tan(\phi_1) F_{p,1_x} \quad \& \quad F_{p,2_y} = tan(\phi_1) F_{p,2_x} \tag{10}$$

The forces at the contact interface for the third case are shown in Figure 8. The normal force components were considerably influenced by the proximal pulling and positional adjustment while the tangential force components were only slightly influenced.

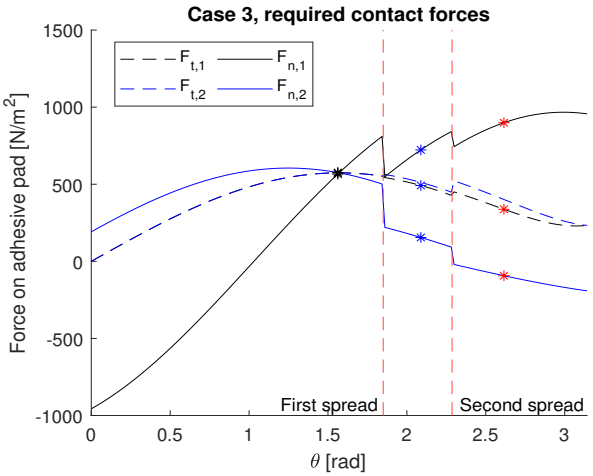

Fig. 8: Required contact forces as a function of the the angle θ for Case 3. The black, blue en red dots which are placed at θ_1 = 90 [deg], θ_2 = 120 [deg] and θ_3 = 135 [deg] indicate the forces implemented in model IV.

D.II. fibre-matrix stiffness ratio

The fibre-matrix stiffness ratio for this model was implemented in a similar way as for model III.

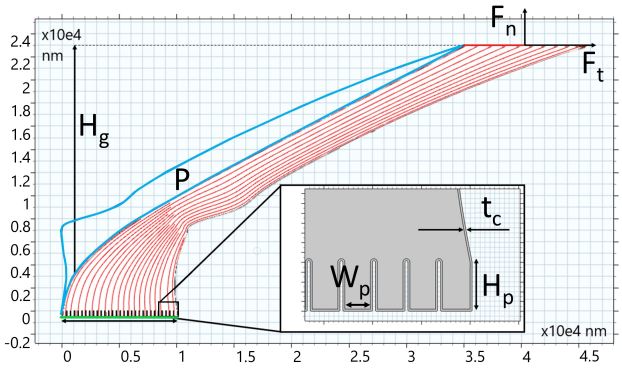

Fig. 9: The dimensions and boundary conditions of the model that resembled the epithelial cell. The lower boundary is coloured green, the upper boundary is coloured red. The forces F_n&F_t were applied on the upper boundary. The blue boundaries enclose the lymph space and P indicates the pressure in the lymph space. H_g and W_g represent the height and base width of the epithelial cell respectively. The epithelial cell is enclosed by a cornified cell layer with thickness t_c. The epithelial cell has a total of 30 micro-pillars. The height and width of each of these pillars are represented by H_p and W_p respectively. The red streamlines indicate the direction of the vector field **a** implemented in Equation 2.

D.III. Boundary conditions

The boundary conditions and loading configurations of model IV, as also shown in Figure 9, were as follows:

- The lower geometry boundary, highlighted in green in Figure 9, was fixed.
- The upper boundary was loaded with the forces F_n&F_t. This loading configuration was a simplification of the real loading configuration in which the loads would be more evenly distributed over the material domain.
- The distance in the x-direction between the upper and lower boundaries could cause a large deformation in the y-direction when a normal force was applied. In reality, however, the space under the epithelial cell is filled with other cells which will resist such deformation. To resemble the mechanics of the neighbouring cells, the lower boundary was subjected by a force per unit area in the x and y-direction. The magnitude of these constraining forces was determined with Equations 11 & 12. The local displacement in these equations is represented by u and v. L = 10 [μm] represents an estimate of the maximum displacement and E_s = 100 [kPa] represents the Young's modulus of the surrounding cellular material. The value of E_s was derived from the indentation experiments performed by Barnes et al. as can be seen in Table I.

$$\sigma_{xx} = \frac{-u}{L} E_s \tag{11}$$

$$\sigma_{yy} = \frac{-v}{L} E_s \tag{12}$$

- The upper boundary of the cell (in red in Figure 9) was constrained in rotation as is also discussed for models II & III.
- The contents of the lymph space was assumed to be incompressible. The pressure P on the boundaries of the lymph space was therefore determined with the relation $P = A - A_0$ which is dependent on the initial undeformed area of the domain A_0 and on the variable area A of the domain.
- The mechanical properties implemented for the cornified cellular layer were based on the assumption that this relatively thin layer (10 [nm]) has linear elastic properties with a Young's modulus of 100 [MPa], a Poisson ratio of 0.4 and a density of 1000 [kg/m^3]. These properties were later varied to evaluate the influence of the stiffness of the cornified cell envelope.
- The mechanical properties of the fibrous domain were implemented with the HGO model. Based on the stiffness values described in Section I-C2, the material stiffness of the base material, which is represented by the parameter C_{10} was set to C_{10} = 100 [kPa]. The value of k_2 was kept constant at k_2 = 1 and the value of k_1 was varied to evaluate the influence of the fibre-matrix stiffness ratio.

D.IV. Model sensitivities

The model sensitivities and the measures taken to counter solver non-convergence for this model were similar to the sensitivities and measures described for model III.

D.V. Data processing

The results of this model were measured in a cut-line that was positioned above the micro-pillars in the fibrous section of the epithelial cell. The position of the cut-line is shown in the insert of Figure 15a.

III. Modeling: results

This section describes the model validation and modeling results for each model from Table IV. The discrete fibre models are validated by comparing the results of model I & II with the results obtained by Xue et al., while the results of model III are compared with the results of model I to validate the use of the HGO model. After validation, the influence of the fibre-matrix bonding, the fibre-matrix stiffness ratio and the fibre density on the frictional and adhesive performance is discussed for each model. The results of model IV focus on the influence of the tree frog behaviour on the adhesive and frictional performance of the epithelial cell.

A. Discrete fibre models: model I

A.I. Validation

Figure 10 shows that the stress in the simplified domain of model I is strongly influenced by the location of the fibres.

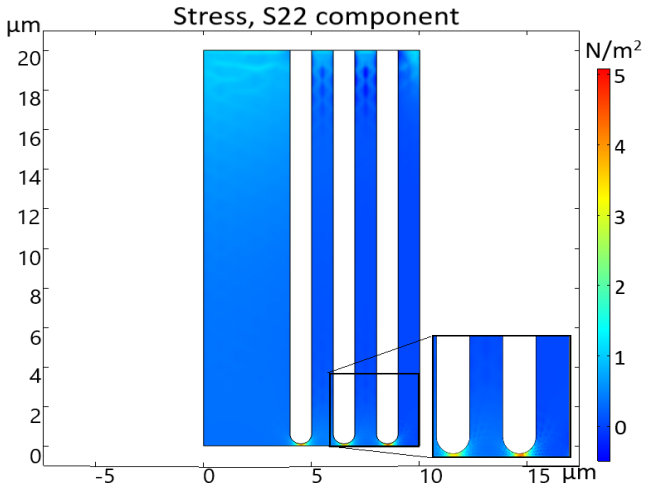

Fig. 10: The S_{22} stress component in a simplified composite model.

Furthermore, the stress in the lower right en left corners is considerably lower compared to the stress in a geometry with similar dimensions and material properties but without the fibres.

Reduction in peak stress magnitude increases the adhesive strength of a material. These observations are in accordance with the results described by Xue et al. as described in Section I-B and validate the use of the simplified composite model for further modeling purposes.

A.II. Fibre-matrix stiffness ratio

The magnitude of S_{11} and S_{22} is the lowest for $R_s = 100$ for a loading configuration that applies the load in the fibre direction as shown for S_{22} in Figure 11a.

For a loading configuration in which the load is applied perpendicular to the fibres, the lowest magnitude of the stress components S_{11} and S_{22} is found for $R_s = 10$ as shown in Figure 11b and is caused by the relatively high stress peak at the location of the last fibre for $R_s = 100$. The stress magnitude at the edge of the domain, however, is found for $R_s = 100$.

A.III. fibre-matrix bonding

The effect of the fibre-matrix bonding is shown in Figures 12a & 12b. When loading is applied in the direction of the fibres, the stress distribution along the lower domain boundary is smoother for $R_k = 1$ compared to $R_k = 1e-6$ both for the models with the fixed tips and for the models involving the free sliding fibres as shown in Figure 12a. The stress magnitude at the edges of the domain is the lowest for the model involving the fixed tips and $R_k = 1e-6$ for the rest of the fibre-matrix interface.

When the geometry is loaded perpendicular to the fibre direction, the magnitude of the stresses in the domain increases due to the non-uniform nature of the response as shown in Figure 12b. The stress peaks just before the edges at the domain are lower for $R_k = 1$. The largest stress magnitude is found for the model involving the fixed tips and with $R_k = 1e-6$.

B. Discrete fibre models: model II

B.I. Validation

This model uses a similar discrete fibre model as is implemented for model I and is therefore validated with the validation described for model I.

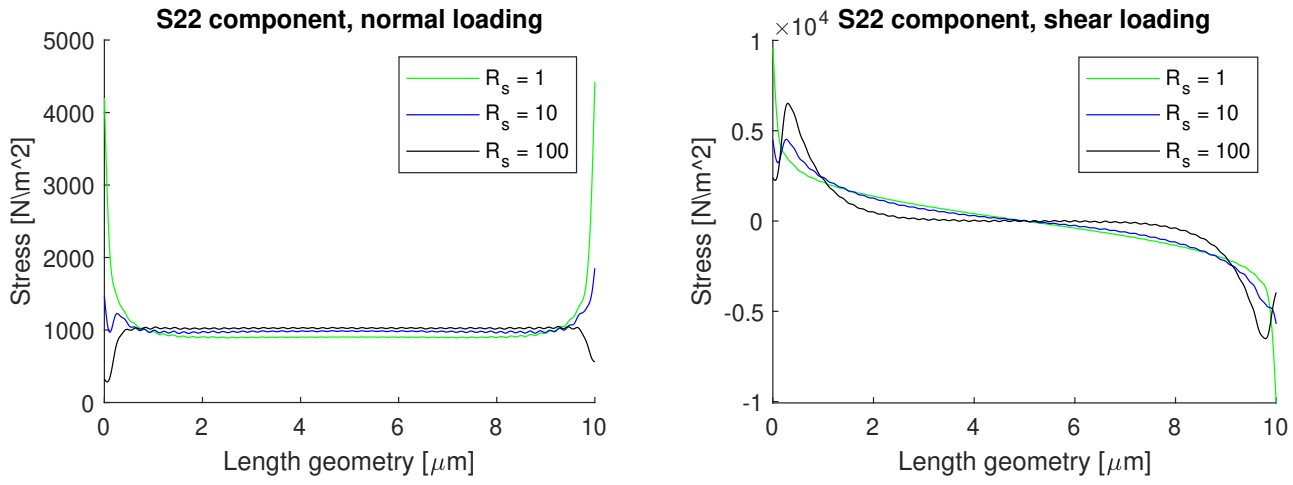

(a) (b)

Fig. 11: The S_{22} component of the response for normal (Fig. 11a) and shear (Fig. 11b) loading configurations of model I.

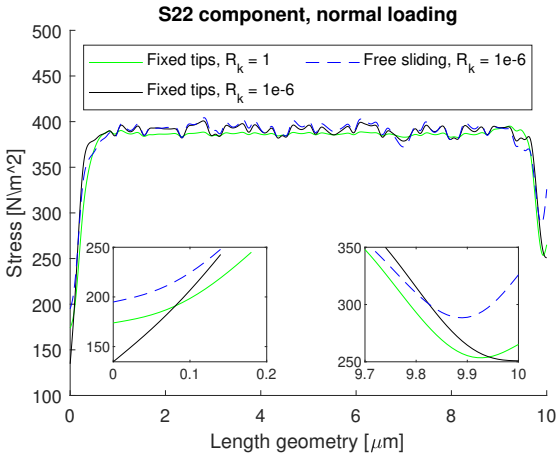

(a)

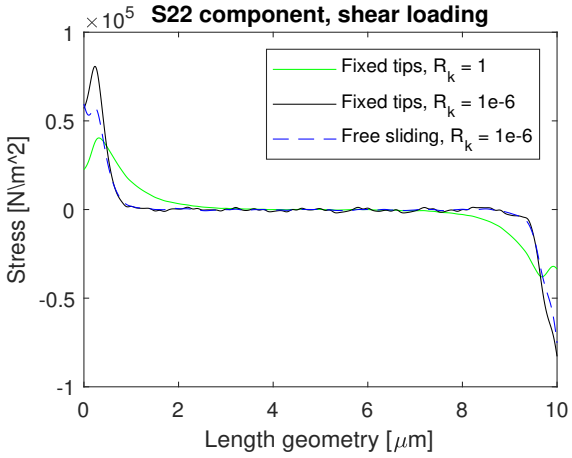

(b)

Fig. 12: The S_{22} component of the response for normal (in Fig. 12a) and shear (in Fig. 12b) loading. The inserts in 12a show the forces at the left and right edges of the domain. The 'free sliding' fibres have a continuous fibre-matrix interface stiffness. For the fixed tips, $R_k = 1$ at the fibre tips while the interface stiffness along the rest of the fibre is varied.

B.II. Fibre-matrix stiffness ratio

This model is used to predict if the effect of the fibre-matrix stiffness could also be expected for the samples used for the experimental results. The results of this model confirm that the influence of the fibre-matrix stiffness ratio, as described above for model I, can also be expected for the samples.

C. HGO models: model III

C.I. Validation

To validate the use of the HGO model properties, the stress response of the HGO model is compared with the response of several other material models which are all implemented in a similar geometry. These models include a coarse fibre model (geometry shown in Figure 10) with linear elastic material properties, a model with a dense pattern of relatively thin fibres with linear elastic properties, a model without fibres and uniform hyperelastic material properties and a model with uniform linear elastic material properties.

Figure 13 shows the moving average of the S_{22} component of the stress response for these models which are all loaded with a force F_n on the upper boundary. This loading configuration loads the fibrous models in the direction of the fibres.

For the HGO material model, the mechanical properties of the fibres and the matrix material are present everywhere in the material domain and can therefore, in theory be approached with a discrete fibre model with infinite thin fibres which are present everywhere in the matrix material. The average stress shown in Figure 13 shows that the stress response of the coarse fibre model is highly dependent on the fibre locations while the response of the thin fibre model is similar to the response of the HGO model. This observation

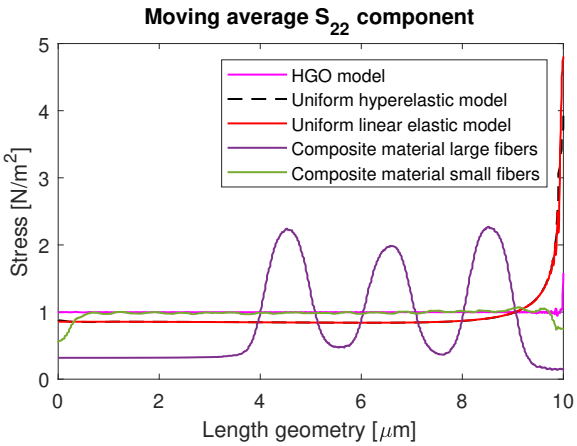

Fig. 13: Moving average of the S_{22} stress component on the lower boundary of the geometry. The response of the uniform material models is added to visualise the effect of the other models on the stress response. The peaks of the HGO model near the right edge of the boundary are caused by numerical instability.

confirms the use of the HGO model to represent the stress distribution of a thin-fibre discrete model.

There are, however, also differences between the response of the HGO model and a thin-fibre model. The largest differences are observed for a shear loading configuration (though the application of a force F_t from Figure 5) which causes a non-uniform loading distribution along the lower geometry boundary with a maximum magnitude at the edges of the domain. The strain stiffening properties of the HGO model cause a non-linear relation between applied loads and stress response. This increases the stress component S_{22} and

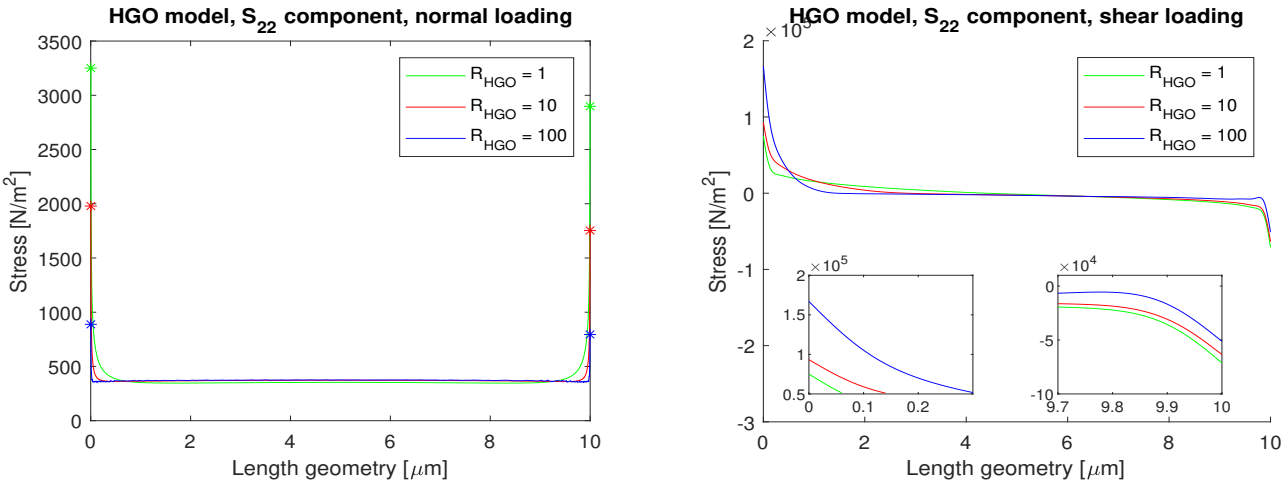

(a) (b)

Fig. 14: The S_{22} component of the response for normal (Fig. 14a) and shear (14b) loading.

reduces the strain at the domain edges. Due to this strain reduction, the S_{11} stress component is reduced at the domain edge.

The discrete fibre models incorporate a layer of matrix material between the domain edge and the fibre that is closest to the domain edge. The matrix material has a relatively low stiffness compared to the fibrous material which causes a reduction in the stress components at the domain edge.

The stress components of the response of the HGO model at locations where the material is loaded in compression are very similar to the response of a homogeneous linear material model. This can be explained by the absence of directional dependent properties for the HGO model when loaded in compression. Without these directional dependent properties, the HGO model acts as a pure solid with a Neo-Hookean material model.

C.II. Fibre-matrix stiffness ratio

The S_{22} component of the stress response upon implementation of a force in the fibre direction is shown in Figure 14a. The results of the HGO model show that a higher fibre-matrix stiffness ratio reduces the stress magnitude when the load is acting in the fibre direction.

For a shear loading configuration, as shown in Figure 14b, the stress at the right edge of the domain differs from the response at the left edge of the domain due to the directional dependent strain stiffening behaviour. The magnitude of the S_{22} stress component at the left corner of the geometry is larger for higher values of R_{HGO}. The observed benefit of a higher fibre-matrix stiffness ratio for the discrete fibre model for both loading configurations is therefore not visible for the shear loaded HGO model. However, due to the strain stiffening effect, the strain at the left edge is reduced and with that, the magnitude of the S_{11} component.

The largest difference between the response of the discrete fibre model and the HGO model is the absence of the stress peak just before the domain edges as shown in Figure 11a.

D. HGO models: model IV

D.I. Validation

This model uses the HGO material model as is implemented for model III and is therefore validated with the validation described for model III.

D.II. Epithelial cell stresses

The mechanical behaviour of the epithelial cell for angle θ_3 is shown in Figure 15. The locations of the stress concentrations in the epithelial cell are shown in Figure 16. A stress concentration is found along the left edge of the domain (number (1) in Fig. 16), which also causes a stress concentration in the left corner of the left most micro-pillar (number (2) in Fig. 16). Such stress concentrations are also observed in the left corners of other micro-pillars that are located in the left side of the epithelial cell geometry (number (3) in Fig. 16).

The stress in the corners of the micro-pillars decreases when the stiffness of the cornified cell layer is set to a lower value than the stiffness of the internal structure of the epithelial cell.

The negative values for the Von Mises stress in the lower right region in the epithelial cell domain (number (4) in Fig. 16) are probably caused by the tension along the left edge of the geometry. For $R_{HGO} = 10$ and for $R_{HGO} = 1$, the magnitude of the stress in the left corner of the geometry is considerably lower than for $R_{HGO} = 100$.

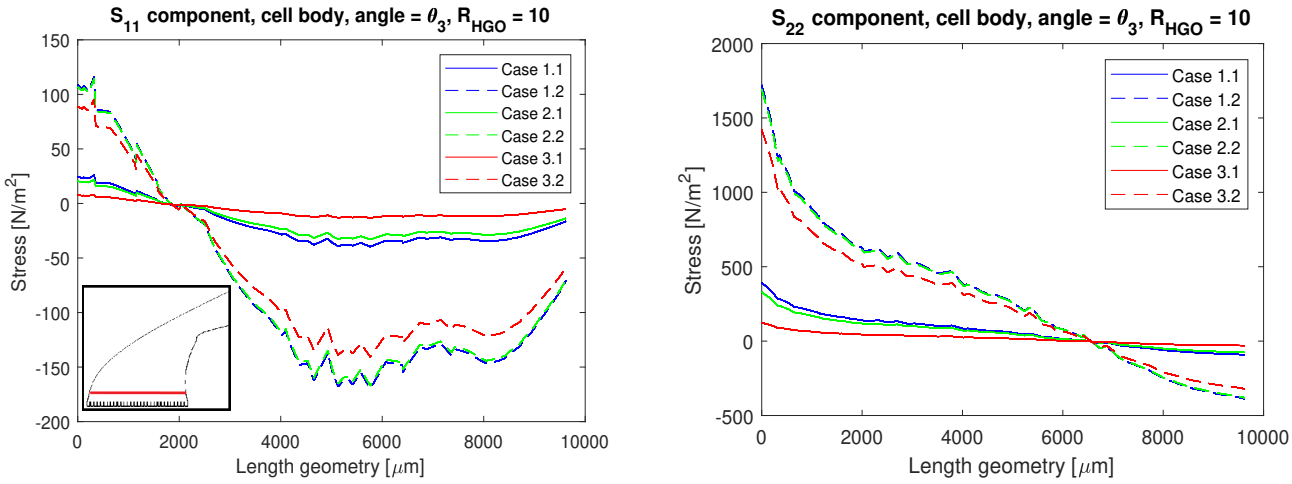

(a) (b)

Fig. 15: Inter-case difference in stress response for the S_{11} (Fig. 15a) and S_{22} (Fig. 15b) stress component. The magnitude of the load on the epithelial cell is shown in Figure 8 and indicated by the red dots on the curves for θ_3. The insert in (Fig. 15a) shows the line in which the response is measured.

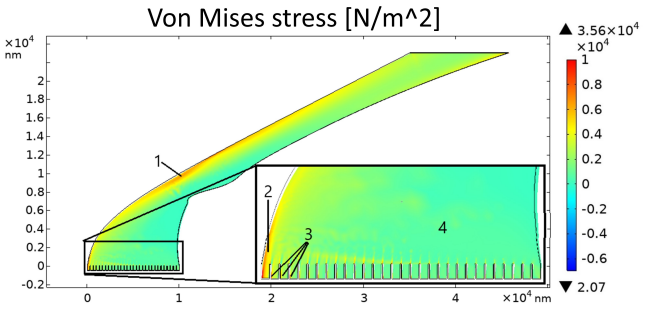

Fig. 16: The Von Mises stress in the geometry of the epithelial cell for $R_{HGO} = 100$. The insert shows a close-up of the bottom of the cell. The stress concentrations are marked with numbers (1)-(4).

D.III. Tree frog behaviour: inter-case differences

The loading cases as defined in Section II-D1 each lead to a stress distribution in the epithelial cell as shown for θ_3 in Figure 15. The main differences between the loading cases are:

1) The highest values for S_{11} are found in the front limb for Case 1.2.
2) The S_{22} stress component is larger for the front limbs (Case 1.2, 2.2, 3.2) when compared to the hind limbs (Case 1.1, 2.1, 3.1). This effect gets stronger when the angle θ is increased.
3) The largest stress magnitude of S_{22} is shown for θ_3 for Case 1.2 in Figure 15b. The magnitude of the S_{22} component for Case 2.2 is only slightly lower than the magnitude found for Case 1.2.
4) The effect of the proximal pulling of the tree frog on the stress response is observed in the difference in the response when comparing the response for Case 1 with the response for Case 2. The difference in the stress response between these cases is relatively small compared to the difference between Case 3 and the other cases.

IV. Experiments: methods

A. Fabrication

The goal of the experiments performed was to validate the modeling results on the influence of the fibre-matrix stiffness ratio and the influence of the fibre density. Six different samples were fabricated as shown in Table V. The matrix material stiffness values in this table are an approximation of the non-linear hyperelastic material 'stiffness'.

The fibres implemented in the samples were cut from 1 [mm] thick ABS material (S-Polytec, Germany) with a Lion Merlin laser system (Lion Laser Systems B.V., The Netherlands). The fibres were attached to a base as shown in Figure 17. The separate parts shown in Figure 17 were glued together (Bison code 6305952, Bison, Goes, The Netherlands). To incorporate the fibres in the base material, a series of moulds was 3D printed using an Ultimaker 2+ (Ultimaker, Geldermalsen, The Netherlands) with Ultimaker PLA filament. The moulds were sanded for a smooth finish. The fibres were then implemented in the silicone elastomer matrix material (SYLGARD® 184, Dow Corning, Midland, USA) which involved a series of steps:

1) A batch of PDMS was thoroughly mixed and poured into the mould until the mould bottom was covered with a layer of uncured PDMS of about 3 [mm] in height. The

TABLE V: Properties, coding and process parameters for the fabricated samples. The mixing ratio is expressed in the (elastomer volume: curing agent volume). The indexes shown for the curing duration and temperature are for the first, second, third and fourth process step respectively.

Sample	Sample coding			Process parameters		
Stiffness	Reference, no fibres	Coarse fibres	Thin fibres	Mixing ratio	Curing time [h]	Curing temperature [$^{\circ}C$]
1 [MPa]	R_1MPa	C_1MPa	T_1MPa	1:10	48,48,[-],48	20,20,[-],20
3 [MPa]	R_3MPa	C_3MPa	T_3MPa	1:5	48,48,72,48	20,20,80,20

PDMS was then degassed in a vacuum chamber until all visible air bubbles were removed. The fibres were inserted in the PDMS and fixated with a series of ABS separator plates. The PDMS was then cured for 48 [h] at room temperature. To prevent sticking, a thin layer of petroleum jelly was applied to the walls of the mould.

2) After finishing the curing of the first step, the partly finished sample was removed from the mould and the ABS separator plates were removed from the assembly. The partly finished sample was then placed in another mould and this mould was filled with degassed PDMS until the final height of the PDMS section of the sample was reached. The setup was again left to cure for 48 [h] at room temperature.
3) This step was only applied for the high stiffness samples and involved a curing cycle in which the sample was cured at 80 [$^{\circ}C$] for 72 [h]. Before curing, the sample was removed from the mould.
4) The purpose of the last step was to smooth the bottom of the sample. The sample was placed on a thin layer of well-mixed and degassed PDMS that was applied on a smooth and clean piece of PMMA. Due to gravity and capillary forces, a thin layer of uncured PDMS remained between the sample and the substrate. The sample was left to cure for 48 [h] at room temperature.
5) The sample was removed from the PMMA substrate and cut to shape.

The mixing ratio of the base component and curing agent and the curing duration and temperature are shown in Table V. Syringes are used to measure the mixing ratio's by volume.

B. Experimental setup

Two measurement setup configurations were used as is shown in Figure 18. The setup consisted of a rigid frame made from aluminium extrusion profiles which was placed on another, wooden frame which accommodated the camera setup (Logitech C920, Logitech, The Netherlands). A Thorlabs Z825B (Thorlabs Inc., United States) linear actuator with a translational stage was used for the linear actuation. The linear actuator had a range of 25 [mm] and was controlled with a KDC101 controller and the Kinesis software. The linear motion of the actuator was transferred to the sample with a nylon wire with a cross-section of 3 [mm]. For shear force application, a pulley was used to guide the nylon wire from the mounting part to the translational stage. The loads were measured with a load cell (Model FLLSB200, Feteris Components, The Netherlands) and the displacement of the actuation stage was measured with a laser range finder (OptoNCDT 1420, model ILD1420-200, Micro Epsilon, Ortenburg, Germany). A 6 [mm] thick glass substrate was connected to the setup with a set of aluminium clamping parts.

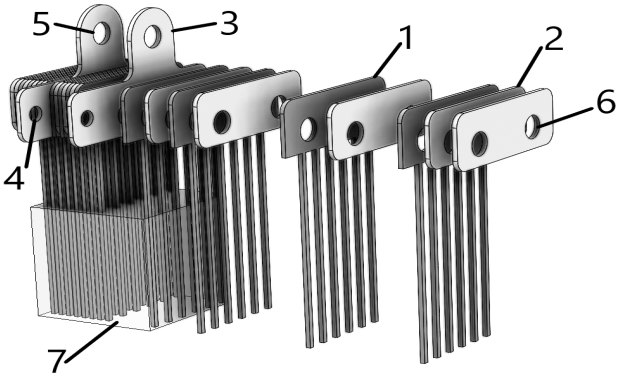

Fig. 17: Fabrication of the coarse fibre samples. The sample is build from single fibrous assembly parts (1). These parts are spaced with separator plates (2&3). Some of these separator plates have attachment points (4&5) for force application. All the parts of the fibrous part of the sample have holes (6) which are used to align the parts which each other during assembly. The fibres is are embedded in a block of PDMS (7) which forms the matrix material.

C. Experimental conditions & procedure

The samples were placed directly on the glass substrate. Preloading was used to ensure the establishment of an initial adhesive bond between the sample and the substrate. Each sample was tested 10 times for both normal and shear loading conditions in randomized order. The measurement procedure for each sample was as follows:

1) A sample was placed on the substrate and preloaded by placing a 500 [gr] weight on the sample for 10 [s].
2) The sample was loaded and the response recorded. The maximum acceleration and velocity of the linear translational stage were set to 0.5 [mm/s^2] and 0.5 [mm/s] respectively.
3) The sample was cleaned after separation from the substrate. The bottom of the sample was first rinsed using a paper towel and alcohol. The sample was subsequently rinsed with tap water and left to dry.

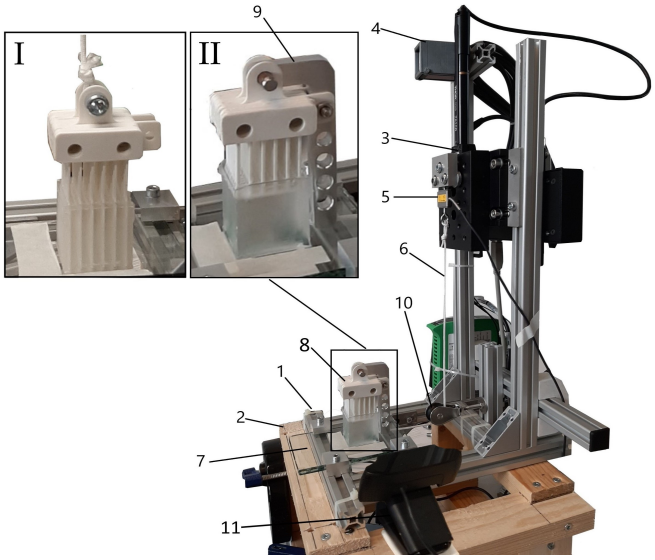

Fig. 18: The measurement setup consisted of an aluminium frame (1) placed on a wooden base frame (2) which enabled the installation of camera's (11). The samples (8) were placed on a glass substrate (7). The forces from the motorized translational actuator (3) were transferred to the sample with a nylon wire (6). A laser distance sensor(4) was used to measure the displacement of the translational stage and a load cell (5) was used to measure the force on the sample. Insert (I) shows the direct attachment of the wire to the top of the sample for adhesive force measurements and insert (II) shows the L-shaped mounting part (9) used for the friction force measurements. For the friction force measurements, a pulley (10) is used to redirect the nylon wire.

4) The substrate was cleaned with alcohol when all six samples were tested. Additional cleaning was performed when the substrate was visually polluted.

D. Data processing

The experimentally obtained data was processed using Matlab 2020b. An one-way Anova analysis with $DoF_1 = 1$, $DoF_2 = 18$, $p < 0.05$ and $F_{ref} = 4.41$ was used to determine the effect of the independent variables.

Some of the elements of the measurement setup such as the nylon wire and the load cell, were relatively compliant compared to the samples and the other elements of the measurement setup. The compliance of these elements influenced the measured force-displacement ratio. The measured data was calibrated to compensate for this deviation in the measurements.

V. Experiments: results

The maximal adhesional and frictional forces measured for the samples is shown in Figure 19. The statistical interpretation of the differences between the different samples and loading configurations is shown in Table VI. In section V-C, some observations are described which give additional information on the sample degradation, the sample deformation and the sample detachment.

A. Fibre-matrix stiffness ratio

A.I. Adhesion force measurements

The differences between samples *R_1MPa* & *R_3MPa*, *C_1MPa* & *C_3MPa* and *T_1MPa* & *T_3MPa* show the influence of the matrix stiffness for samples with a similar fibre configuration. The samples with the 1 MPa matrix stiffness exhibited significantly higher adhesional forces compared to the samples with the 3 MPa matrix material stiffness.

A.II. Friction force measurements

For the shear loading, the measured frictional forces are shown in Figure 19b. For the 1 MPa matrix stiffness samples, the difference in the measured forces is the lowest between sample *R_1MPa* and *T_1MPa*. The highest friction force is measured for sample *R_1MPa* and the lowest friction force is measured for sample *C_1MPa*.

B. Fibre density

B.I. Adhesion force measurements

For the normal loading of the samples with the 1 MPa matrix stiffness, sample *C_1MPa* exhibited a higher adhesional force than sample *R_1MPa*. Sample *T_1MPa* has the highest adhesional force response in the normal direction among the samples with the 1 MPa matrix stiffness.

For the normal loading of the samples with the 3 MPa matrix stiffness, sample *R_3MPa* exhibited the highest adhesional force. The difference between sample *R_3MPa* & *C_3MPa* is relatively low as can be seen in Table VI. Furthermore, it should be noted that the measured forces for sample *C_3MPa* are lower than the forces measured for sample *R_3MPa* and *T_3MPa*.

B.II. Friction force measurements

The frictional forces measured for the 3 MPa matrix stiffness samples and the 1 MPa matrix stiffness samples show a similar pattern: the highest friction forces are measured for both the reference samples. The measured forces for the thin fibre samples are slightly lower compared to the reference samples. The measured forces for the coarse fibre samples are significantly lower compared to the reference samples and the thin fibre samples.

The difference in the measured friction force among the high base stiffness samples (row 4-6 in Table VI) is relatively low compared to the difference in force response among the low base stiffness samples (row 1-3 in Table VI). This is arguably caused by the outliers in the data for the frictional

force measurements for sample *C_3MPa*.

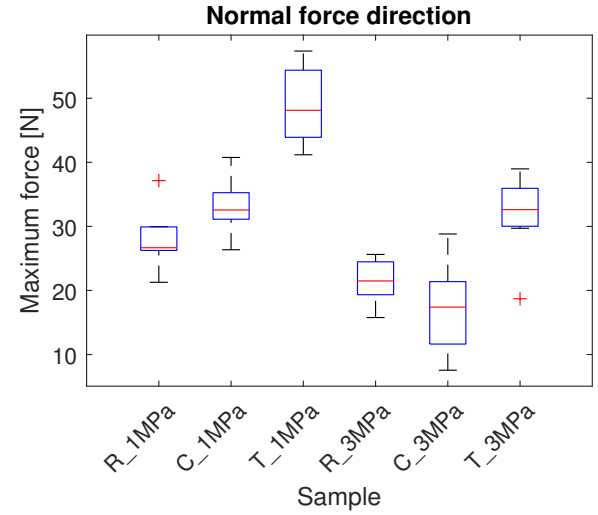

(a)

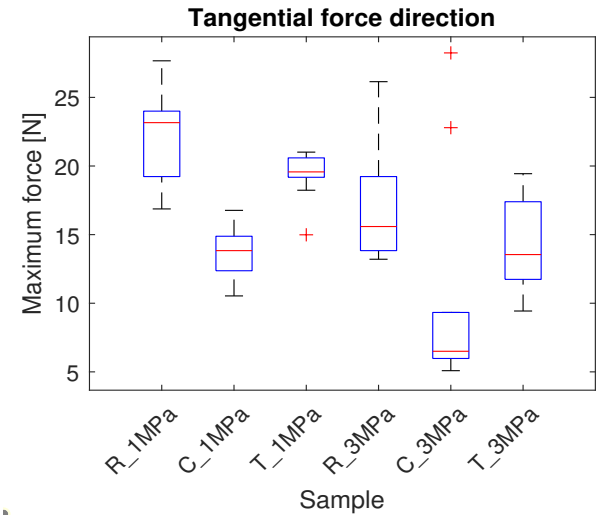

(b)

Fig. 19: Boxplots that show the experimental data obtained for the normal (Fig: 19a) and shear loading configurations (Fig: 19b) measurements.

C. Experimental observations

C.I. Sample degradation

The samples were directly placed on the substrate and were therefore dependent on the smoothness of the sample-substrate interface which could degrade with the number of testing cycles performed on the samples. As could be visually observed, the cause of the sample degradation was the detachment of the layer applied in the fourth fabrication step as described in Section IV-A. For the 1 MPa matrix stiffness samples, a gradual decline in performance was observed with the number of testing cycles performed. The degradation in performance observed for the 3 MPa matrix stiffness samples was even more significant. The largest degradation in performance is observed for sample *C_3MPa* for normal and shear loading configurations as shown in Figure 20.

TABLE VI: Statistical significance of the difference in force response between the different samples. The one-way Anova method is used to determine the parameters p & F.

Samples	Adhesion measurements		Friction measurements	
	p	F	p	F
R_1MPa & T_1MPa	2.0008e-08	89.9742	0.0224	6.2407
R_1MPa & C_1MPa	0.0090	8.5555	1.8139e-06	47.8765
C_1MPa & T_1MPa	7.7069e-07	54.3332	3.4435e-06	43.4297
R_3MPa & T_3MPa	6.5175e-05	26.6680	0.1131	2.7738
R_3MPa & C_3MPa	0.0728	3.6327	0.0321	5.3950
C_3MPa & T_3MPa	2.7426e-05	31.0408	0.1765	1.9792
R_1MPa & R_3MPa	0.0011	14.9473	0.0113	7.9558
C_1MPa & C_3MPa	2.2270e-06	46.4182	0.1989	1.7791
T_1MPa & T_3MPa	2.7338e-06	44.9942	3.9398e-04	18.8410

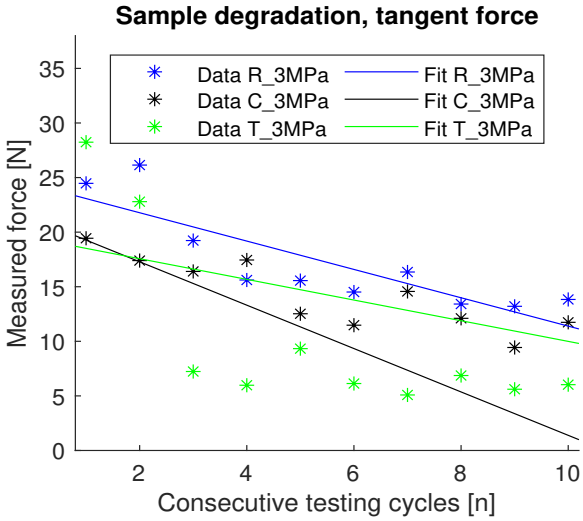

Fig. 20: Sample degradation visualized as the measured response for consecutive tests of the 3 MPa matrix stiffness samples for tangential loading.

C.II. Sample deformation

For the tangential loading conditions, there is a difference between the deformation of the samples as shown in Table VII. The stiffness of the reference samples is higher than the stiffness of the fibrous samples. The samples with the coarse fibres have a higher resistance to deformation than the samples with the thin fibres.

C.III. Sample detachment

The detachment of sample *T_1MPa* for tangential loading conditions is shown in Figure 21. For normal and tangential loading conditions, detachment for sample *T_1MPa* is initialized at the fibre tips after which the detached area grows until full detachment occurs. At the lower right

TABLE VII: Calibrated deformation and average stiffness of the samples measured for tangential loading configuration.

Sample	R_1MPa	C_1MPa	T_1MPa	R_3MPa	C_3MPa	T_3MPa
Deformation [mm]	9.642	6.947	12.131	12.040	9.618	15.053
Stiffness [N/m]	1.968	1.270	1.063	1.961	1.545	1.214

sample-substrate interface corner, shown in Figure 21, the sample is partly detached from the substrate. The growth of this detached area, however, is very minor when compared to the detached area under the fibre tips which shows that the stress at the fibre tips is considerably higher than the stress at the edges of the sample-substrate interface. Detachment for the reference samples is observed to start at one of the edges of the sample-substrate interface.

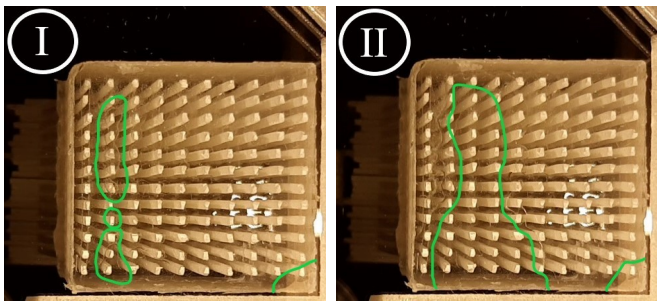

Fig. 21: Stages in sample detachment. The detachment boundaries are highlighted with the green lines. Stage I visualises initial detachment for sample *T_1MPa* for tangential loading and stage II shows the detached area just before full sample detachment.

VI. Discussion

A. Modeling assumptions

Models I-III as described in Section II involve a simplified geometry that does not directly resemble the geometry of the epithelial layer of the tree frog. Model IV, on the other hand, is focused on resembling the properties of an epithelial cell. The assumptions and boundary conditions of this model are discussed in this section.

A.I. Material properties

The adhesional and frictional forces required for the tree frog to prevent detachment from a substrate are purely imposed by gravity while the evaluated loading configurations assume a static situation. The stationary models described in this paper do not involve materials with viscoelastic properties. These properties are time-dependent and can therefore not be modelled with the models described in this paper.

The epithelial layer of the tree frog adhesional pads is well-hydrated and can therefore be expected to have some viscoelastic properties [29], [37]. For a situation in which a static equilibrium is present, these viscoelastic properties do not influence the validity of the modeling results. For more dynamic situations, however, these properties can play a role. The exact extent of this role, however, is not quite clear from the available literature.

The stiffness implemented for the keratinous fibres in the epithelial model is derived from the stiffness measurements found in the literature for the tree frog adhesive pads, as shown in Table I. The stiffness values in this table are not all in the same range and the implemented stiffness is therefore an estimation.

The stiffness implemented for the HGO model is significantly higher than the values used by others who have used the HGO method to model the mechanical properties of other animal tissues [60], [62]. These tissues, however, mainly consist of collagen while the structure of the epithelial cell is mainly composed of keratinous fibres.

The results of the epithelial cell model show that the stress in the corners of the micro-pillars decreases when the stiffness of the cornified cell layer is set to a lower value than the stiffness of the internal structure of the epithelial cell. In literature, the stiffness of the cornified cell layer is argued to be higher than the stiffness of the material directly under this outer cell layer [29], [31] while others describe the opposite [30]. The results described in this paper agree with the observations described by Scholz et al. [30].

A.II. Boundary conditions

The boundary conditions and applied forces implemented for the epithelial cell model include a constraint on the top boundary of the cell that restricts deformation and rotation while an evenly distributed load acts on this boundary. These boundary conditions are an approximation of reality in which all cell boundaries have some degree of compliance. The material between the upper cell boundary and the lower cell boundary (where the forces are measured), will probably smooth out potential unrealistic effects caused by the boundary conditions on the cell top boundary.

The boundary condition imposed upon the right border of the epithelial cell is dependent on the deformation of the geometry and independent of the material stiffness of the epithelial cell. This leads to a larger role for the force on the boundary for lower values of R_{HGO}, which leads to an increased deformation of the geometry. The increased magnitude of the boundary force compensates the load on the cell and with that, reduces the stress in the other regions of the cell. This partly explains the increased stresses in the

epithelial cell for the higher values of R_{HGO}.

The strain stiffening behaviour of the HGO model is one of the causes for the differences between the discrete model and the HGO model. Strain stiffening material behaviour, however, is also encountered in other animal tissues [60], [63], [64] and may therefore be an essential part in approximating the adhesional and frictional performance of the epithelial cell.

B. Modeling results

The modeling results are discussed separately for the discrete models (model I & II) and for the HGO models (model III & IV). The results of model IV are compared to the tree frog behaviour. Finally, the differences between the results from the discrete models and the HGO models are discussed.

B.I. Discrete fibre model: model I & II

Fibre-matrix stiffness ratio

The results obtained from the discrete fibre models indicate that a high fibre-matrix stiffness ratio is beneficial for a geometry loaded in the direction of the fibres. When loaded perpendicular to the fibre direction, however, the lowest stress response is found for an intermediate value (R_s = 10) of the fibre-matrix stiffness ratio. This fibre-matrix stiffness ratio is not in agreement with the stiffness ratio between the fibres and connective tissue described in Section I-C2. The stiffness values of the fibres and connective tissue in the adhesive pads are therefore probably closer to each other than the values derived from the available literature as described in Section I-C2.

A probable explanation of the higher performance for an intermediate fibre-matrix stiffness ratio for a shear loaded discrete fibre model is that the stress in the fibres increases with the increase in the fibre-matrix stiffness ratio. For shear loading, the stress has the largest magnitude in the fibres near the edges of the material which results in a stress peak at the fibre tips near the domain edge while the stress at the edges is relatively low compared to this peak [56].

A low fibre-matrix stiffness ratio (R_s = 1) results in stresses at the edges of a shear loaded domain that are significantly higher than the stress peaks found at the domain edges for the intermediate and high (R_s = 100) values of the fibre-matrix stiffness ratio. A realistic loading configuration involves both shear and normal forces. The stress magnitudes recorded for the shear loading configuration, however, are significantly higher than the stress magnitudes found for the normal loading conditions. A fibre reinforced material loaded with a normal and a shear force which are in the same order of magnitude, is therefore argued to have the best frictional and adhesional performance for an intermediate value of the fibre-matrix stiffness ratio.

Fibre-matrix bonding

The results obtained from the discrete models for both normal and shear loading configurations show that an increase in the fibre-matrix bonding increases the fibre-matrix stress transfer and with that, reduces the magnitude of the stress components. This is in agreement with the results obtained by Xue et al. [56].

An increase in the matrix-fibre bonding, however, reduces the compliance of the geometry. The effect of this compliance reduction is not directly visible in the obtained modeling results. The compliance of the epithelial layer is considered an important property for the tree frog adhesive pads, which allows close pad-substrate proximity [28], [37]. An increase in the matrix-fibre bonding may therefore reduce the adhesive pad effectiveness.

B.II. HGO model: model III

Fibre-matrix stiffness ratio

For normal loading conditions, the response of the HGO model for the various fibre-matrix stiffness ratio's is similar to the response of the discrete fibre model for the various implemented fibre-matrix stiffness ratio's. For shear loading conditions, the maximum magnitude of the stress response increases with respect to the discrete model with an increase of the fibre-matrix stiffness ratio.

Fibre-matrix bonding

To model the effect of the fibre-matrix bonding with the HGO model, a reduced resistance against shear in the planes parallel to the fibres needs to be implemented. Such shear allowance cannot be implemented by varying the parameters C_m, k_1 or k_2, but requires the exclusion of the shear contributions from the location-dependent stiffness matrix which requires an adaption of the HGO model that changes how W_1 and W_4 from Equation 1 are calculated. Such an adaption would fundamentally change the HGO model and therefore falls outside the scope of this paper.

B.III. HGO model: model IV

Fibre-matrix stiffness ratio

The epithelial cell model shows a highly non-uniform stress distribution at the cell-substrate interface for R_{HGO} = 100. This behaviour can be explained by the strain stiffening properties of the HGO model. The magnitude of the stress peak at the left cell edge is significantly lower for R_{HGO} = 10 which confirms the observation described in Section III-A2 that an 'intermediate' fibre-matrix stiffness ratio is an effective way to reduce the magnitude of the stress response at the sample-substrate interface.

Tree frog behaviour vs. modeling results

The proximal pulling on the limbs by the tree frog (the difference between Case 1 and Case 2 described in Section II-D1) is expected to reduce the forces needed to keep the contact between the adhesive pads and the substrate

intact. An increase of the proximal force changes the forces that are in plane with the substrate while the forces acting perpendicular to the substrate are not affected since $F_{n,1}$ and $F_{n,2}$ are not dependent on the tangential force components.

The modeling results, however, indicate that the difference made by the proximal pulling on the adhesion and frictional forces required for attachment performance is only marginal. This is most noticeable for the hind limbs which are significantly longer and stronger compared to the front limbs. The main purpose of the proximal pulling may therefore not be aimed at the reduction of the required frictional and adhesive forces.

Proximal pulling is also reported as a mechanism used by animals with smooth attachment pads to thin the layer of adhesive fluids between adhesive pads and the substrate [28], [30], [40]. A thinner liquid layer at the substrate-pad interface increases the capillary forces acting between the adhesive pad and the substrate [65]–[67]. Proximal pulling can also bring the pad close enough to the substrate to generate dry contact interaction through Van der Waals forces [27], [68].

The absence of a significant difference between the front and hind limbs is in agreement with the absence of any observed differences in morphology between the front and hind limbs of the tree frog in the available literature. Furthermore, there is no reported difference between the mucus properties for the front and hind limbs.

The required forces at the interface between adhesive pads and substrate to maintain adhesional performance as shown in Figure 3 indicate that the limb spreading and positional adjustment of the tree frog can reduce the required adhesion forces while increasing the involved friction forces. These friction forces can 'load' the dermal structure of the adhesive pads and with that, increase the contact area between the pads and the substrate [31], [69]. In this way, the tree frog can simultaneously reduce the required adhesive forces and increase the adhesive and frictional properties of the adhesive pads.

The positional adjustment of the tree frog also reduces the contact angle between the adhesive pads and the substrate. A reduction of the contact angle can further increase the adhesional performance [66]. The effect of contact angle reduction is larger when the positional adjustment causes the contact angle to be reduced to a value that is smaller than the critical contact angle. The critical contact angle is around 30 degrees for flat contact surfaces [19], [70].

B.IV. Discrete fibre model vs. HGO model

The difference in the stress response for the different values of R_{HGO} is relatively small when compared to the difference in the stress response found for a variation of R_s for the discrete fibre model. A probable cause for this is that the strain stiffening properties of the HGO model increase the stiffness in the direction of the fibres for low values of R_{HGO} which indirectly stiffens the material in the fibre direction.

Another difference between the discrete model and the HGO model is that the stress response on the level of individual fibres cannot be implemented with the HGO model. This leads to a difference in the measured stresses between both material models at the edges of the domain for non-uniform loading configurations. The decreased magnitude of the stress at the edge of the domain for the discrete fibre model is probably caused by the lower stresses in the relatively compliant matrix material between the edge of the material domain and the last fibre. The properties of the HGO model are continuous through the domain. The stress peak at the edge of the domain is for this is model probably caused by a combination of non-uniform loading conditions and the strain stiffening properties.

The HGO material model implemented in models III & IV does not incorporate discrete fibres and the results of these models are therefore not considered representative for the stresses at the level of the discrete fibres in the micro-pillars. The stresses at the discrete fibre level are more accurately represented by the fibre pattern implemented in the geometry of model I. Model I is therefore considered representative for the stress components in the micro-pillars. The results of model IV are used to evaluate the influence of the proximal pulling and positional adjustments of the tree frog.

C. Experimental results

The variables that are varied between the different samples are the fibre-matrix stiffness ratio and the fibre density. The experimental results on the effect of these two variables on the adhesional and frictional performance are compared with the modeling results in this section.

C.I. Fibre-matrix stiffness ratio

Adhesion force measurements

Based on the modeling results it was expected that the 1 MPa matrix stiffness samples would outperform the 3 MPa matrix stiffness samples which have a lower fibre-matrix stiffness ratio. The difference in performance was not expected to be very significant since the difference in stiffness ratio between these two groups is relatively low compared to the different fibre-matrix stiffness ratio's implemented in the models.

The experimental results show higher adhesional forces for the samples with relatively low matrix material stiffness compared to the samples with the relatively high matrix material stiffness. This is accordance with the expectations, but the observed difference in adhesional performance is much larger than expected from the modeling results.

A probable cause for this deviation is a difference in the stickiness of the bottom of the samples. The bottom of the 1 MPa matrix stiffness samples was observed to be more sticky than the bottom of the other samples. The difference in bottom stickiness directly influences the adhesion performance since no further adhesive is used to improve the attachment of the samples to the substrate. An increased adhesive performance for a very soft PDMS structure compared to a stiffer PDMS structure is also described by Li et al. [71].

Friction force measurements

The difference between the modelled and experimental results for the influence of the fibre-matrix stiffness ratio as described for the adhesional measurements in the previous section is also applicable for the frictional force measurements.

C.II. Fibre density

Adhesion force measurements

It was expected that samples *T_1MPa* & *T_3MPa* would outperform samples *C_1MPa* & *C_3MPa* due to the better stress distribution for the relatively thin fibre pattern. Based on the modeling results, the difference between the thin and coarse fibre pattern is expected to be less for friction force measurements than for adhesion force measurements. For the adhesive force measurements, the samples with the relatively thin fibres show higher adhesional forces than the reference samples and the samples with the coarse fibre pattern which confirms the expectations.

The measured adhesional force for normal force loading conditions for sample *C_3MPa* is lower than expected from the modeling results which predicted the adhesional performance of this sample to be in between the performance of samples *R_3MPa* & *T_3MPa*. A probable cause for the lower adhesional performance of sample *C_3MPa* is the relatively large bottom surface degradation of this sample as is also shown in Figure 20. Degradation of the attachment performance is also observed for the other samples and plays a larger role for the samples with the 3 MPa matrix material stiffness compared to the samples with the 1 MPa matrix material stiffness. Degradation of PDMS adhesives is also described by others [72], [73].

Friction force measurements

The results on the frictional performance show that both reference samples exhibit higher frictional forces than the fibrous samples. These results are not in agreement with the modeling results, which predicted the reference samples to exhibit lower frictional forces than the fibrous samples.

A possible explanation for this deviation can be found in Table VII. In this table it is shown that the reference samples exhibit a higher resistance to deformation compared to the fibrous samples. This higher resistance to deformation under tangential load reduces the peeling effect which develops when the samples are tangentially loaded. The peeling effect is thus considerably stronger for the fibrous samples than for the reference samples.

A second possible cause for this deviation between the expected and obtained results is that the model (model II) used to predict the experimental results can not be used to produce an estimation of the stress for large deformations. The reason for this is the limited convergence of the model which severely restricted the magnitude of the deformation that could be implemented. Large deformations can considerably affect the stress response of the hyperelastic materials involved which are described to exhibit non-linear strain-dependent properties [59].

D. Recommendations & future work

D.I. Modeling

The material properties implemented in the different models used to obtain the modeling results are derived from studies that describe the mechanical properties of several animal tissues. These properties are considered representative for the mechanical properties of the tree frog epithelial layer. The true mechanical properties of the different materials present in the epithelial, however, are not known and additional research is needed to determine these properties.

The modeling results are influenced by the boundary conditions. Model IV is an approximation of an actual epithelial cell and the boundary conditions of an actual epithelial cell are dependent on the mechanical properties of the other elements in the dermal structure of the terminal digit of the tree frog. The mechanical properties of these other elements are largely unknown and need further research.

One of the assumptions incorporated in the used models is that the sample-substrate attachment is static until sample detachment occurs. Some studies, however, do suggest that static attachment for animals using wet adhesion can also be dynamic [74]. Dynamic attachment is often related to the viscoelastic properties of the mucus layer between the pad and the substrate [27], [74]. The influence of mucus properties and dynamic attachment is not included in this paper.

D.II. Experiments

The observed sample degradation relates to the fabrication method of the samples which includes several steps in which the sample is constructed from different layers of PDMS. The curing of PDMS is time-dependent which leads to differences between the mechanical properties of the different layers in the sample. A production process that involves fewer layers of PDMS would speed up sample production, increase the uniformity of the mechanical properties in the matrix material and would reduce sample degradation. A faster production process would also facilitate an increase in the sample size. A larger sample size would make re-use of samples unnecessary

and with that, reduce the influence of sample degradation.

The larger deformation for the fibrous samples compared to the reference samples is a probable reason for the deviation between modeling and experimental results for tangential loading configurations. To further validate the modeling results, The reference samples should be adapted such that the resistance to deformation of these samples is in the same range as observed for the fibrous samples.

VII. Conclusion

This paper discusses the mechanics of an epithelial cell in a tree frog adhesive pad. The modeling steps taken provide insight into the mechanical behaviour of the fibrous domain and the micro-pillars of the epithelial cell. The analysis of the mechanical behaviour focuses on the stress distribution at the interface of the epithelial layer and a smooth substrate. The goal of this paper is to answer the research question: *'Do the tilted embedded keratin fibres in the epithelial cells and nanopillars prevent the development of stress concentrations on the adhesive pads of the tree frog?'*

Using a simplified modeling approach, it is found that fibre-matrix bonding is essential for the stress distribution in a material. The fibre-matrix bonding should furthermore be equal at the entire interface between fibres and matrix material.

The modeling results indicate that for a fibre reinforced composite with a coarse fibre pattern, the largest stress concentrations at the interface between the sample and the substrate can be found at the locations of the fibre tips. However, for an increasing fibre density (more and thinner fibres), the stress components present at the interface with the substrate smooth out over the length of the interface.

The magnitude of the stress components in a composite material is found to be dependent on the fibre-matrix stiffness ratio. For loading configurations in which the load has a uniform distribution over the domain and acts in the direction of the fibres, an increase in the fibre-matrix stiffness ratio decreases the magnitude of the stress response. For non-uniform loads and loads perpendicular to the fibre direction, a more intermediate fibre-matrix stiffness is found to yield the lowest stresses at the sample-substrate interface.

The effect of the fibre-matrix stiffness ratio is also visible in the epithelial cell model. The stress distribution in the epithelial cell is calculated for the loads associated with the stages in limb spreading of the tree frog. The results of the epithelial cell model show that proximal pulling on the limbs by the tree frog has no significant effect on the stress magnitude at the pad-substrate interface. The positional adjustment of the frog, however, is argued to significantly reduce the magnitude of the maximum stress values at the pad-substrate interface. Furthermore, the behaviour of the frog is argued to reduce the required normal forces while simultaneously increasing the adhesive properties of the adhesive pads.

References

[1] Rui Chen, Leilei Fu, Yilin Qiu, Ruizhou Song, and Yan Jin. A gecko-inspired wall-climbing robot based on vibration suction mechanism. *Proceedings of the Institution of Mechanical Engineers, Part C: Journal of Mechanical Engineering Science*, 233(19-20):7132–7143, 2019.

[2] Matthew J Spenko, G Clark Haynes, JA Saunders, Mark R Cutkosky, Alfred A Rizzi, Robert J Full, and Daniel E Koditschek. Biologically inspired climbing with a hexapedal robot. *Journal of field robotics*, 25(4-5):223–242, 2008.

[3] Alan T Asbeck, Sangbae Kim, Arthur McClung, Aaron Parness, and Mark R Cutkosky. Climbing walls with microspines. In *IEEE ICRA*, pages 4315–4317. Fla., 2006.

[4] Elina Auzina. Exploring the possibility and need of making a spider inspired footpad for robotic legs using a 3d printer for use in a low energy system. In *2015 IEEE 3rd Workshop on Advances in Information, Electronic and Electrical Engineering (AIEEE)*, pages 1–5. IEEE, 2015.

[5] Rui Chen. A gecko-inspired electroadhesive wall-climbing robot. *IEEE Potentials*, 34(2):15–19, 2015.

[6] Matthias Greuter, Gaurav Shah, Gilles Caprari, Fabien Tâche, Roland Siegwart, and Metin Sitti. Toward micro wall-climbing robots using biomimetic fibrillar adhesives. In *Proceedings of the 3rd International Symposium on Autonomous Minirobots for Research and Edutainment (AMiRE 2005)*, pages 39–46. Springer, 2006.

[7] Yilin Su, Xuyan Hou, Shengyuan Jiang, Man Li, Yuming Liu, and Wei Chen. A study of the microstructure modification of a space crawling robot adhesive feet based on discrete element method. *Journal of the Brazilian Society of Mechanical Sciences and Engineering*, 41(11):533, 2019.

[8] Ozgur Unver, Ali Uneri, Alper Aydemir, and Metin Sitti. Geckobot: A gecko inspired climbing robot using elastomer adhesives. In *Proceedings 2006 IEEE International Conference on Robotics and Automation, 2006. ICRA 2006.*, pages 2329–2335. IEEE, 2006.

[9] Elliot W Hawkes, Hao Jiang, and Mark R Cutkosky. Three-dimensional dynamic surface grasping with dry adhesion. *The International Journal of Robotics Research*, 35(8):943–958, 2016.

[10] Dan Sameoto, Yasong Li, and Carlo Menon. Multi-scale compliant foot designs and fabrication for use with a spider-inspired climbing robot. *Journal of Bionic Engineering*, 5(3):189–196, 2008.

[11] Ozgur Unver and Metin Sitti. Flat dry elastomer adhesives as attachment materials for climbing robots. *IEEE transactions on robotics*, 26(1):131–141, 2009.

[12] Sangbae Kim, Matthew Spenko, Salomon Trujillo, Barrett Heyneman, Daniel Santos, and Mark R Cutkosky. Smooth vertical surface climbing with directional adhesion. *IEEE Transactions on robotics*, 24(1):65–74, 2008.

[13] Zhongyuan Wang, Gongxun Sun, and Zhendong Dai. Trajectory optimization for robot crawling on ceiling using dry elastomer adhesive. In *Advances in Reconfigurable Mechanisms and Robots II*, pages 593–601. Springer, 2016.

[14] Zhiwei Yu, Ye Shi, Jiaxing Xie, Simon X Yang, and Zhendong Dai. Design and analysis of a bionic adhesive foot for gecko robot climbing the ceiling. *International Journal of Robotics and Automation*, 33(4), 2018.

[15] Stanislav N Gorb, Mitali Sinha, Andrei Peressadko, Kathryn A Daltorio, and Roger D Quinn. Insects did it first: a micropatterned adhesive tape for robotic applications. *Bioinspiration & biomimetics*, 2(4):S117, 2007.

[16] Moon Kyu Kwak, Changhyun Pang, Hoon-Eui Jeong, Hong-Nam Kim, Hyunsik Yoon, Ho-Sup Jung, and Kahp-Yang Suh. Towards the next level of bioinspired dry adhesives: new designs and applications. *Advanced Functional Materials*, 21(19):3606–3616, 2011.

[17] Kenji Suzuki, Shusuke Nemoto, Takahiro Fukuda, Hideaki Takanobu, and Hirofumi Miura. Insect-inspired wall-climbing robots utilizing surface tension forces. *Journal of Advanced Mechanical Design, Systems, and Manufacturing*, 4(1):383–390, 2010.

[18] Niall Crawford, Thomas Endlein, and W Jon P Barnes. Self-cleaning in tree frog toe pads; a mechanism for recovering from contamination without the need for grooming. *Journal of Experimental Biology*, 215(22):3965–3972, 2012.

[19] MJ Orchard, Mika Kohonen, and Stuart Humphries. The influence of surface energy on the self-cleaning of insect adhesive devices. *Journal of Experimental Biology*, 215(2):279–286, 2012.

[20] MingHe Li, Bin He, HaiYan Qin, YanMin Zhou, HanXiong Lu, and JiGuang Yue. A wet adhesion inspired biomimetic pad with direction dependence and adaptability. *Chinese Science Bulletin*, 56(18):1935–1941, 2011.

[21] Pho Van Nguyen, Ngoc Van Huynh, Tue Trong Phan, et al. Soft grasping with wet adhesion: Preliminary evaluation. In *2018 IEEE International Conference on Soft Robotics (RoboSoft)*, pages 418–423. IEEE, 2018.

[22] Ling Gong, Haiwu Yu, Xuan Wu, and Xiaojie Wang. Wet-adhesion properties of microstructured surfaces inspired by newt footpads. *Smart Materials and Structures*, 27(11):114001, 2018.

[23] William E Duellman and Linda Trueb. *Biology of amphibians*. JHU press, 1994.

[24] GAVIN HANNA, W Jon, and WP JON BARNES. Adhesion and detachment of the toe pads of tree frogs. *Journal of Experimental Biology*, 155(1):103–125, 1991.

[25] W Federle, WJP Barnes, W Baumgartner, P Drechsler, and JM Smith. Wet but not slippery: boundary friction in tree frog adhesive toe pads. *Journal of the Royal Society Interface*, 3(10):689–697, 2006.

[26] Julian KA Langowski, Saranshu Singla, Alex Nyarko, Henk Schipper, Frank T van den Berg, Sukhmanjot Kaur, Henry C Astley, Sander WS Gussekloo, Ali Dhinojwala, and Johan L van Leeuwen. Comparative and functional analysis of the digital mucus glands and secretions of tree frogs. *Frontiers in zoology*, 16(1):1–17, 2019.

[27] Michael Kappl, Farzaneh Kaveh, and W Jon P Barnes. Nanoscale friction and adhesion of tree frog toe pads. *Bioinspiration & biomimetics*, 11(3):035003, 2016.

[28] Julian KA Langowski, Dimitra Dodou, Marleen Kamperman, and Johan L van Leeuwen. Tree frog attachment: mechanisms, challenges, and perspectives. *Frontiers in zoology*, 15(1):1–21, 2018.

[29] W Jon P Barnes, Pablo J Perez Goodwyn, Mohsen Nokhbatolfoghahai, and Stanislav N Gorb. Elastic modulus of tree frog adhesive toe pads. *Journal of Comparative Physiology A*, 197(10):969, 2011.

[30] Ingo Scholz, W Jon P Barnes, Joanna M Smith, and Werner Baumgartner. Ultrastructure and physical properties of an adhesive surface, the toe pad epithelium of the tree frog, litoria caerulea white. *Journal of Experimental Biology*, 212(2):155–162, 2009.

[31] Masato Nakano and Tomoyuki Saino. Light and electron microscopic analyses of the high deformability of adhesive toe pads in white's tree frog, litoria caerulea. *Journal of morphology*, 277(11):1509–1516, 2016.

[32] Julian KA Langowski, Henk Schipper, Anne Blij, Frank T van den Berg, Sander WS Gussekloo, and Johan L van Leeuwen. Force-transmitting structures in the digital pads of the tree frog hyla cinerea: a functional interpretation. *Journal of anatomy*, 233(4):478–495, 2018.

[33] Valerie V Ernst. The digital pads of the tree frog, hyla cinerea. i. the epidermis. *Tissue and Cell*, 5(1):83–96, 1973.

[34] Dirk M Drotlef, Esther Appel, Henrik Peisker, Kirstin Dening, Aránzazu del Campo, Stanislav N Gorb, and W Jon P Barnes. Morphological studies of the toe pads of the rock frog, staurois parvus (family: Ranidae) and their relevance to the development of new biomimetically inspired reversible adhesives. *Interface focus*, 5(1):20140036, 2015.

[35] Thomas Endlein, Aihong Ji, Diana Samuel, Ning Yao, Zhongyuan Wang, W Jon P Barnes, Walter Federle, Michael Kappl, and Zhendong Dai. Sticking like sticky tape: tree frogs use friction forces to enhance attachment on overhanging surfaces. *Journal of The Royal Society Interface*, 10(80):20120838, 2013.

[36] Thomas Endlein, Aihong Ji, Shanshan Yuan, Iain Hill, Huan Wang, W Jon P Barnes, Zhendong Dai, and Metin Sitti. The use of clamping grips and friction pads by tree frogs for climbing curved surfaces. *Proceedings of the Royal Society B: Biological Sciences*, 284(1849):20162867, 2017.

[37] BNJ Persson. Wet adhesion with application to tree frog adhesive toe pads and tires. *Journal of Physics: Condensed Matter*, 19(37):376110, 2007.

[38] WJP Barnes, P Perez-Goodwyn, and SN Gorb. Mechanical properties of the toe pads of the tree frog, litoria caerulea. *Comparative Biochemistry and Physiology. Part A: Molecular and Integrative Physiology*, 141(3 Supp):S145–S145, 2005.

[39] W Jon P Barnes, Martina Baum, Henrik Peisker, and Stanislav N Gorb. Comparative cryo-sem and afm studies of hylid and rhacophorid tree frog toe pads. *Journal of morphology*, 274(12):1384–1396, 2013.

[40] Ling Gong, Xiaojie Wang, Haiwu Yu, and Xuan Wu. Observation of micro-topography of newt toe pads and investigating on wet adhesive properties of microstructured surface of pdms. In *Bioinspiration, Biomimetics, and Bioreplication VIII*, volume 10593, page 105930M. International Society for Optics and Photonics, 2018.

[41] David Labonte and Walter Federle. Biomechanics of shear-sensitive adhesion in climbing animals: peeling, pre-tension and sliding-induced changes in interface strength. *Journal of The Royal Society Interface*, 13(122):20160373, 2016.

[42] Zhilong Peng, Cong Wang, and Shaohua Chen. The microstructure morphology on ant footpads and its effect on ant adhesion. *Acta Mechanica*, 227(7):2025–2037, 2016.

[43] David AD Parry and Alan S Craig. Growth and development of collagen fibrils in connective tissue. In *Ultrastructure of the connective tissue matrix*, pages 34–64. Springer, 1984.

[44] Colin A Grant, David J Brockwell, Sheena E Radford, and Neil H Thomson. Tuning the elastic modulus of hydrated collagen fibrils. *Biophysical journal*, 97(11):2985–2992, 2009.

[45] Marco PE Wenger, Laurent Bozec, Michael A Horton, and Patrick Mesquida. Mechanical properties of collagen fibrils. *Biophysical journal*, 93(4):1255–1263, 2007.

[46] R Harley, D James, A Miller, and JW White. Phonons and the elastic moduli of collagen and muscle. *Nature*, 267(5608):285–287, 1977.

[47] Pavel Dutov, Olga Antipova, Sameer Varma, Joseph PRO Orgel, and Jay D Schieber. Measurement of elastic modulus of collagen type i single fiber. *PloS one*, 11(1):e0145711, 2016.

[48] BB Aaron and JM Gosline. Elastin as a random-network elastomer: A mechanical and optical analysis of single elastin fibers. *Biopolymers: Original Research on Biomolecules*, 20(6):1247–1260, 1981.

[49] John Gosline, Margo Lillie, Emily Carrington, Paul Guerette, Christine Ortlepp, and Ken Savage. Elastic proteins: biological roles and mechanical properties. *Philosophical Transactions of the Royal Society of London. Series B: Biological Sciences*, 357(1418):121–132, 2002.

[50] RH C BONSER. The young's modulus of ostrich claw keratin. *Journal of Materials Science Letters*, 19(12):1039–1040, 2000.

[51] JE Bertram and JM Gosline. Functional design of horse hoof keratin: the modulation of mechanical properties through hydration effects. *Journal of Experimental Biology*, 130(1):121–136, 1987.

[52] WS Simpson. 51—a comparison of methods of measurement of young's modulus for keratin fibres. *Journal of the Textile Institute Transactions*, 56(12):T675–T683, 1965.

[53] Valentin Lulevich, Hsin-ya Yang, R Rivkah Isseroff, and Gang-yu Liu. Single cell mechanics of keratinocyte cells. *Ultramicroscopy*, 110(12):1435–1442, 2010.

[54] GJ Cameron, Tim J Wess, and RHC Bonser. Young's modulus varies with differential orientation of keratin in feathers. *Journal of structural biology*, 143(2):118–123, 2003.

[55] Anne M Peattie, Carmel Majidi, Andrew Corder, and Robert J Full. Ancestrally high elastic modulus of gecko setal β-keratin. *Journal of The Royal Society Interface*, 4(17):1071–1076, 2007.

[56] Longjian Xue, Belén Sanz, Aoyi Luo, Kevin T Turner, Xin Wang, Di Tan, Rui Zhang, Hang Du, Martin Steinhart, Carmen Mijangos, et al. Hybrid surface patterns mimicking the design of the adhesive toe pad of tree frog. *ACS nano*, 11(10):9711–9719, 2017.

[57] LePing Li, JTM Cheung, and W Herzog. Three-dimensional fibril-reinforced finite element model of articular cartilage. *Medical & biological engineering & computing*, 47(6):607, 2009.

[58] Raymond W Ogden. *Non-linear elastic deformations*. Courier Corporation, 1997.

[59] Melvin Mooney. A theory of large elastic deformation. *Journal of applied physics*, 11(9):582–592, 1940.

[60] Gerhard A Holzapfel, Thomas C Gasser, and Ray W Ogden. A new constitutive framework for arterial wall mechanics and a comparative study of material models. *Journal of elasticity and the physical science of solids*, 61(1-3):1–48, 2000.

[61] Carl Runge. Über empirische funktionen und die interpolation zwischen äquidistanten ordinaten. *Zeitschrift für Mathematik und Physik*, 46(224-243):20, 1901.

[62] MJ Collins, M Bersi, E Wilson, and JD Humphrey. Mechanical properties of suprarenal and infrarenal abdominal aorta: implications

for mouse models of aneurysms. *Medical engineering & physics*, 33(10):1262–1269, 2011.

[63] Kendra A Erk, Kevin J Henderson, and Kenneth R Shull. Strain stiffening in synthetic and biopolymer networks. *Biomacromolecules*, 11(5):1358–1363, 2010.

[64] Mo Li, Zibo Gao, Taidong Dai, Donghui Chen, Jin Tong, Li Guo, and Chaofei Wang. Comparative research on morphology and mechanical property of integument of rana dybowskii, xenopus laevis and ambystoma mexicanum. *Journal of the Mechanical Behavior of Biomedical Materials*, page 104382, 2021.

[65] Pierre Simon Laplace. *Traité de mécanique céleste*, volume 1. de l'Imprimerie de Crapelet, 1799.

[66] Jin Qian and Huajian Gao. Scaling effects of wet adhesion in biological attachment systems. *Acta biomaterialia*, 2(1):51–58, 2006.

[67] Xiong Yi, Imad Ahmed, Michael Kosinsky, Xiangjun Zhang, Yonghe Liu, and J Schaefer. Dynamic contact model of bio-adhesive pads of animals: Simulation experiments. In *Advanced Tribology*, pages 867–868. Springer, 2009.

[68] Walter Federle, Werner Baumgartner, and Bert Hölldobler. Biomechanics of ant adhesive pads: frictional forces are rate-and temperature-dependent. *Journal of Experimental Biology*, 207(1):67–74, 2004.

[69] Pablo Perez Goodwyn, Andrei Peressadko, Heinz Schwarz, Victoria Kastner, and Stanislav Gorb. Material structure, stiffness, and adhesion: why attachment pads of the grasshopper (tettigonia viridissima) adhere more strongly than those of the locust (locusta migratoria)(insecta: Orthoptera). *Journal of comparative physiology A*, 192(11):1233–1243, 2006.

[70] Yewang Su, Baohua Ji, Yonggang Huang, and Kehchih Hwang. Concave biological surfaces for strong wet adhesion. *Acta Mechanica Solida Sinica*, 22(6):593–604, 2009.

[71] Meng Li, Jun Xie, Qingwen Dai, Wei Huang, and Xiaolei Wang. Effect of wetting case and softness on adhesion of bioinspired micropatterned surfaces. *Journal of the mechanical behavior of biomedical materials*, 78:266–272, 2018.

[72] Dirk-Michael Drotlef, Lukas Stepien, Michael Kappl, W Jon P Barnes, Hans-Jürgen Butt, and Aránzazu del Campo. Insights into the adhesive mechanisms of tree frogs using artificial mimics. *Advanced Functional Materials*, 23(9):1137–1146, 2013.

[73] Jagoba Iturri, Longjian Xue, Michael Kappl, Luis García-Fernández, W Jon P Barnes, Hans-Jürgen Butt, and Aránzazu del Campo. Torrent frog-inspired adhesives: attachment to flooded surfaces. *Advanced Functional Materials*, 25(10):1499–1505, 2015.

[74] Leonid Frantsevich, Aihong Ji, Zhendong Dai, Jintong Wang, Ludmila Frantsevich, and Stanislav N Gorb. Adhesive properties of the arolium of a lantern-fly, lycorma delicatula (auchenorrhyncha, fulgoridae). *Journal of insect physiology*, 54(5):818–827, 2008.

Report

Adhesive mechanisms and the role of positional adjustment on tree frog toe pads

April 15, 2021

R. Copier | 4354095

TU Delft

Preface

Back in my childhood, I used to catch tadpoles in the ditch near our house and while the other kids resumed with other activities, my mother sometimes found me gazing in the bucket were the tadpoles were imprisoned. She often had to call me several times to tear me away from the fascinating sight of the little creatures in the bucket. The tadpoles quickly grew and so did I. During my high school period, I developed a preference for physics and mathematics which led to my choice to study mechanical engineering at the TU Delft. My fascination for nature however, remained the same. This led to my choice for the biomechanical design track which enables me to combine the best of two different worlds. These two worlds are also present in the contents of this thesis. It combines my awe and fascination for the wonder of nature and my desire to analyse the mechanics of things that are not fully understood yet. The focus of this thesis on fully developed tadpoles sometimes brought me back to my childhood and reminded my of the benefits of a childlike open-minded attitude.

For the obtained results however, I also have to thank everyone who helped my along the way. This thesis would definitely not be the same without the tremendous support I received from Dimitra Dodou and Aimée Sakes. I want to thank Aimée for the help and inspiration I received to guide me through my literature study and to determine the focus of my thesis. I want to thank Dimitra for the constructive feedback on the modelling work and the experimental setup and results. Furthermore I want to thank Julian Langowski from Wageningen University for his willingness to help me with his expertise on the tree frog morphology. At last I also want to thank Mark Goossens and all the other employees at the workshop for helping me with the assembly of my samples.

I also want to thank all my friends and family with were all tremendously supportive throughout my gradation process. In particular I want to thank my girlfriend for her willingness to provide me with perspective when I needed it. The time has come to proceed with a new life chapter and I sincerely hope that I can do that with you all.

Rick Copier
Delft, April 15, 2021

Abstract

Background: the performance of wall climbing robots depends on the reversible adhesional properties of the mechanism used for locomotion. In nature, reversible adhesion is applied by animals to walk on vertical or inverted surfaces. The tree frog is such an animal and uses adhesive pads that also allow for reversible adhesion in very wet environments. The keratinized epithelium on the adhesive pads of tree frogs incorporates keratinous fibres embedded in a relatively compliant matrix material. The epithelium consists out of epithelial cells. The cell-substrate interface of these cells consists from an array of micro-pillars which are filled with the keratinous fibres.

Goal: the aim of this work is to evaluate the mechanical behaviour of the keratinised epithelium. The main assessment criterion for the mechanical behaviour is the stress distribution at the interface between the epithelium domain and the substrate since the magnitude of this stress determines the adhesive performance of the epithelium.

Methods: the epithelium mechanical behaviour is analysed by evaluating the influence of the fibre density, the fibre-matrix bonding and the fibre-matrix stiffness ratio. These factors are implemented in different modelling steps. The mechanical behaviour in the micro-pillars is modelled with a simplified model in which discrete fibres are present. The mechanics of the fibrous domain in the epithelial cell is modelled with an anisotropic hyperelastic material model (HGO model). The mechanical behaviour of the epithelium is furthermore coupled with the tree frog behaviour, which consists of proximal pulling on the limbs and adjustments in the body posture and the position of the limbs. To validate the modelling results obtained on the influence of the fibre-matrix stiffness ratio and the fibre density, a set of samples is fabricated that mimic the epithelial composite structure. These samples consist of a polydimethylsiloxane (PDMS) base matrix in which acrylonitril-butadieen-styreen (ABS) fibres are embedded.

Results: the modelling results show that a higher fibre density and good fibre-matrix boding increases adhesive and frictional performance. An increase in the fibre-matrix stiffness ratio is found to be beneficial for adhesional performance while for frictional performance an optimum value exists for this ratio. Furthermore, the modelling results show that proximal pulling on the limbs by the tree frog has no significant effect on the adhesional and frictional performance. The positional adjustment however, is found to significantly reduce the magnitude of the stress values at the pad-substrate interface. For adhesion, the model results are in agreement with the experimental results. For the frictional response, the agreement between the modeled results and experimental results is less strong.

Conclusion: the results of this research provide insight in the mechanical behaviour of the tree frog epithelium and show that the positional adjustments made by the tree frog have the potential to decrease the required adhesion force while simultaneously increasing the adhesive properties of the adhesive pads.

Keywords **- biomimetric, bio-inspired adhesives, tree frog, discrete model, HGO model, fibre-matrix composite, fibre-matrix stiffness ratio, fibre density**

Contents

1 Introduction

Wall climbing robots have potential applications for tasks at locations that are hard to reach or inaccessible for humans. These robots depend on surface adhesion for locomotion on vertical and inverted surfaces. Nature offers a wide variety of animals using adhesion for locomotion. The feet of these animals have reversible adhesive properties which allows them to climb vertical and inverted surfaces of various roughness. A well-known example of an animal which makes use of adhesion for locomotion is the gecko. This animal makes use of dry adhesion for which Van der Waals forces play a dominant role. Other animals like tree frogs and newts makes use of wet adhesion through secretion fluids which enable them to use capillary adhesional forces. This paper explores the state of the art of wet and dry adhesives used for adhesion for robotic applications and provides further insight in the mechanics of the adhesive performance of the adhesive pads of the tree frog.

1.1. Dry adhesion

Robots that utilise bio-inspired adhesives employ mechanical legs, rotating levers or continuous belts on which the adhesive materials are placed. Some of the existing climbing robots are vacuum powered [11]. Other applications, like the robots RiSE [64] Spinybot [2], DROP and LEMUR [3] utilise claws and spines to establish mechanical interlocking to overcome gravitational forces when climbing a vertical or inverted surface. Others use magnetic forces[64], or electrostatic forces to establish adhesion [10].

Most robotic applications make use of Van der Waals forces which require very close contact between the adhesive pad and substrate. Close contact is established with very compliable materials such as silicone [32, 66, 69, 35, 61] or polyurethane rubber [68, 39, 61, 71], often with a structured or 'hairy' surface to make use of the principle of contact splitting [75, 39, 29].

Hairy adhesive pads are promising for dry adhesion since they are less sensitive to surface roughness and flaws like cracks and contamination [29]. These adhesives are also directional dependent which means that they adhere well under shear but easily detach when shear forces are removed [35, 39].

Robotic applications using magnetic, electrostatic or vacuum adhesive pads have a very high power consumption which limits their useability [3, 69]. Furthermore, suction mechanisms are very sensitive to surface roughness [69] and electrostatic adhesives attract contamination which reduces adhesional effectiveness. Other adhesives made from soft materials like silicone quickly degrade due to contamination or wear [32, 69, 41]. Climbing performance on vertical and inverted surfaces varies between robotic applications. All of these applications, however, suffer from performance reduction through adhesive pad contamination.

1.2. Wet adhesion

The mechanism of wet adhesion is applied less in robotic applications. wet adhesion is arguably better for light robotic applications because it requires a low load to establish [67]. Furthermore, capillary forces have a larger working range than Van der Waals forces and thus allow for larger tolerances in the distance between adhesive pad and surfaces. It is argued that animals using wet adhesion are also able to make use of Van der Waals forces due to the compliable nature of the adhesive pads of these animals.

The state of the art in the field of biomimetic pads for wet adhesion includes pads that are inspired on the adhesive pads of insects, [49, 67] like the stick insect, tree frogs[70] or newts [27]. These biomimetic pads are made from compliant materials to increase the effective surface area of the pads. The adhesive pads inspired by the tree frog[70] and the newt[27] incorporate channels in the pad surface to drain excess liquids. The insect-inspired pad described by Li et al.[49] incorporates internal fibres to mimic the internal structure of the adhesive pads of the stick insect.

1.3. Tree frog adhesion

1.3.1. Morphology

Tree frogs secrete a watery mucus to increase their adhesional performance [16, 13]. The exact functionality of the mucus secreted by tree frogs is not yet clear. Studies show that both viscous forces and surface tension are likely to contribute to the adhesional performance of the tree frog [33, 23, 43].

Adhesional performance is furthermore dependent on the compliance of the adhesional pads[38, 45]. Adhesional pad compliance is relevant for all animals that make use of reversible adhesion and is dependent on the morphological properties of the pads used by animals to adhere to a surface. The morphological properties of the digital digits of the different species of tree frogs described in literature are very similar: it is usually not possible to identify the family from the appearance of the toe pads [5]. The morphological properties described below are from observations on the *Litoria Caerulea White* by Scholz, Barnes and Nakano et al. [62, 5, 53], on the *Osteopilus Septentrionalis* by Hanna et al. [33], on the *Hyla Cinerea* by Ernst and Langowski et al [21, 44] and the *Staurois Parvus* by Drotlef et al. [14].

The specialised adhesive pad epithelium of the *Hyla Cinerea* is 10- 15 [µm] thick and delineated from the normal skin by distinct grooves [21, 44, 38]. The epidermis consists of four to six layers of columnar epithelial cells. The outermost layer is non-living and consists from polygonal epithelial cells [33, 18, 19]. Most of these are hexagonal, but pentagonal, heptagonal and octagonal formed epithelial cells are also observed [14]. The structure of the second cell layer is very similar to the structure of the outer cell layer[44, 21] and becomes the outer layer when the first layer has worn of. The epithelial cells contain keratin fibrils which are oriented at an angle to the surface. For both tree frogs and rock frogs, the fibrillar structures in the epithelial cells are distally pointed.

The amount of angling varies between species: for some species, the fibrillar structure is almost normal tot the surface while for other species like the *Hyla Cinerea* [44, 21], the fibrillar structures are more angled as is shown in Figure 1.1. The nanopillars on top of the epithelial cells are formed from the ends of these keratin filaments and (partly) fill these structures. The presence of the keratin filaments increases the stiffness and the wear resistance of the epithelial cells[6]. The angling of the keratin filaments is described to give the adhesive pad directional dependent properties[44].

The epithelial cells have a diameter of 13 [µm] [38]. A network of channels exists between the epithelial cells which follows the hexagonal pattern of the epithelial cells for the tree frogs[21, 53]. The adhesive pads of the rock frogs, however, has more stratified channels which form a shorter route to the channel running around the toe pads[14]. The channels between the epithelial cells for both tree frogs and rock frogs have a width of about 1-2 [µm] and are about 10 [µm] in depth[21, 53]. The channel surrounding the toe pad not only functions in drainage of excess water from the pad but is also argued to drain excess ambient liquids around the pad to prevent excessive wetting of the pad [58].

The surfaces of the epithelial cells are covered with closely packed columnar nanopillars. These pillars measure 200-350 [nm] in diameter for the frog species *Osteopilus Septentrionalis* and *Staurois Parvus* [33]. The height of the nanopillars for these frogs is 300-500 [nm] which gives the pillars an aspect ratio between 1 and 2. The nanopillars of the *Litoria Caerulea* are smaller with a diameter and height of approximately 22 [nm][5, 53].

The nanopillars shown in Figure 1.2 do contribute to the frictional and adhesive properties of the adhesive

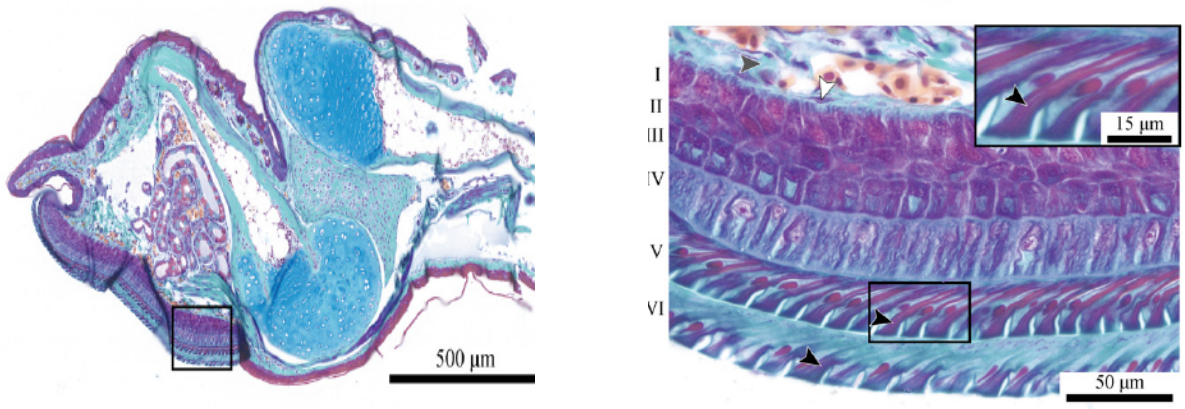

(a) (b)

Figure 1.1: Pictures from the paper by Langowski et al. [44] which show the epidermal structure to the level of the epithelial cells. (1.1a) A mid-sagittal section of a digital pad of the Hyla Cinerea. (1.1b) A magnified view of the ventral epidermis. The cellular layers are numbered with the numbers I-VI. The fibrillar structure has a reddish colour and is also shown in the magnified view in the top right of the image. The black arrows point to the fibrillar structure in the epithelial cells, the white arrows to the reticular cells and the grey arrows point to the reticular connective tissue.

pads [13, 18, 26, 62]. The most probable mechanism for this performance enhancement is that the nanopillars allow for close conformation to surface irregularities. Just as the epithelial cells, but at a much smaller length scale. Close contact activates Van der Waals forces and increases capillary forces through thinning of the fluid layer between the adhesive pad and the substrate[13, 18].

Close surface conformation is furthermore probable caused by the presence of the grooves surrounding each nanopillar and by the high pillar material compliance and aspect ratio. The nanopillars mainly affect the frictional forces which do approach dry frictional forces due to the close contact made between the adhesive pad and surface[18, 38, 42]. The role of the micro-pillars for the capillary forces is argued to be less since such forces are generated by the air-water interface around the edge of the whole adhesive pad [21].

The nanopillars each have a slight depression or 'dimple' on top of each pillar[62, 4]. The dimple has a depth of approximately 6-8 [nm] and the edges of these dimples are interrupted with one or two channels connecting the dimple with the surrounding space between the nanopillars. Between the nanopillars are channels. These channels are part of the channel network on the adhesive pads which drains excess water from the pads and acts as a reserve to make capillary adhesion possible on dry surfaces.

1.3.2. Material properties of the adhesive pad

The epidermal structure of the tree frog is composed of different materials. The exact composition of this structure is known to be dependent on the age of the animal [5] and it furthermore likely to be dependent on species and living environment as it is for other animals [57]. The adhesional performance of the animal is dependent on the mechanical properties of the adhesive pads. Actual measurements of these properties are described in studies by Barnes et al. and in work from Scholz et al. [6, 62, 5, 4, 38]. The results from the stiffness measurements are shown in Table 1.1. The content of this table matches the content published by Langowski et al. [45]. The Young's modulus of the adhesive pads is found to be inversely proportional to the indentation depth which makes the toe epidermis self-adaptive to an applied load. The pads show pure elastic deformation when indented more than 200 [μm] [5]. Furthermore, the toe pad epithelium is found to be stiffer than the dermal material directly under the epithelium.

In Table 1.1 is shown that the stiffness values found for the experiments described by Scholz are much higher than the values found in the studies of Barnes et al. In the paper published by Barnes in 2011, the author ascribes the higher measured stiffness in the study by Scholz et al. to the the difference in indentation depth between the experiment carried out by Scholz et al. and the experiment carried out by Barnes et al. in

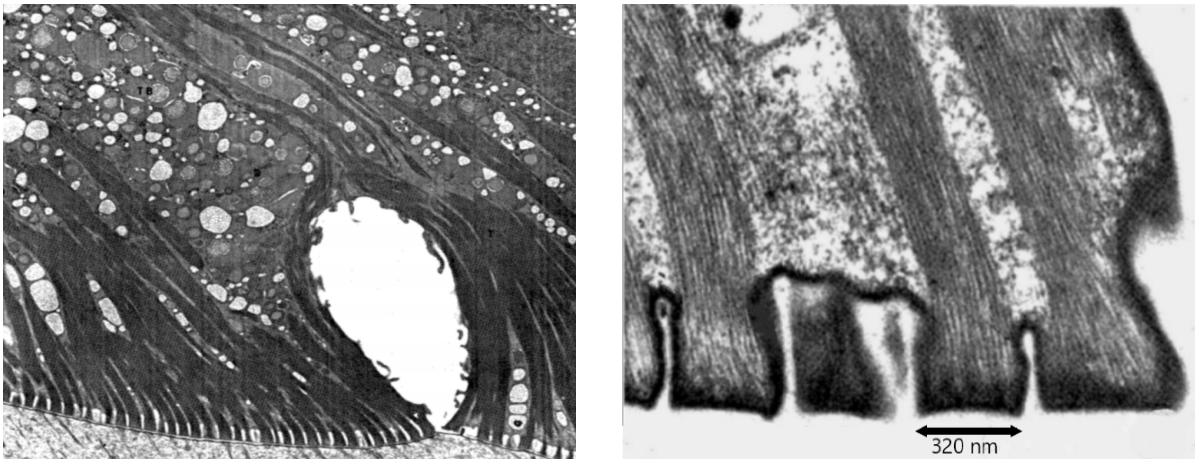

(a) **(b)**

Figure 1.2: Pictures from the paper by Ernst et al. which show the structures of the adhesive pads of the Hyla cinerea [21]. (1.2a) Epithelial cells on which multiple nanopillars are shown. The dark lines are the keratin fibres which originate in the epithelial cells and run up to the surfaces of the nanopillars. (1.2b) Close-up of the nanopillars with a more detailed view on the keratin fibres. The width of one nanopillar as depicted above is an estimation based on the data provided by Ernst et al.

Table 1.1: Setup and results from indentation experiments described in literature

Species	Setup	Diameter indentor [μm]	Indentation depth [μm]	Frequency [Hz]	Indentation velocity [μm]	Stiffness mean value [kPa]	Work of adhesion [J/m^2]	Source
Litoria Caerulea	Whole frog with restricted limbs, temporally anesthetized		1.6	1-2	3.2-6.4	5.7e3		Scholz 2009
Litoria Caerulea			50 - 350			12		Barnes 2005
Litoria Caerulea	Whole frog with restricted limbs, temporally anesthetized	1500	350	1/35, 5 s relaxation time	23	4.45	0.08	Barnes 2011
Litoria Caerulea	Toes removed from frogs	0.04	0.2	0.5		33.5		Barnes 2013
Rhacophorus Prominanus	Toes removed from frogs	0.04	0.2	0.5		28.7		Barnes 2013

2011. The experiments by Barnes et al. from 2013, however, use a similar technique and indentation depth as used by Scholz et al. in 2009 and still show much lower values for the stiffness than reported by Scholz et al. Possible other explanations for this difference in measured stiffness are:

- The indentation frequency used in the experiments by Scholz et al. is higher than described by Barnes et al. which can allow viscoelastic effects to play a role. The stiffness of most viscoelastic materials increases with an increase in loading frequency.
- The experiment described by Barnes et al. from 2013 involves tree frog toes that are separated from the animal while the experiment by Scholz et al. involves living tree frogs. Measurements on living tissue

are more sensitivity to animal induced distortions such as the animal's heartbeat.

- For the study by Barnes et al. from 2013, the cut-off limbs were placed in a Ringer's solution which can soften the epithelial tissue and especially the outer layer of the cellular layers. A relatively small difference in the tissue stiffness can play a considerable role since the indentation depth is relatively small in the experiment described in this study.
- Barnes et al. describe that the stiffness of epithelial material increases with the age of the tree frog [5]. A difference in age between the frogs used by Barnes and Scholz could play a role in the difference in measured stiffness between these two studies.
- The mathematical models to calculate the stiffness from the indentation data differ between the studies under consideration. Barnes describes a modified version of the Hertz contact model while Scholz has used a force-indentation model from Oliver and Parr. Both models can be used to calculate stiffness values but may produce different results for similar input data.

As a consequence of the relatively large difference between the reported values of the stiffness of the adhesive pads, the stiffness of these pads needs to based on a choice of one of the values reported in literature while neglecting the others. The stiffness values reported by Barnes et al. are considered the most reliable because:

- The stiffness values reported in the three papers by Barnes et al. are all in the same range while each paper reports another theoretical model to calculate the stiffness values from the raw measured data.
- The paper published in 2011 describes that the samples were tested at a frequency to eliminate viscoelastic effects.
- The paper published in 2013 gives the stiffness of the epithelial layer of two different frog species. The measured values are of the same order of magnitude.

The stiffness measurements from the studies of Barnes et al. give an order of magnitude for the stiffness of the epithelial layer of the tree frog. These stiffness measurements, however, need to be approached carefully:

- The results of the stiffness measurements obtained with the smallest indentation depths (0.2 [μm]) are expected to be very sensitive to variations in the surface of the epithelial layer. The surface of the epithelial layer consists of nanopillars as is shown in Figure 1.2. An indentation measure between two nanopillars is expected to produce a different result than a similar measurement on the surface of a pillar.
- The adhesive pads are expected to have a direction-dependent stiffness due to the fibrillar internal structure. The stiffness measured with an indentation measurement does not apply a tensile load on the internal fibres. The stiffness measured in an experiment in which the internal fibres are loaded in tension is therefore expected to be considerably higher. The stiffness values reported by Barnes et al. are expected to be in the range of the stiffness of the material surrounding the fibres. The stiffness of this material is expected to be of considerably lower stiffness than the fibre material.
- The epithelial cells are partially filled with cytoplasm. A large volume of cytoplasm will increase the compliance of the epithelial cell when compared to a cell without cytoplasm. Well-hydrated tissue is more sensitive to viscoelastic effects. The indentation frequency therefore, has to be low enough to prevent such effects.

Figure 1.3 shows the cell components of an epithelial cell. The nucleus is not expected to contribute to the mechanical properties of the cell.

The stiffness measurements on the adhesive pads of the tree frog can be compared to other stiffness measurements performed on animal tissue. The mechanical properties of animal tissue depend on the type of protein and the level of hydration. One of the most frequent proteins is collagen. The fibres in the tree frog epithelial layer are composed of keratin which has a higher stiffness than collagen.

Some stiffness values found for animal keratin in literature are given in Table 1.2. Keratin found in mammals can be classified as alpha or helical keratin while the keratin found in birds and reptiles can be classified as beta or pleated-sheet keratin [8]. The elastic properties of keratin in birds and reptiles are therefore considered more representative of the keratin properties of the tree frog. In the table below is also shown that the

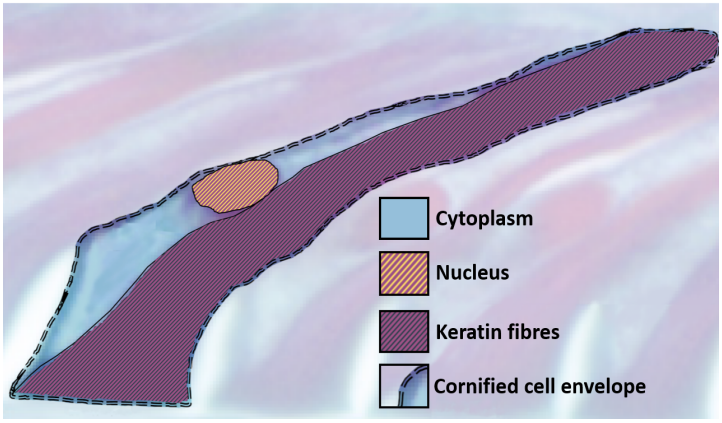

Figure 1.3: Epithelial cell with cell components. Derived from the work of Langowski et al.[44].

Table 1.2: Stiffness values for animal and human keratin. The lower three rows give the stiffness values of pleated sheet keratin and are thus most relevant.

Origin	Elastic modulus [GPa]	Source
Sheep wool	7-47	[63]
Human keratinocyte cytoskeleton	1.2e-4 3.4e-4	[51]
Birds claw	1.84	[8]
Birds feathers	2-5	[9]
Gecko setae	1.5	[56]
Horse-hoof	0.41 - 14.6	[7]

elastic moduli of the bird's claw, the bird's feathers and the gecko setae are very similar.

The keratin fibres in the epithelial layer are embedded in connective tissue. Connective tissue typically has a lower stiffness than keratin but the exact composition of the connective tissue in the epithelium is not described in the literature. Common connective tissues in tissue are collagen and elastin. The material properties of collagen are listed in Table 1.3. The collagen material stiffness values are slightly lower but in the same range as the stiffness values found for keratin tissues. This can be caused by the highly directional properties of the tissues used to determine these stiffness values. Such directional properties are not observed in the material between the keratin fibres and above and below these fibres in the epithelial cell. The elastic properties of elastin indicate a much lower stiffness than the stiffness of collagen.

Table 1.3: Stiffness values for animal connective tissue.

Origin	Elastic modulus [GPa]	Source
Collagen, rat tail tendon	3.75	[72]
Collagen, bovine Achilles tendon	9.0	[34]
Collagen, rat tail tendon	0.1 -0.36	[17]
Collagen, bovine Achilles tendon	0.002 - 0.2	[31]
Bovine elastin	0.00041	[1]
Bovine elastin	0.0011	[30]

The stiffness values found in the literature for collagen are relatively close to the stiffness values found for keratin. The stiffness of these materials, however, can be severely influenced by the degree of hydration. Grant et al. describe a range of 2-200 [MPa] for bovine collagen in varying solution conditions [31] and Bertram et al. [7] describes that the stiffness of horse-hoof keratin can be varied over a range of 0.41-14.6 [GPa] depending on the hydration of the material.

The relatively high stiffness measurements on hairs, claws, feathers and setae as shown in Table 1.2 are all

obtained from dead and relatively dry materials. The stiffness of these materials is much higher than the stiffness of living keratinous material like keratinocytes as also shown in Table 1.2. These keratinocytes are much better hydrated than the dead keratinous materials. Furthermore, it should be noted that keratinocytes are living cells that also contain other cell elements which are most likely not as stiff as the keratinous elements in these cells. The stiffness of pure keratinous fibres is therefore expected to be in the range of 1-10 [GPa].

The exact composition of the connective tissue between the fibres is not reported in the literature. Based on the stiffness values shown in Table 1.3, the stiffness of the connective tissue between the keratin fibres is probably somewhere in between the stiffness values reported for collagen and elastin. Furthermore, the connective tissue in the epithelial cells is well hydrated. The effective stiffness of the connective tissue is therefore estimated at a range of 1-10 [MPa].

The most superficial layer of the epithelium of the adhesive pads is argued to have a relatively high stiffness [53]. This cornified cell envelope is about 10 [nm] thick and is composed of insoluble proteins. The stiffness of this layer is probably in the range of the other keratinous cell elements.

1.3.3. Behavioural analysis

A study performed by Endlein et al. [18] shows that tree frogs actively change their position when higher adhesional forces are required. The tree frogs change their position to a sprawled position by extending their legs laterally which reduces the contact angle between pads and substrate and increases the lateral forces at the contact interface. This spreading is shown in Figure 1.4.

(a) **(b)** **(c)**

Figure 1.4: Stages in the limb spreading of the tree frog on inclined surfaces. (1.4a) The initial position of the resting frog. (1.4b) The first spread of the frog. (1.4c) The second spread of the frog. Derived from Endlein et al. [18].

There are two stages in the limb spreading: the frog first spreads its limbs when adhesional performance in the resting position is insufficient (Figure 1.4b). The frog spreads its limbs even further when the adhesional performance in the first spread is insufficient (Figure 1.4c). The impact of the spreading behaviour is further described in Section 3.4.

The magnitude of the forces involved in the proximal pulling is shown in Figure 1.5 which shows that the magnitude of the proximal pulling force has a maximum value of approximately one-fifth of the body weight. The large variation in the results of Endlein et al., however, does not allow for an accurate estimation of the pulling force magnitude.

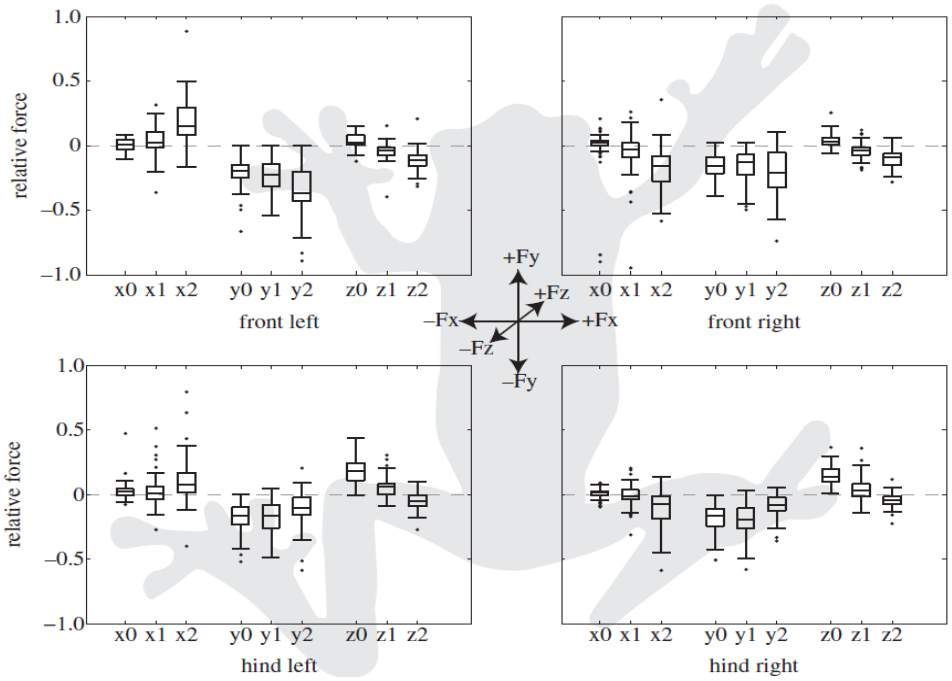

Figure 1.5: Relative force as force per body weight generated at the interface of the individual limbs. The resting position, first and second spread is indicated by the indexes 0, 1 and 2 respectively.

1.3.4. Tree frog inspired adhesive

From all the biomimetic adhesives described in the literature, the adhesive described by Xue et al.[73] is found to be the only tree frog inspired adhesive in which relatively stiff fibres are embedded in a compliant material matrix. The stress distribution in the composite material is described with a comparison between a fibre reinforced material in which the fibres and the base material are well-bounded and a material in which the fibres and the base material are not bound to each other.

The results obtained by Xue show that the stress magnitude is lower in a composite material in which the base material and the fibres are properly bound compared to a composite material with a reduced bonding between the matrix material and the fibres. Furthermore, the maximum stress in the well-bounded material is not located at the edge of the geometry but can be found at a certain distance (1-2 rows of pillars from the edge) from the material edge. A composite material in which the fibres are not bound to the base material has a maximum stress on the edge of the geometry as is also the case for homogeneous materials. The stress distributions for the material with the well-bound and the loose fibres are shown in Figures 1.6a and 1.6b respectively.

The difference in stress distribution between the two composite materials can be explained with the relatively good stress distribution of the stress over the material domain for the well-bound composite material compared to the material with the loose fibres. Good fibre-matrix bonding is described to reduce the magnitude of the stress concentrations and slow down the development of cracks between the material and the substrate that would ultimately lead to detachment from the substrate.

The stress concentrations in Figure 1.6a are located at the top of the nanopillars. This is caused by the transfer of stress from the contact surface to the relatively stiff fibres which bear more stress than the base material. Friction experiments show higher frictional performance for materials with well-bound fibres compared to materials without fibres or loose fibres.

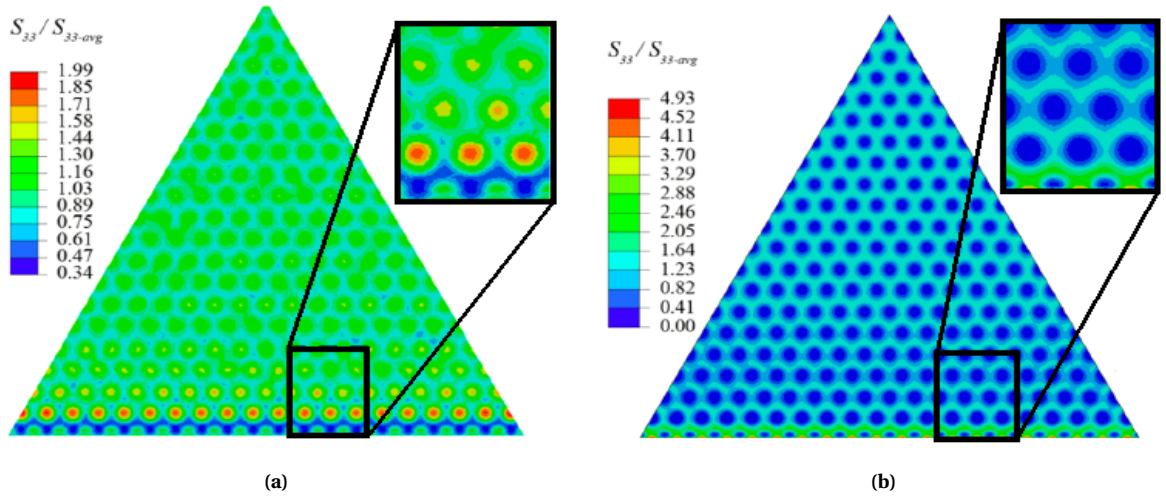

(a) **(b)**

Figure 1.6: Pictures from the modeling work by Xue et al. The stress distribution in (fig:Xue$_model_1$) $is the result of the internal bounding between the fibres and the base material. The stress distribution in (fig : Xue_m$ component is taken into account.

1.4. Goal & approach

This study focuses on recreating the mechanical behaviour present in the epithelial cell of the tree frog. The research question is: *'Do the tilted embedded keratin fibres in the epithelial cells and nanopillars prevent the development of stress concentrations on the adhesive pads of the tree frog?'*

To answer this question, this study investigates how stress is distributed in an epithelial cell and how this distribution affects the stress at the interface between the micro-pillars of the epithelial cell and the substrate. Furthermore, the influence of variation of mechanical properties of the composite structure of the epithelial cell is studied. These properties include the stiffness ratio between the fibres and the matrix material, the bonding between the fibres and the matrix and the fibre density.

To model the mechanics of the epithelial cell and the micro-pillars, a set of models is implemented in Comsol Multiphysics. The properties and purpose of these models are shown in Table 1.4.

The implementation of the modeling steps shown in Table 1.4 is discussed in Chapter 2. The results of these models are described in Chapter 3. The modeling results are validated with a set of experimental results. The experimental setup used to obtain these results is discussed in Chapter 4. The experimental results are discussed in Chapter 5.

Table 1.4: Different models, model purposes, boundary conditions and loading configurations used to resolve the different aspects of the mechanical behaviour of the epithelial cell.

Model	Model purpose	Loading & boundary conditions
I: Simplified geometry, discrete fibres	Evaluate influence of: - The fibre-matrix stiffness ratio - The fibre-matrix bonding - The fibre density	Simplified normal & tangential loads
II: Fabricated sample geometry discrete fibres	Evaluate influence of experimental boundary conditions & predict experimental results	Experimental loading conditions
III: Simplified geometry, HGO model	Validate HGO model	Simplified normal & tangential loads
IV: Epithelial cell geometry, HGO model	Evaluate stress distribution in epithelial cell	Loads derived from tree frog weight and posture

2
Modeling: methods

This chapter first discusses the implementation of a simplified model (model I from Table 1.4) which was used to evaluate the effect of the fibre-matrix stiffness ratio, the fibre-matrix bonding and the fibre density on the frictional and adhesive performance. The implementation of model II involved a discrete fibre geometry but required another set of boundary conditions to predict the outcome of the experimental results.

For model III, the same simplified geometry as model I was implemented. This model used the HGO material model and validated the use of the HGO material model for further use in model III. The purpose of model IV was to evaluate the stress distribution in the epithelial cell under loading conditions which were dependent on the tree frog behaviour. An analysis of the effect of the frog behaviour on the substrate-pad interface forces was carried out to determine the loading conditions. The interface forces were implemented in model IV to analyse the effect of the tree frog behaviour on the adhesional and frictional performance.

2.1. Discrete fibre models: model I

2.1.1. Fibre-matrix bonding

The space between the keratinous fibres in the epithelial layer as shown in Figure 1.2 is filled with connective tissue. The exact composition of this connective tissue and the degree of bonding to the fibres is not exactly clear. Given the well-hydrated nature of the tree frog terminal digits, however, the connective tissue can be safely assumed to be relatively compliant compared to the keratinous fibres [31]. It is therefore, possible that the material between the fibres offers relatively low resistance to inter-fibre sliding. Inter-fibre sliding was expected to modify the mechanical response, especially when the direction of the load is not in the direction of the fibres. The bounding of the fibres to the surrounding tissue is probably significantly better at the junctures between fibres and surrounding tissue at the ends of the fibres. The results about the influence of fibre-matrix bonding are only discussed for the discrete fibre model since the HGO model did not allow for variations in the fibre-matrix bonding.

To investigate the influence of fibre sliding, a thin elastic layer was added at the interface between the fibres and the matrix material. The stiffness of this layer was determined with the ratio $R_k = \frac{k_i}{k_f}$ with k_i for the stiffness of the thin elastic layer and k_f for the fibre stiffness. For $R_k = 1$ the thin layer had the same stiffness as the fibres. A higher elastic layer stiffness than the stiffness of the stiffest material in the geometry was expected to deform the thin layer less than the surrounding materials and with that, reduce the transfer of stress. Optimum stress transfer was expected for $R_k = 1$ while for $R_k << 1$, the thin layer was expected to be relatively compliant and allow inter-fibre sliding.

The model involved a simplified rectangular geometry in which relatively thin fibres were implemented as is shown in Figure 2.1. The mechanical behaviour of the fibres and the matrix material was simplified with a linear elastic material model. To investigate the influence of fixation of the fibre tips to the matrix material, the elasticity of the elastic layer at the fibre tips was set to $R_k = 1$.

2.1.2. Fibre-matrix stiffness ratio

The Young's modulus of the fibres in the discrete fibre model, E_f was set to $E_f = E_m + R_s E_m$ with E_m for the Young's modulus of the matrix material. The stiffness ratio R_s was varied in three steps from $R_s = 1$ to

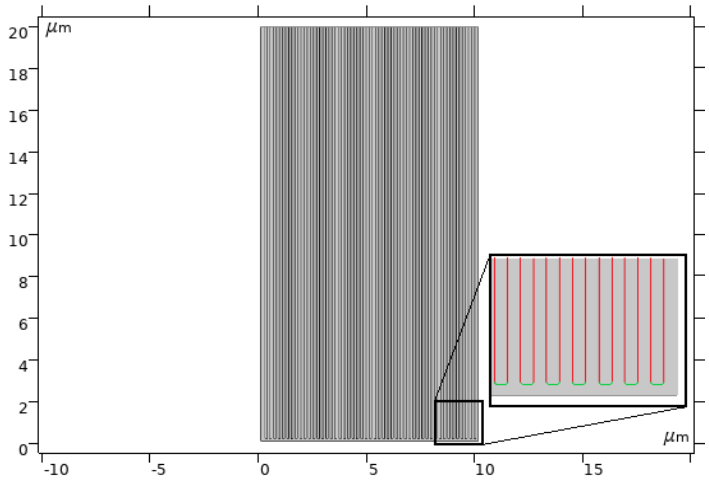

Figure 2.1: Simplified geometry with relatively fine fibres compared to the model used by Xue et al. [73]. For the 'free sliding' results, the value of R_k had an equal value for both the green and the red interfaces as shown in the insert. For the 'fixed tips' results, the stiffness of the thin elastic layer at the green interfaces was set to a constant value of $R_k = 1$ while the stiffness of the red interfaces was varied.

$R_s = 100$.

2.1.3. Geometry

The outline of the epithelial cell and its cell components is shown in Figure 1.3. The basic outline of the cell and the keratinous part of the cell were implemented in a 2D model which used a parameterized Matlab model in which the fibres were proportionally divided over the keratinous domain. The 2D model was implemented in Solidworks and transferred into Comsol Multiphysics. The Solidworks implementation is shown in Figure 2.2.

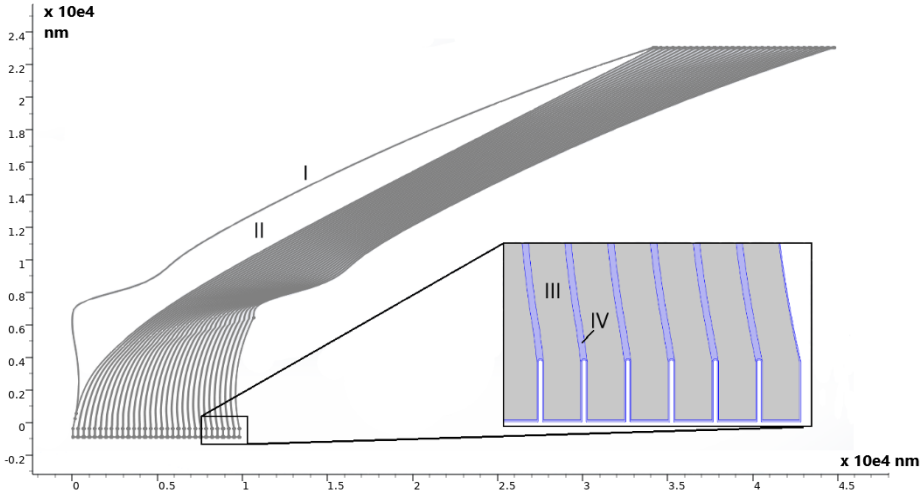

Figure 2.2: A representation of the geometry implemented in Solidworks. The keratinous structure is shown in the right part of the cell. The enlarged section shows the individual keratinous fibres. I represents the cornified cell envelope, II the lymph space, III a keratinous fibre and IV the space between the keratinous fibres with formed the matrix in which the fibres are embedded.

The geometry shown in Figure 2.2 had a relatively high level of complexity due to the presence of the

discrete fibres. Comsol Multiphysics needs a mesh to perform the finite element analyses. The numbers of elements of this mesh increases with the complexity of the geometry and the high level of complexity of the geometry shown in Figure 2.2 causes the mesh builder to form a mesh that contains a very large number of mesh elements which is shown in Figure 2.3. The number of mesh elements directly influences the convergence of the model. The fibre configuration shown in Figure 2.2, however, could be simplified into a rectangular geometry with a reduced number of fibres.

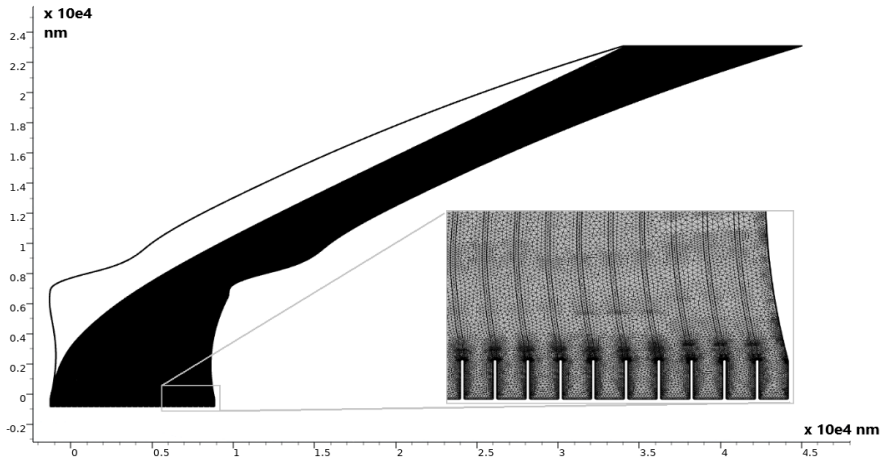

Figure 2.3: The mesh for the geometry in which one fibre bundle runs from every pillar. The mesh consists of 715790 domain elements and 118113 boundary elements.

The fibre density and the amount of fibres was varied between models to evaluate the consequences of these changes. The standard size of a simplified square fibrous domain was 10[μm] in width and 20 [μm] in height.

2.1.4. Boundary conditions

The points of attention that were addressed to obtain the required mechanical response for the simplified model with the rectangular domain were:

1. The lower boundary of the domain was assumed fixed. This boundary condition could be applied since the contact with the substrate was assumed to be constant. The constant contact with the substrate also allowed stress concentrations on the substrate do develop and made the mechanical behaviour more pronounced compared to a situation in which the lower boundary can deform. The geometry edges at which the boundary conditions were applied are shown in Figure 2.4.

2. Forces were applied on the upper boundary as would be the case when the micro-pillars are loaded by the tree frog.

3. The upper boundary was left free in translation in the x and the y-direction but was constrained in rotation. The rotational constraint was derived from the observation that the epithelial cells are concatenated and would therefore resist rotation of the upper boundaries. Fully constrained rotation is a simplified assumption of the real situation since the real situation would probably offer a small amount of rotational freedom.

4. The left and right sides of the geometry were left unconstrained. This was based on the observation that the micro-pillars of the epithelial layer are separated from their surroundings by a channel network. The interaction with the mucus present in these channels was not expected to significantly influence the mechanical properties of the micro-pillars.

5. In Section 1.3.2 the stiffness of the individual epithelial cell components is discussed. These stiffness values were also used in this model.

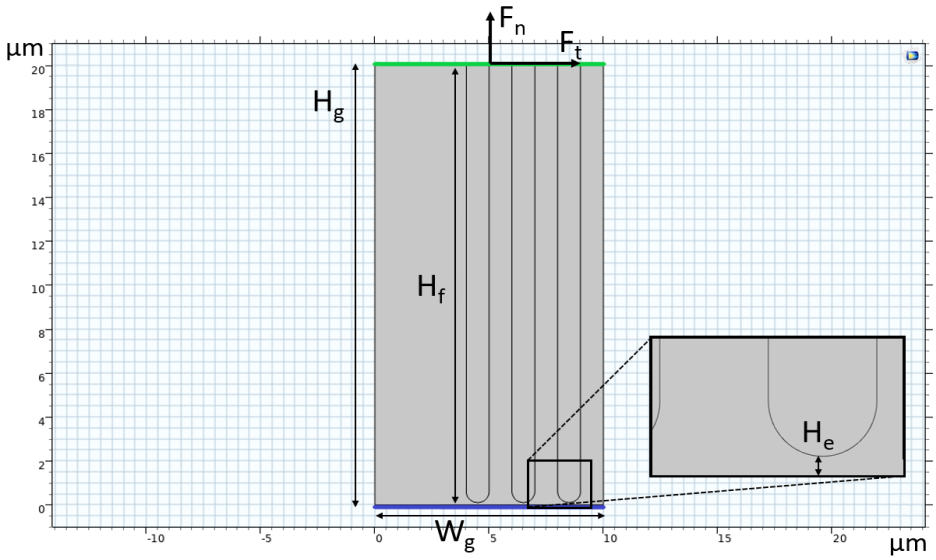

Figure 2.4: The dimensions involved in the boundary conditions of the simplified domain. The upper boundary is coloured green and is the point of application for the applied forces F_n&F_t. The lower boundary is colored blue. The height and width of the domain are represented by H_g&W_s respectively. H_f represents the length of the fibres and H_e represents the distance between the fibre tips and the lower boundary. The insert shows a close-up of one of the fibre tips. The influence of the degree of fibre-matrix bonding was evaluated with a much denser distribution of thinner fibres than is shown in this figure.

6. A linear elastic material model was implemented for the fibres and the matrix. It was found that the differences in the stress response between a hyperelastic and a linear elastic material model were very minor which validated the implementation of the linear elastic material model.

7. The length of the fibres and the gap between the fibre tips and the substrate were represented by H_f and H_e respectively. These parameters were kept constant for all the performed simulations. The thin layer ensured that the contact with the substrate was established with a continuous domain. This is a simplification of the real situation in which the contact is established with the thin cornified cell envelope which is also shown in Figure 1.3.

2.1.5. Model sensitivities

The smoothness and numerical instability of the solution was dependent on the number of mesh elements and on the discretization order. Numerical instability was caused by the Runge's phenomenon which causes oscillation at the edges of an interval when a polynomial interpolation is used [60]. This phenomenon can be countered by increasing the resolution of the mesh which increases the number of mesh nodes. A more efficient way is a mesh refinement study that increases the mesh locally at the locations where steep gradients are encountered. The adaptive mesh algorithm does smooth the response but takes too much mesh elements for the available memory to compute a fully smooth model response.

Another way to smooth the response is an increase in the discretization order of the displacement field. Increasing the discretization order also increases the memory needed for the computation which can causes memory errors. An increase in the discretization order, however, considerably smoothed the solution as is shown in Figure 2.5. This method was used to smooth out the response of the discrete fiber model.

The discrete fibre model did encounter non-linear behaviour for loading configurations in which shear and normal loads were simultaneously applied. To prevent the convergence issues caused by the non-linear behaviour and to shorten computation time, the estimates of the initial values of the dependent values were carefully chosen. Comsol Multiphysics uses these values as an estimate for the computational result and therefore benefits from an accurate prediction of these values.

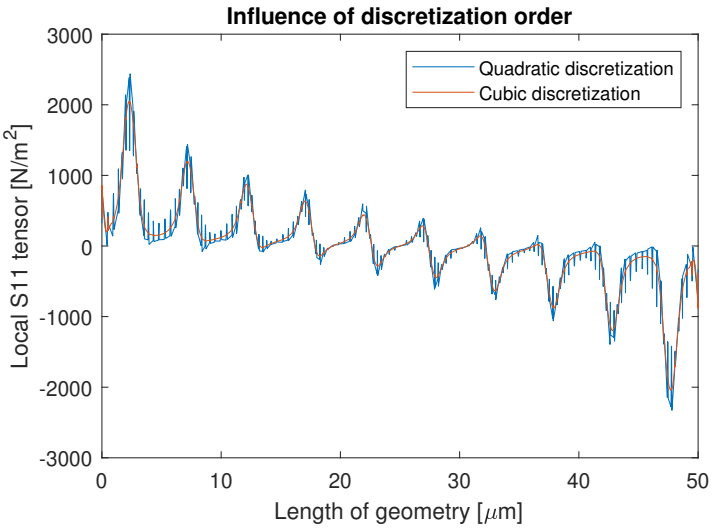

Figure 2.5: Model stress response for different discretization orders. The cubic discretization gives a smoother response than the quadratic discretization but is more computational demanding.

2.1.6. Data processing

The stresses of the discrete fibre model were evaluated at the lower boundary of the geometry. The values of the stress components were evaluated in a cut-line which was defined just above the lower geometry boundary at y = 0.001 [μm]. The S_{11} and S_{22} stress components were extracted from the Comsol simulation. The results were smoothed out using a moving average in the post-processing of the results.

2.2. Discrete fibre models: model II

The purpose of model II was to approach the experimental setup as close as possible while the other models were focused on approaching the mechanical behaviour in the cells and micro-pillars of the epithelial layer. Model II was used to confirm that the results obtained with model I could also be expected from the experimental results.

2.2.1. Boundary conditions

The main differences between model II and model I were:

- The material properties of the fibres and base material were set to realistic values for the ABS fibres and PDMS matrix material. The ABS fibre mechanics were implemented with a linear elastic material model with a Young's modulus of E = 1.19 [GPa], a Poisson's ratio of ν = 0.35 and a density of ρ = 1070 [kg/m^3]. For the PDMS matrix, a two-parameter Ogden hyperelastic material model with nearly incompressible material properties was implemented. The parameters to further define the material properties were derived from the work of Kim et al. [40] and are shown in Table 2.1.
- The shear load on the samples was implemented with a force distribution which acted at the right boundary of the sample base and equaled the sum of the applied pulling force and the moment caused by this pulling force. The magnitude of this sum varied over the length of the boundary as shown in Figure 2.6. The normal force was applied at the top of the geometry and the bottom of the geometry was fixed.

2.2.2. Model sensitivities

The smoothness of the solution for this model was influenced by the mesh density and the discretization order as is described for model I. The main difference between model I and model II was that the non-linear

Table 2.1: Parameters to define the Ogden hyperelastic material properties that were implemented to model the PDMS matrix material for the samples used to obtain the experimental results [40].

Matrix stiffness / Ogden parameters	Low stiffness	High stiffness
μ_1	63.49 [MPa]	0.0003428 [MPa]
μ_2	0.041 [MPa]	0.1316 [MPa]
α_1	$6.371e-10$	7.7991
α_2	3.811	3.6718

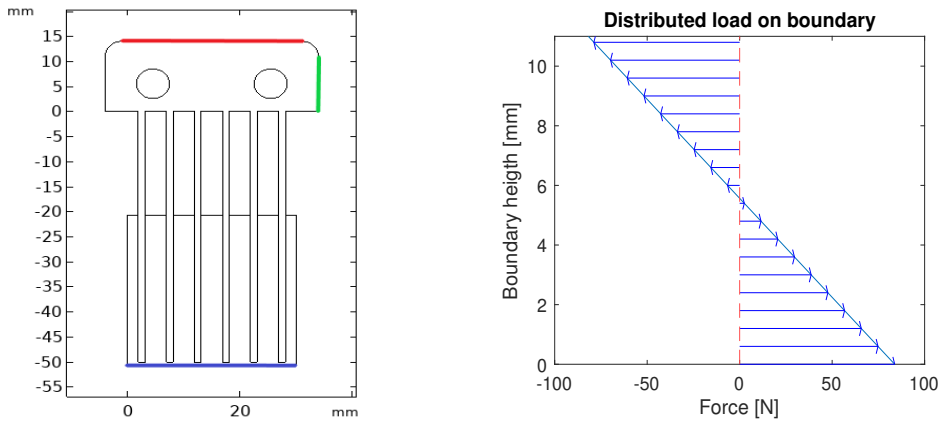

(a) **(b)**

Figure 2.6: The geometry of the model used for modeling the experimental setup and the load to simulate the applied moment in Figure 2.6a and 2.6 respectively. In Figure 2.6a, the normal force was applied to the red boundary and the blue boundary was constrained. The force on the green boundary is shown in Figure 2.6b.

material model causes geometric non-linearity for model II. To prevent convergence issues, the estimates for the initial values of the dependent variables were first determined by implementing an initial modeling step in which relatively small loads were implemented. The response of this initial modeling step was then used to estimate the values of the dependent variables. The non-linear solver configuration used an auxiliary sweep for a step-by-step introduction of the variables which caused the non-linear mechanics.

2.2.3. Data processing

The results of this model were measured and processed as described for model I.

2.3. HGO models: model III

The HGO model allowed the implementation of directional dependent and composite material properties in one continuous domain. This reduced the number of mess elements needed for the implementation of the material properties of the epithelial cell.

2.3.1. Background: HGO model fundamentals

The formulation of the possible linear material transformations for an orthotropic material is shown in Equation 2.1 which shows the stress vector σ, the strain vector ϵ and the fourth-order stiffness tensor C [25]. The material properties of an orthotropic material are different along the orthogonal axis of the material.

$$\sigma = C\epsilon,$$

With for σ, ϵ and C:

$$\sigma = \begin{bmatrix} \sigma_{11} \\ \sigma_{22} \\ \sigma_{33} \\ \sigma_{23} \\ \sigma_{13} \\ \sigma_{12} \end{bmatrix}, \quad \epsilon = \begin{bmatrix} \epsilon_{11} \\ \epsilon_{22} \\ \epsilon_{33} \\ 2\epsilon_{23} \\ 2\epsilon_{13} \\ 2\epsilon_{12} \end{bmatrix},$$

$$C = \begin{bmatrix} C_{1111} & C_{1122} & C_{1133} & 0 & 0 & 0 \\ C_{2211} & C_{2222} & C_{2233} & 0 & 0 & 0 \\ C_{3311} & C_{3322} & C_{3333} & 0 & 0 & 0 \\ 0 & 0 & 0 & C_{2323} & 0 & 0 \\ 0 & 0 & 0 & 0 & C_{1313} & 0 \\ 0 & 0 & 0 & 0 & 0 & C_{1212} \end{bmatrix},$$

With

$$C_{2211} = C_{1122}, C_{3311} = C_{1133}, C_{3322} = C_{2233} \tag{2.1}$$

Biological materials often have similar properties in two orthogonal directions which is caused by the (local) orientation of the fibres in these materials. The modifications needed to represent such a transversal isotropic material by the fourth-order stiffness tensor C from Equation 2.1 are shown in Equation 2.2 [25].

$$\begin{aligned} C_{2211} = C_{1122}, C_{3311} = C_{1133} = C_{3322} = C_{2233}, \\ C_{1111} = C_{2222}, \\ C_{2323} = C_{1313}, \\ C_{1212} = \frac{1}{2}(C_{1111} - C_{1122}) \end{aligned} \tag{2.2}$$

Equation 2.2 allows the implementation of direction-dependent material properties but represents only linear material deformations. Fibres in biological materials, however, often display non-linear material behaviour, are often much stiffer in tension than in compression [47] and can display strain-dependent elastic properties. Hyperelastic material properties can be described with several material models. Examples of such models are the neo-Hookean material model [54] and the Mooney–Rivlin model [52].

To model the non-linear properties of the materials present in the epithelial cell of the tree frog, a material model was needed that describes the mechanical behaviour of the fibres and the ground substance in which the fibres are embedded. The fibre orientation in the keratinous domain of the epithelial cell is a function of the location which makes the material properties direction and location dependent.

The HGO model introduced by Holzapfel et al.[36] allowed modeling of composite fibrous materials with anisotropic hyperelastic properties. These hyperelastic properties could be implemented for both the ground substance and for the embedded fibres. The equations for the HGO model describe the isochoric strain energy density which is defined as shown in Equation 2.3. The parameter W_1 describes the contribution of the material in which the fibres are embedded and W_4 describes the contribution of the fibres. Both parameters can be derived with Equation 2.4-2.10.

$$W_s = W_1 + W_4 \tag{2.3}$$

To construct the parameters W_1 and W_4, it is required to go back to some basic relations. The deformation of a material can be described with the deformation gradient **F** given in Equation 2.4. This gradient is composed of a parameter describing the rotation **R** and of a parameter which describes the translation from the undeformed to the deformed composition **V**. The left Cauchy-Green deformation tensor **B** can be constructed from the deformation gradient **F** and is shown in Equation 2.5. These basic equations can be used

to construct the invariant $\bar{\mathbf{I}}_1$ which is used to describe the incompressible material behaviour as shown in Equation 2.6. $\bar{\mathbf{I}}_1$ uses the jacobian $\mathbf{J}$ of $\mathbf{F}$ and the invariant $\mathbf{I}_1$ which is defined as $\mathbf{I}_1 = tr(\mathbf{B})$.

$$\mathbf{F} = \mathbf{VR} \tag{2.4}$$

$$\mathbf{B} = \mathbf{F}\mathbf{F}^T = \mathbf{V}^2 \tag{2.5}$$

$$\bar{\mathbf{I}}_1 = \mathbf{J}^{-\frac{2}{3}}\mathbf{I}_1 \tag{2.6}$$

The invariant $\mathbf{I}_4$ is dependent on the direction of the fibres and the local deformation gradient. Equations 2.7 and 2.8 show the short and the long notation of the invariant respectively. The invariant is composed of a vector field $\mathbf{a}$ which represents the direction of the fibres and the isochoric elastic Cauchy-Green tensor $\overline{C_{el}}$.

$$I_4 = \mathbf{a}\overline{\mathbf{C}_{el}}\mathbf{a} \tag{2.7}$$

$$\begin{aligned} I_4 = {} & a_1\overline{C_{el_{11}}}a_1 + 2a_1\overline{C_{el_{12}}}a_2 + 2a_1\overline{C_{el_{13}}}a_3 \\ & + a_2\overline{C_{el_{22}}}a_2 + 2a_2\overline{C_{el_{23}}}a_3 + a_3\overline{C_{el_{33}}}a_3 \end{aligned} \tag{2.8}$$

The isochoric elastic Cauchy-Green tensor $\overline{\mathbf{C}_{el}}$ as shown in Equation 2.10 is constructed from the local elastic Cauchy-Green tensor $\mathbf{C}_{el_{ij}}$ and the elastic volume ratio $\mathbf{J}_{el}$. Subscripts i and j express the local coordinates. $\mathbf{C}_{el_{ij}}$ is constructed from the inverse of the inelastic deformation gradient and the local Cauchy-Green tensor. The local Cauchy-Green tensor is constructed from the local deformation gradients as shown in Equation 2.9. This equation sums over n dimensions and uses the deformations in the i and j directions.

$$C_{l_{ij}} = \sum_{n=1}^{3} F_{ni}F_{nj} \tag{2.9}$$

$$\overline{\mathbf{C}_{el}}_{ij} = \mathbf{J}_{el}^{-\frac{2}{3}}\mathbf{C}_{el_{ij}} \tag{2.10}$$

The parameters $\overline{I}_1$ and I_4 can now be used to define the parameters from Equation 2.3. W_1 is the isotropic function which describes the isotropic behaviour of the material in which the fibres are embedded. W_1 depends on C_m and on the first invariant of isochoric elastic right Cauchy-Green tensor $\overline{I}_1$ as shown in Equation 2.6. The parameter W_4 represents the contribution of the anisotropic material properties. As shown in Equation 2.12, W_4 is dependent on the parameters k_1 and k_2 which respectively represent a stress-like material parameter and a dimensionless constant. The invariant I_4 is shown in Equation 2.8. The parameter k_2 represents the amount of non-linearity (strain stiffening) in the material.

$$W_1 = \frac{C_m}{2}(\overline{I_1}) - 3) \tag{2.11}$$

$$W_4 = \frac{k_1}{2k_2}(e^{k_2(I_4-1)^2} - 1) \tag{2.12}$$

2.3.2. Fibre-matrix stiffness ratio

Implementing a fibre-matrix stiffness ratio for the HGO model involved a ratio that relates the stiffness of the base material component C_m with the direction-dependent stiffness of the fibrous component k_1 and was defined as $R_{HGO} = \frac{k_1}{C_m}$. The modeling steps to explore the influence of R_{HGO} involved a simplified square geometry which was similar to the geometry shown in Figure 2.1 but without the fibres.

2.3.3. Geometry

The geometry of this model was similar in dimensions as the geometry implemented for models I & II but did not contain fibres.

2.3.4. Boundary conditions

The boundary conditions of model III were similar to the boundary conditions implemented for model I.

2.3.5. Model sensitivities

The HGO model response was influenced by numerical instability as is described for model I. The HGO model convergence was furthermore, sensitive to the implemented initial conditions, model properties and solver configurations. To increase convergence, a non-linear solver was used and the magnitude of the initial values of the dependent variables was set to the same order of magnitude of the solution magnitude for these variables as described for model II. An auxiliary sweep was used for a step-by-step introduction of the non-linear model mechanics.

2.3.6. Data processing

The results of this model were measured and processed in a similar way as described for model I.

2.4. HGO models: model IV

In Section 1.3.3 is described how tree frogs spread their limbs when an increase in adhesional performance is required. This model was used to evaluate the impact of limb spreading on the forces at the contact interface.

2.4.1. Background: tree frog behaviour

The forces acting on the epithelial layer of the adhesive pad were decomposed in adhesion forces and friction forces. These forces were respectively normal and tangential to the substrate. The magnitude of the forces that act on the tree frog was determined by the position of the frog and the weight of the frog. For a frog that is sitting on a vertical wall, a schematic representation of the forces is shown in Figure 2.7a. The adhesive pads of the tree frog are thus subjected to tangential ($F_{t,1}, F_{t,2}$) and normal ($F_{n,1}, F_{n,2}$) forces. The normal forces were for the largest part determined by the weight and the posture of the frog while the tangential forces could also be increased by the frog by proximal pulling on the limbs. The direction of the normal force in attachment point I was opposed to the direction of the normal force in point II. A schematic representation of the situation is shown in the free body diagram in Figure 2.7b.

The normal forces acting on the limbs of the frog could be fully defined using static equilibrium equations. The tangential forces, however, could not be easily determined because the problem is statically over-constrained and thus static indeterminate. Such problems can be solved when the mechanical properties of the rigid body are known. The mechanical properties of the body of the tree frog connecting the two attachment points are dependent on the tree frog and could therefore not be easily determined. Furthermore, the tangential forces can be manipulated by the frog itself.

The frog can create a force between the limbs with the application of a proximal pull. Proximal pulling is also described in Section 1.3.3 and is shown in Figure 1.4a-1.4c. The behaviour shown in this figure, is displayed by the frog when the substrate is rotated so that the frog needs a larger adhesional force to prevent falling off. The forces at the surface of the adhesive pads are shown in Figure 2.8. The proximal pulling forces $F_{p,1}$ and $F_{p,2}$ are oriented towards the center of gravity and can be decomposed in x and y-components.

The limb spreading influences the angles of attachment α_1 and α_2 which are shown in Figure 2.7b. The tangential forces on the adhesive surfaces of the frog were split up in a component representing the proximal pulling (F_p), and in components representing the rest of the tangential force on the adhesive surfaces ($F_{s,1}$&$F_{s,2}$). The magnitude of $F_{s,1}$&$F_{s,2}$ was unknown because the FBD of the frog is statically indeterminate and the mechanical properties of the frog body connecting the two points of attachment were unknown. The relations between these various force components are shown in Equation 2.13.

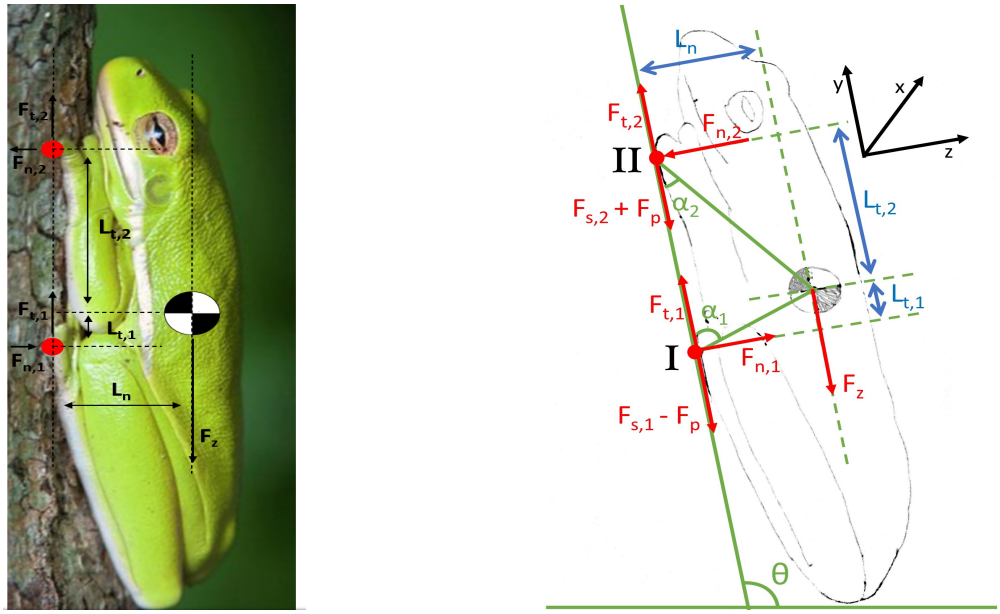

(a) (b)

Figure 2.7: Forces on a tree frog in resting position with in (2.7a) the Hyla Cinerea with the relevant forces and dimensions and in (2.7b) the free body diagram of the same situation

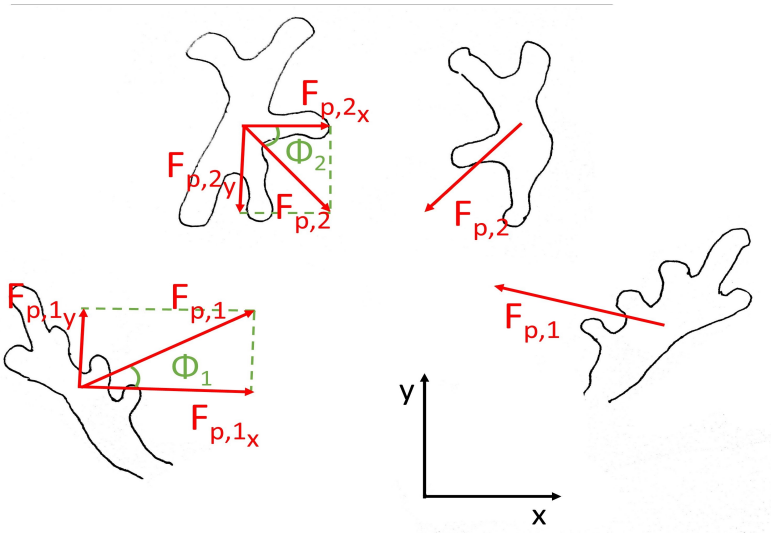

Figure 2.8: The forces on the frog feet seen from below. The proximal pulling forces $F_{p,1}$ and $F_{p,2}$ were decomposed in components in the x-direction ($F_{p,1_x}$ & $F_{p,2_x}$) and in components in the y-direction ($F_{p,1_y}$ & $F_{p,2_y}$).

$$
\begin{aligned}
F_{t,1} &= F_{s,1} - F_p, \\
F_{t,2} &= F_{s,2} + F_p, \\
F_z &= F_{t,1} + F_{t,2}
\end{aligned} \tag{2.13}
$$

A Matlab model was written in which three cases were defined:

- **Case 1** considered a frog that does not make use of proximal pulling. The mechanical properties of the frog body connecting the two points of attachment were assumed such that the tangential forces were

both equal to half the tangential component of the gravitational force $F_{t,1} = F_{t,2} = \frac{F_z}{2} cos(\frac{\pi}{2} - \theta)$. The normal forces were calculated using the relations given in Equation 2.14.

$$F_{n,2} = \frac{F_z(L_n cos(\frac{\pi}{2} - \theta) + L_{t,1} cos(\theta))}{L_{t,1} + L_{t,2}},$$
$$F_{n,1} = \frac{F_z cos(\frac{\pi}{2} - \theta) L_n - L_{t,2} F_{n,2}}{L_{t,1}} \tag{2.14}$$

- **Case 2** involved a situation in which the frog proximally pulls on its limbs. The magnitude of these pulling forces was derived from the work of Endlein et al. [18] which is also discussed in Section 1.3.3. It was assumed that the proximal pulling started when the frog performed its first spread. The proximal pulling forces increased to their maximal values when the frog performed its second spread. The angles of the first and second spread were taken from the work of Endlein et al. and were $\theta_1 = 106$ [deg] and $\theta_2 = 131$ [deg] for the first and second spread respectively. Equations 2.15 - 2.17 give the magnitudes of the pulling forces as a function of parameter R which resembled the ratio between the bodyweight of the frog and the magnitude of the pulling force. The value of this parameter was set to $R = 0.2$ as described in Section 1.3.3. The parameter ϕ_1 is the angle of the proximal pulling force as is shown in Figure 2.8.

$$\text{For } \theta < \theta_1,$$
$$F_{p,1_x} = F_{p,2_x} = F_{p,1_y} = F_{p,2_y} = 0 \tag{2.15}$$

$$\text{For } \theta_1 \leq \theta \leq \theta_2,$$
$$F_{p,1_x} = F_{p,1_x} = F_z \frac{R}{4},$$
$$F_{p,1_y} = tan(\phi_1) F_{p,1_x} \quad \& \quad F_{p,2_y} = tan(\phi_1) F_{p,2_x} \tag{2.16}$$

$$\text{For } \theta > \theta_2,$$
$$F_{p,1_x} = F_{p,1_x} = F_z R,$$
$$F_{p,1_y} = tan(\phi_1) F_{p,1_x} \quad \& \quad F_{p,2_y} = tan(\phi_1) F_{p,2_x} \tag{2.17}$$

- **Case 3** involved the pulling forces as in Case 2 but also included a positional adjustment of the frog due to the re-positioning of the limbs. For $\theta_1 \leq \theta \geq \theta_2$ the dimensions L_{t1} & L_{t2} were multiplied with a factor $\frac{3}{2}$ and parameter L_n was multiplied with a factor $\frac{3}{4}$. For the second spread, the parameters were multiplied with factors 2 and $\frac{1}{2}$ for L_{t1} & L_{t2} and L_n respectively. These values were based on a rough estimate derived from images of the tree frog during its different spreading positions as shown in Figure 1.4.

The forces involved in the three cases are shown in Figures 2.9a, 2.9b and 2.9c. The normal forces were independent of tangential forces and were the same for Case 1 and Case 2. The tangential forces which were dependent on the proximal pulling were different between Case 1 and Case 2. The value of the tangential components $F_{t,1}$ and $F_{t,2}$ increased with the first spread and with the second spread. The increase of the tangential force components after the first spread was relatively small compared to the increase at the second spread which was proportional to the magnitude of the proximal forces shown in Figure 2.9d. Case 3 shows the forces at the contact interface for a combination of proximal pulling and positional adjustment. For this loading configuration, the tangential component $F_{t,2}$ increased. The normal force components decreased due to the positional adjustment.

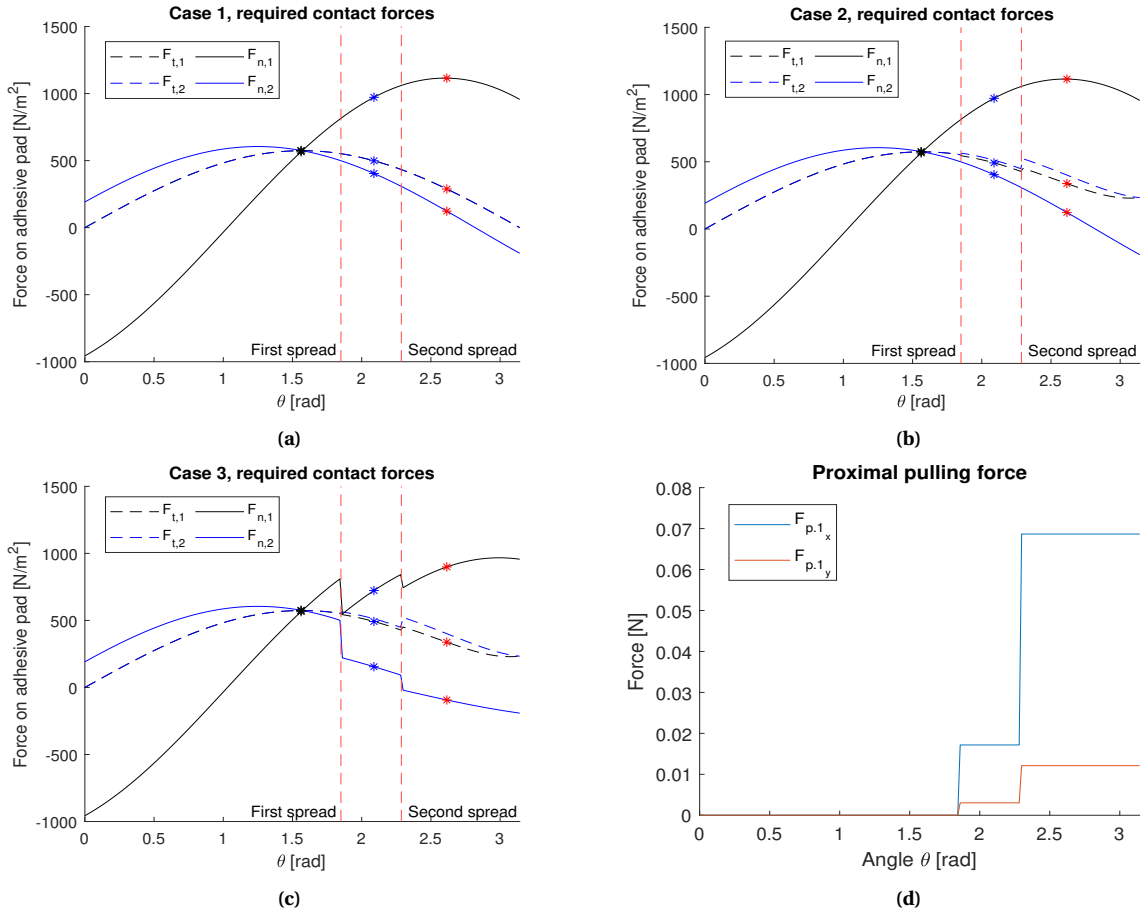

Figure 2.9: Required contact forces as a function of the the angle θ for the three cases. Case 1 in (2.9a) represented a default situation. In (2.9b), the proximal pulling was included and in (2.9c) positional adjustment was added. The proximal pulling forces for Cases 2 Case 3 are shown in (2.9d).

2.4.2. Fibre-matrix stiffness ratio

The fibre-matrix stiffness ratio for this model was implemented in a similar way as for model III.

2.4.3. Geometry

The working principle of the keratinous structure was not expected to be dependent on an exact number of fibres. The most important characteristic of the fibrous structure is that of an anisotropic material. Furthermore, it was expected to display non-linear material behaviour. The HGO material model allowed the implementation of anisotropic hyperelastic materials. With the HGO model, the material properties of the keratinous fibres were dependent on a location-dependent vector field. The streamlines of this vector field are shown in Figure 2.10.

2.4.4. Boundary conditions

The boundary conditions implemented in the epithelial cell model to obtain a mechanical response that agrees with the mechanical behaviour of an actual epithelial cell were:

1. The lower geometry boundary, highlighted in green in Figure 2.10 was fixed. This assumption was also implemented in the simplified rectangular geometry described in Section 2.1.4.

2. The upper boundary was loaded with the applied forces F_n&F_t. These forces resembled the perpendicular and tangential loads respectively. This loading configuration is a simplification of the real loading

configuration in which the loads would be more evenly distributed over the material domain.

3. The boundary conditions on the left and right cell boundaries were necessary to prevent unrealistic deformations in the y-direction. The relatively large distance in the x-direction between the point of application of the forces and the point of application of the reaction force on the base of the epithelial cell could cause a large deformation in the y-direction when a normal force was applied. In reality, however, the space under the epithelial cell is filled with other cells which will resist such a large deformation. To resemble the mechanics of the neighbouring cells, the lower boundary was subjected by a force per unit area in the x and y-direction. These parameters were represented by σ_{xx} and σ_{yy} which were defined as shown in Equation 2.18. In these equations, the displacement was represented by u and v. The parameter L represented an estimate of the maximum displacement and the parameter E_s represented the Young's modulus of the surrounding cellular material. The values of these parameters were 10 [μm] and 100 [kPa] respectively. The value of E_s was derived from the indentation experiments performed by Barnes et al. as shown in Table 1.1.

$$\begin{aligned} \sigma_{xx} &= \frac{-u}{L} E_s, \\ \sigma_{yy} &= \frac{-v}{L} E_s \end{aligned} \tag{2.18}$$

4. The upper boundary of the cell (in red in Figure 2.10) was constrained in rotation which resembled a realistic situation in which concatenated cells do not have full rotational freedom. This condition is also described in Section 2.1.4.

5. The lymph fluid in the domain enclosed by the blue boundaries in Figure 2.10 consists mainly out of water which was assumed an incompressible fluid. Equation 2.19 defined the pressure P on the boundaries of the lymph space as a function of the initial undeformed area A_0 and the variable area A of the domain. The surface area of the lymph domain was defined with an integration on the domain borders. The displacement of the lymph fluid was considered irrelevant and computationally demanding and therefore excluded.

$$P = A - A_0 \tag{2.19}$$

6. The mechanical properties implemented for the cornified cellular layer were based on the assumption that this relatively thin layer (10 [nm]) had linear elastic properties with a Young's modulus of 100 [MPa], a Poisson ratio of 0.4 and a density of 1000 [kg/m^3]. These properties were later varied to evaluate the influence of the stiffness of the cornified cell envelope.

7. The mechanical properties of the fibrous domain were implemented with the HGO model. The stiffness of the fibres is expressed by k_1 & k_2 and represents the amount of fibre nonlinearity. This nonlinear behaviour determined the amount of strain stiffening since the fibres in the implemented model did not have any stiffness in compression. The material stiffness of the base material was represented by the parameter C_m. Based on the stiffness values described in Section 1.3.2, the true stiffness of the connective tissue was expected to fall in a range of C_m = 1-10 [MPa] and the stiffness of the keratin was expected to be the range of k_1 = 1-10 [GPa]. Typical values for the parameter k_2 are between 0.5 and 5. The first approximation implemented in the model was k_2 = 1. The value of the parameter k_1 was varied as further discussed in Section 3.4.

2.4.5. Model sensitivities

The model sensitivities and the measures taken to counter solver non-convergence for this model were similar to the sensitivities and measures described for model III.

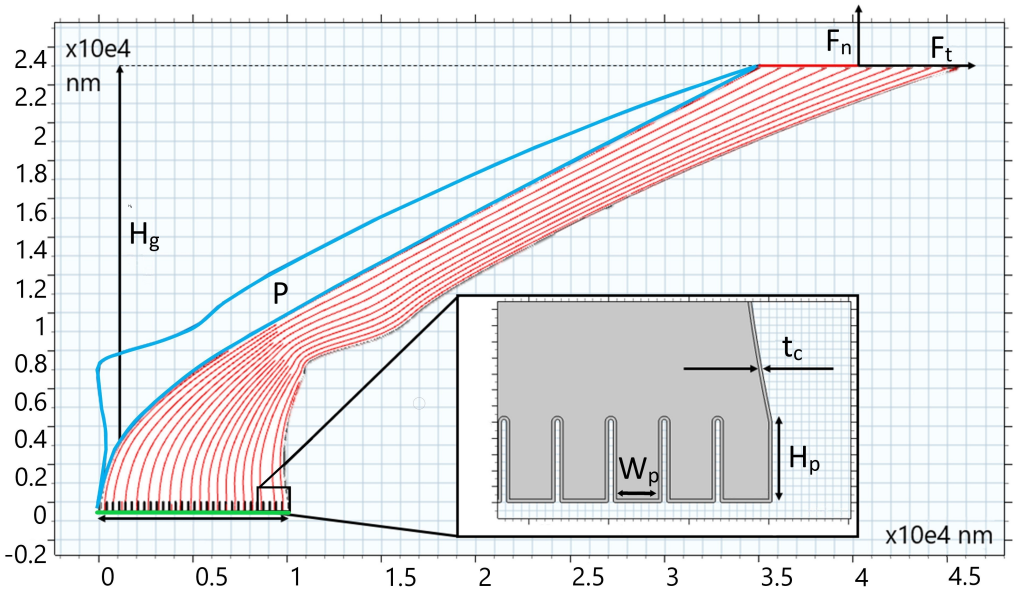

Figure 2.10: The dimensions and boundary conditions of the model which resembled the epithelial cell. The red streamlines indicate the direction of the keratinous fibres. The lower boundary is coloured green, the upper boundary is coloured red. The lower boundary was fixed while the external forces F_n&F_t were applied on the upper boundary. The blue boundaries enclose the lymph space. The lymph fluid exerted a pressure P on the boundaries of the lymph space. H_g and W_g represented the height and base width of the epithelial cell respectively. The epithelial cell model was enclosed by a cornified cell layer with thickness t_c and had a total of 30 pillars. The height and width of these pillars was represented by H_p and W_p respectively.

2.4.6. Data processing

The results of this model were measured in a cut-line that was positioned above the micro-pillars in the fibrous section of the epithelial cell at y = 1 [μm].

3
Modeling: results

This chapter describes the model validation and modeling results for each model from Table 1.4. The discrete fibre models are validated by comparing the results of model I & II with the results obtained by Xue et al. while the results of model III are compared with the results of model I to validate the use of the HGO model. After validation, the influence of the fibre-matrix bonding, the fibre-matrix stiffness ratio and the fibre density on the frictional and adhesive performance is discussed for each model. The results of model IV are focused on the influence of the tree frog behaviour on the adhesive and frictional performance of the epithelial cell.

3.1. Discrete fibre models: model I

3.1.1. Validation

For validation, a model with a rectangular domain, uniform elastic material properties and a fixed base is considered. When this model is loaded in tension, the stress concentrations can be found at the corners of the geometry as is shown in Figure 3.1. The S_{22} stress component considered is equivalent to the S_{33} stress component considered by Xue et al. as shown in Figure 1.6a and 1.6b.

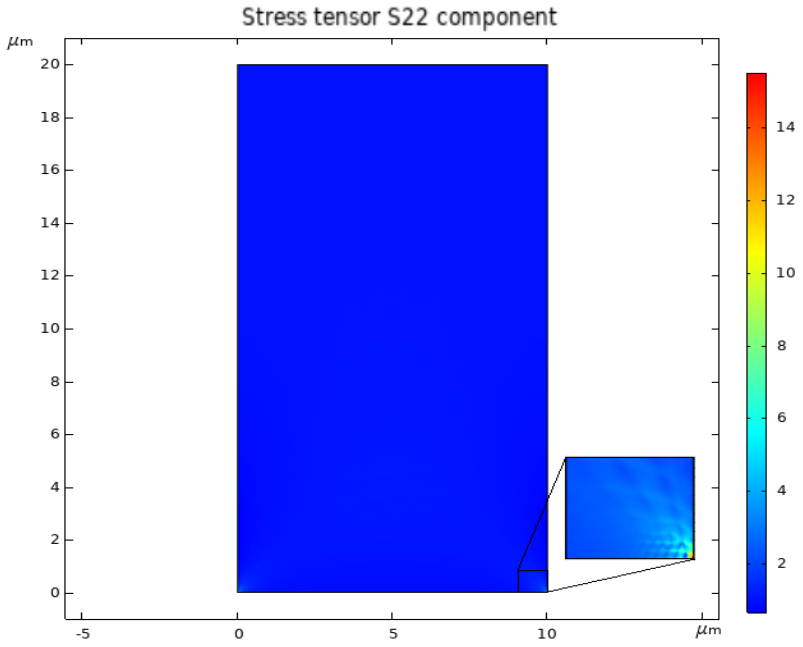

Figure 3.1: An uniform elastic domain with a fixed base loaded with a vertical load on the upper boundary. The stress concentrations appear in the lower right and left corners. The stress concentration in the lower right corner is shown in the insert.

The stress distribution in Figure 3.1 can be compared with the stress distribution in a domain in which fibres are implemented. Figure 3.2 shows a domain in which coarse fibres are implemented. The stress in this model is strongly influenced by the location of the fibre reinforcement. The most important observation is that the fibre reinforced model has a much lower value for the stress in the corners of the domain. A reduction

in peak stress increases the adhesive strength of the material since the stress is better divided over the contact interface compared to the uniform domain shown in Figure 3.1. The stiffness of the base material used for this model is 2 [MPa] and the stiffness of the fibres is set to 200 [MPa]. A Poison's ratio of 0.49 is implemented for the base material and the fibres.

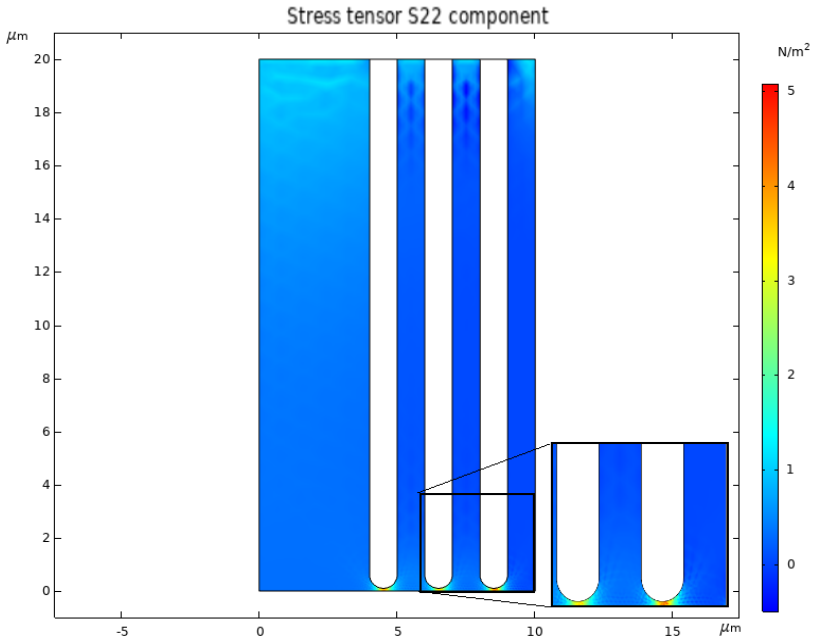

Figure 3.2: A composite model with coarse fibres implemented in a relatively soft base material. The loading and boundary conditions of this model are similar to the model from Figure 3.1.

The stress concentrations shown in Figure 3.2 are very similar to what is shown in Figure 1.6a. In both models, a stress concentration occurs between the fibres and the contact surface. When the maximum of the stress magnitude is compared between Figure 3.1 and Figure 3.2, it appears that the magnitude of the stress below the fibres in Figure 3.2 is considerably lower than the magnitude of the stress in the lower right corner of the geometry shown in Figure 3.1. The maximum of the stress found in the composite material is a factor 3 lower than the maximum value of the stress in the continuous material domain.

These observations confirm that the stresses in the simplified composite model are indeed lower than the stresses in a model with similar dimensions and homogeneous material properties. Furthermore, it is observed that the location of the maximum stress shifts from the corner of the geometry to a location under the fibres. These observations are also described by Xue et al. and validate the use of models I & II.

3.1.2. Fibre-matrix stiffness ratio

As shown in Figure 3.3, the magnitude of the S_{11} and S_{22} stress components is the lowest for $R_s = 100$ when the geometry is loaded with a normal force. For this stiffness ratio, the stress peaks at the ends of the fibres are larger in magnitude than for the smaller values of R_s. The stress in the corners of the geometry, however, has a much smaller magnitude for $R_s = 100$ than for the other stiffness ratio's.

For shear loading conditions which apply the load perpendicular to the fibres, the lowest magnitude of the stress components S_{11} and S_{22} is found for $R_s = 10$ as shown in Figure 3.4 and is caused by the relatively high stress peak at the location of the last fibre for $R_s = 100$. The stress magnitude at the edge of the domain however is found for $R_s = 100$.

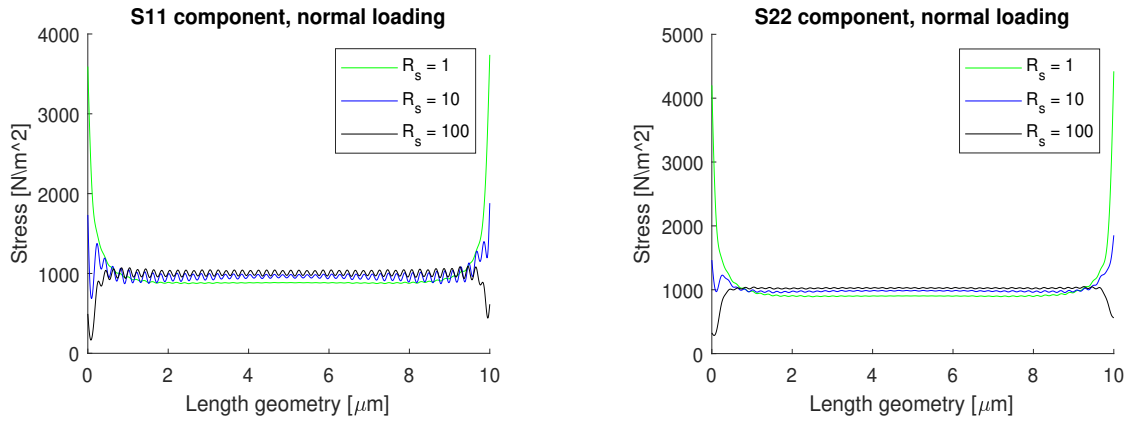

(a) **(b)**

Figure 3.3: The S_{11} and S_{22} force components measured at the lower boundary of geometry 2.1 shown in (a) and (b) respectively.

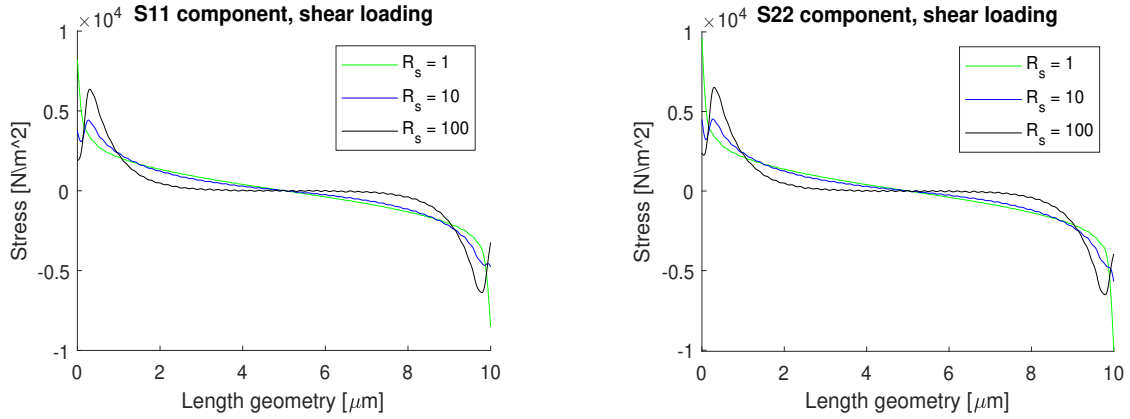

(a) **(b)**

Figure 3.4: The S_{11} and S_{22} force components measured at the lower boundary of geometry 2.1 shown in (a) and (b) respectively.

3.1.3. Fibre-matrix bonding

When loading is applied in the normal direction, the stress distribution at the lower domain boundary is considerably smoother for $R_k = 1$ compared to $R_k = 1e-6$ for the models involving fixed tips and free sliding fibres as shown in Figure 3.5. The absolute magnitude of the S_{11} and S_{22} stress components at the right and left edges of the geometry is the highest for the fixed tips with a low value for the parameter R_k. For the free sliding tips, however, both stress components are the smallest for the lowest value of R_k.

The magnitude of the stress components in the geometry under normal loading conditions does not show a peak at one of the corners of the geometry. This is probably caused by the fine fibre distribution which reduces the magnitude of stress peaks for individual fibres and relieves the stress from the domain corners by directing the stress from the corners to fibres.

The location of the stress transfer can be visualized with the location dependent deformation of the domain. The effect of the reduced stress transfer along the length of the fibres is observed in the larger strain in the y-direction for smaller values of R_k as is shown in Figures 3.6a & 3.6b.

The free sliding fibres with the lowest stiffness of the interfacial layer display the largest stress magnitudes for both stress components under normal loading conditions which is probably caused by the reduced stress transfer between fibres and matrix for low values of R_k. The reduced stress transfer along the fibres forces the

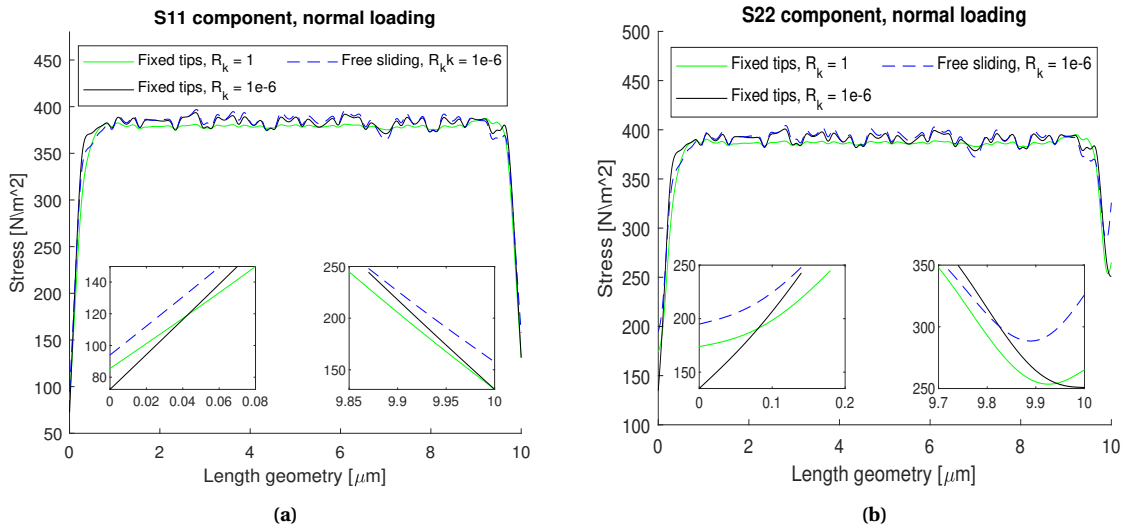

Figure 3.5: The S_{11} and S_{22} force components measured at the lower boundary of geometry 2.1 shown in (a) and (b) respectively. The normal load is applied at the top boundary of the geometry. The inserts in both figures show the forces near the geometry left and right corners.

stress transfer to the top of the fibres as is shown in Figures 3.6c & 3.6d.

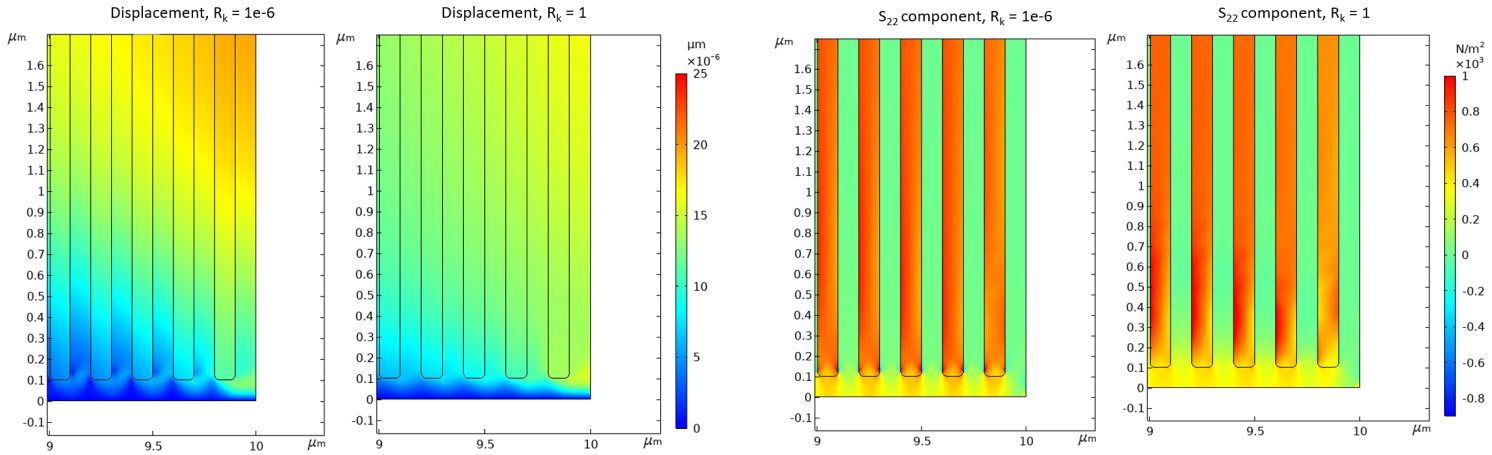

Figure 3.6: The displacement and stress in the right corner of the geometry shown in Figure 2.1 for normal loading conditions. Sub-figures (a) and (c) show the displacement and S_{22} stress component for $R_k = 1e-6$ while sub-figure (b) and (d) display the displacement and strain for $R_k = 1$.

In Figure 3.6a is shown that reduced fibre-matrix bonding results in a difference in material displacement between the fibres and the matrix material. For good fibre-matrix bonding, the gradient of the strain is much lower at the fibre-matrix interfaces. As a result of this difference in strain distribution, the S_{22} component is considerably higher at the tips of the fibres for $R_k = 1e-6$ than for $R_k = 1$ as shown in Figures 3.6c and 3.6d.

For shear loading, the S_{11} and S_{22} stress component at the edge of the geometry are higher for a lower value of R_k and the stress curves show a steeper increase near both edges of the geometry as shown in Figure 3.7. The high stress magnitude for low values of R_k is probably caused by a reduced stress distribution over the length of the geometry.

For $R_k = 1e-6$, a relatively large difference between the stress magnitudes for the 'free sliding' model and

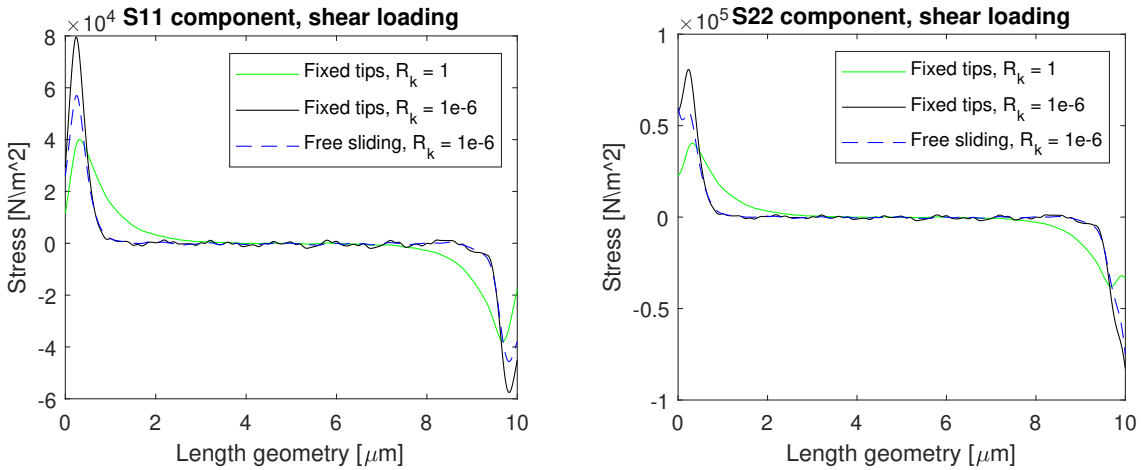

Figure 3.7: The S_{11} and S_{22} force components measured at the lower boundary of geometry 2.1 shown in (a) and (b) respectively. The shear load is applied at the top boundary of the geometry.

the model with the fixed fibres tips can be observed in the left corners of both subplots of Figure 3.7. This difference is probably caused by the large difference in the bonding along the length of the fibres and at the fibres tips for the model with the fixed tips and $R_k = 1e-6$.

3.2. Discrete fibre models: model II

3.2.1. Validation

This model uses a similar discrete fibre model as is implemented for model I and is therefore validated with the validation described for model I.

3.2.2. Fibre-matrix stiffness ratio

This model is used to predict if the effect of the fibre-matrix stiffness could also be expected for the samples used for the experimental results. The results of this model confirm that the influence of the fibre-matrix stiffness ratio, as described above for model I, can also be expected for the samples.

3.3. HGO models: model III

3.3.1. Validation

The HGO model is a simplified version of a fibre reinforced material in which the fibres are relatively thin and everywhere present such that the directional properties of the fibres are present everywhere in the material. For validation of the HGO material model, this model is compared with the model of Xue et al. which is described in Section 1.3.4.

The validation of the HGO model is divided into several steps in which the fibre density is increased from a few discrete fibres with finite thickness to an infinite number of infinitely thin fibres. The S_{22} component of the stress response of the different models is shown in Figure 3.8.

1. The first step of the validation involves the discrete fibre model discussed in Section 3.1 which involves only a few and relatively thick discrete fibres which are well bounded to the matrix material. The largest magnitude of the stress is observed between the fibres and the contact surface.
2. The second step involves a model in which more and thinner fibres are present. The results from this

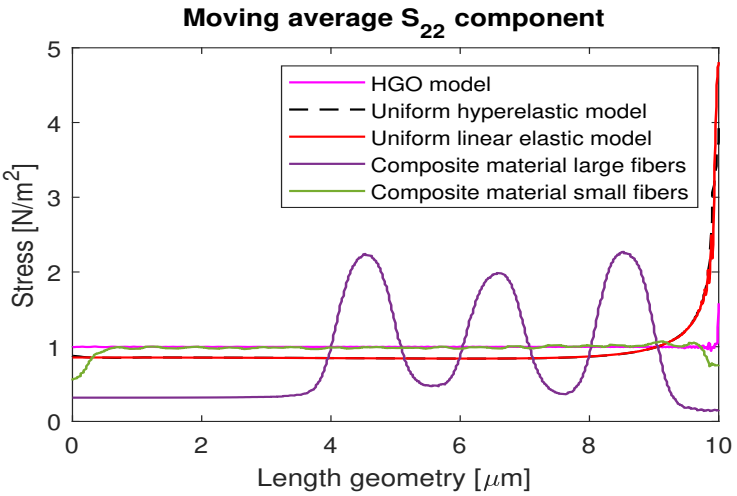

Figure 3.8: The S_{22} component of the stress along the length of the geometry for different material models. The models were all loaded with an equal force in the y-direction while the lower boundary was fixed. The stress response of the uniform linear elastic model and the uniform hyperelastic model are very similar to each other and are added for comparison with the composite material models and the HGO material model.

model show that the stress concentrations are still located at the tips of the fibres. The magnitude of the stress at the tips of the fibres, however, is much lower compared to the stresses observed for the coarse fibre model. The mechanical behaviour of the fine fibre model shows that a finer fibre configuration is beneficial for the magnitude of the contact stresses. The stress drops at the edge of the geometry where no fibres are located.

3. Based on the stress distribution of the fine fibre model, the stress distribution of the HGO model can be expected to be uniform over the whole length of the domain since the mechanical properties of the fibres are present everywhere in the geometry. The stress response of the HGO model shown in Figure 3.8 does meet this expectation. This model is set up with the parameters k_1 = 2 [MPa] and k_2 = 200 [MPa]. The largest difference between the discrete fiber model and the HGO model is observed near the boundary of the geometry and is probably caused by the absence of fibres near the boundary of the geometry for the fine fibre model. The peaks of the HGO model near the right edge of the boundary are caused by numerical instability and will be discussed in Section 2.3.5.

The modeling results discussed above validate the use of the HGO model for a geometry that would otherwise be filled with fine fibres. The validation described above, however, only validates the HGO model for a configuration in which the load is applied in the direction of the fibres. The validation, therefore, needs to be elaborated to investigate the validity of the HGO model for a case in which the geometry is not loaded in the direction of the fibres.

Figure 3.9 shows the S_{22} stress component for several modelling steps implemented in a simplified geometry that is loaded with a force in the x-direction (perpendicular to the direction of the fibres) and with a force in the y-direction. The stress values of the models loaded in tension are comparable with the stress values shown in Figure 3.8. The model results of the models loaded with a normal and a shearing force show that a shearing force considerably increases the S_{22} and S_{11} stress components in the geometry. The S_{13} component is zero along the whole length of the lower geometry boundary. Figure 3.9 shows the stress in the lower left corner of the geometry while the same effects in the stress response can also be observed in the lower right corner.

The difference between the stress distribution for the HGO model and the composite model increases with the introduction of the shear force. When loading a geometry like the geometry shown in Figure 3.1 with a force in the x-direction while the bottom is fixed, a moment is created. A moment introduces reaction forces in the y-direction from which the magnitude and forces are dependent on the location in the geometry. These reaction forces are the largest at the right and left boundaries of the geometry as shown for the S_{11} and S_{22} stress components in Figure 3.9 which are the largest near the lower right and left corners of the geome-

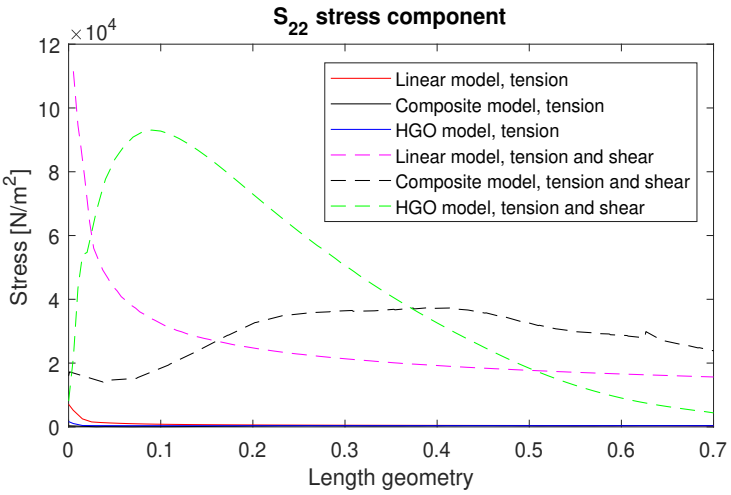

Figure 3.9: Stress response of the linear material model, the fine fibre model and the HGO material model for different loading configurations.

try. The forces in the x-direction are the sum of the shear forces and the forces induced via the deformations caused by the forces in the y-direction. The forces induced by the deformation of the material are dependent on the Poison ratio.

Figure 3.10 shows the stress components for a rectangular geometry with the same dimensions as shown in Figure 3.1. This geometry is fixed at the lower boundary and the right boundary is loaded with a force in the x-direction. From these figures the following observations can be done:

1. In the right subplot of Figure 3.10b is shown that the S_{22} component for the HGO model, when loaded in compression and shear, is very similar to the S_{22} component for the linear model for similar loading conditions. This can be explained by the absence of direction dependent properties for the HGO model when loaded in compression. Without these properties, the HGO model acts as a pure solid with a Neo-Hookean material model. The stress response of such a model is very similar to the response of a linear elastic material model for the boundary and loading conditions used in this validation simulation.

2. In the left subplot of 3.10b is shown that the different variations of the HGO model do have a stress peak in the left corner of the geometry which is probably caused by the strain stiffening properties of the HGO model. The effect of strain stiffening properties can be expected at the left corner of the geometry due to the reaction forces implied by the imposed moment which are in the direction of the strain stiffening material model properties.

3. The S_{11} component in the corners of the geometry, as shown in both subplots of Figure 3.10a, follows the deformation that is caused by the S_{22} component. The deformation at the left edge is relatively low due to the strain stiffening effect discussed above and probably is the reason why the peak of the S_{11} component occurs right before the left edge of the geometry as is shown in the left subplot of Figure 3.10a.

4. The stress components of the linear composite model in the left corner of the geometry shown in the left subplots of Figure 3.10a & 3.10b are much lower than the stresses found for the other material models. The reason for the higher performance of the composite model is probably the buffering nature of the compliant material situated at the edge of the geometry for the discrete fibre model geometry. The linear composite model has more strain at the edges than the HGO model which does not result in higher values for the S_{11} and S_{22} stress components because of the buffering nature of the outer compliant layer present at the edge of the composite linear model. The relatively low strain for the HGO model can be explained by the strain stiffening effect.

5. The strain stiffening composite model is similar to the linear composite model but has fibres that display non-linear strain stiffening behaviour. Strain stiffening behaviour is also discussed for other biological materials [36]. The mechanical properties of the fibres are similar to these of the HGO model

with $C = e$ used in Equation 3.1. The S_{11} and S_{22} components found for the strain stiffening composite model show that the strain stiffening leads to higher stress at the top of the fibres as shown in the left subplots of Figures 3.10a & 3.10b. The directional dependence of the strain stiffening properties, however, leads to higher values for the S_{11} and S_{22} components in the right corner of the geometry as shown in the right subplots of Figures 3.10a & 3.10b. It is observed for this model that the buffering nature of the compliant layer at the left edge of geometry prevents the development of stresses.

The S_{11} and S_{22} stress components shown in Figures 3.10a & 3.10b are plotted for three variants of the HGO model to provide insight into the strain stiffening properties of the HGO model. The strain stiffening behaviour of this model is determined by Equation 2.12 which can also be written as shown in Equation 3.1. The effects of varying the parameter C are shown in Figures 3.10a & 3.10b. From these figures it is observed that the stress in the x-direction can be brought closer to the response of the fibrous model by tuning the exponential function that determines the W_4 component of the HGO model.

$$W_4 = \frac{k_1}{2k_2}(C^{k_2(I_4-1)^2} - 1)(I_4 > 1) \tag{3.1}$$

The reduction of the peak magnitude of the S_{11} component is most probably caused by the decreased strain at the locations where the strain stiffening occurs. The S_{22} component of the stress in these locations does not match the response of the fibrous model. The slope of this component, however, is affected by the tuning of the parameter C as shown in the left subplot of Figure 3.10b.

The tuning of the W_4 component of the HGO model gives the best results for the default value e for the parameter C. Values higher or lower than e give a worse result in terms of the stress peak shown in the left subplot of Figure 3.10a. The maximum value of the S_{22} component shown in the left and the right subplot of Figure 3.10b is the lowest for the smallest value for C. This can be explained by the reduced effect of the strain stiffening for this value. The magnitude of C, therefore, determines the ratio of the S_{11} and S_{22} components.

In addition to the tuning of the W_4 component by modifying C from Equation 3.1, the parameters k_1, k_2 and C_{10} which define Equations 2.11 and 2.12 can be modified as well to match the expected material properties of the epithelial layer of the tree frog terminal digits with the HGO model.

The observations in this section point out that the HGO model differs from the discrete fibre model when the load on the geometry causes a non-uniform distribution of forces at the interface between the geometry and the substrate. This is caused by the strain stiffening of the HGO model and the buffering nature of the compliant material present along the edges of the composite material model.

Modeling a complex geometry with a large number of mesh elements as is shown in Figure 2.2 requires a material model in which individual fibres are not present. The HGO model meets this requirement but differs from the (strain stiffening) composite model as discussed above. These differences are taken into account when discussing the modeling results of the model that incorporates the geometry shown in Figure 2.2.

3.3.2. Fibre-matrix stiffness ratio

The mechanical response of the geometry upon implementation of a normal force at the top of the geometry is expressed in the S_{11} and S_{22} stress components as shown in Figure 3.12. The S_{11} stress response in Figure 3.11a is similar to the response for the geometry with the discrete fibres for a normal loading configuration as shown in Figure 3.3a. The response of the S_{22} component for the normal load shown in Figure 3.11b, does not display a decrease in the stress magnitude at the corners of the geometry for $R_{HGO} = 100$ and with that, differs from the response of the discrete fibres shown in Figure 3.3a. The S_{11} and the S_{22} components indicate that a high value of R_{HGO} reduces the stress response at the lower boundary of the geometry.

The S_{11} and S_{22} components of the stress response for shear loading are shown in Figures 3.12a and 3.12b respectively. In the left insert of Figure 3.12a, is shown that the magnitude of the S_{11} component is reduced for a larger value of R_{HGO}. The peak in the stress shown for $R_{HGO} = 100$ is comparable in appearance to the peaks visible in the stress magnitude for the discrete fibres shown in Figure 3.4a. The gradient magnitude

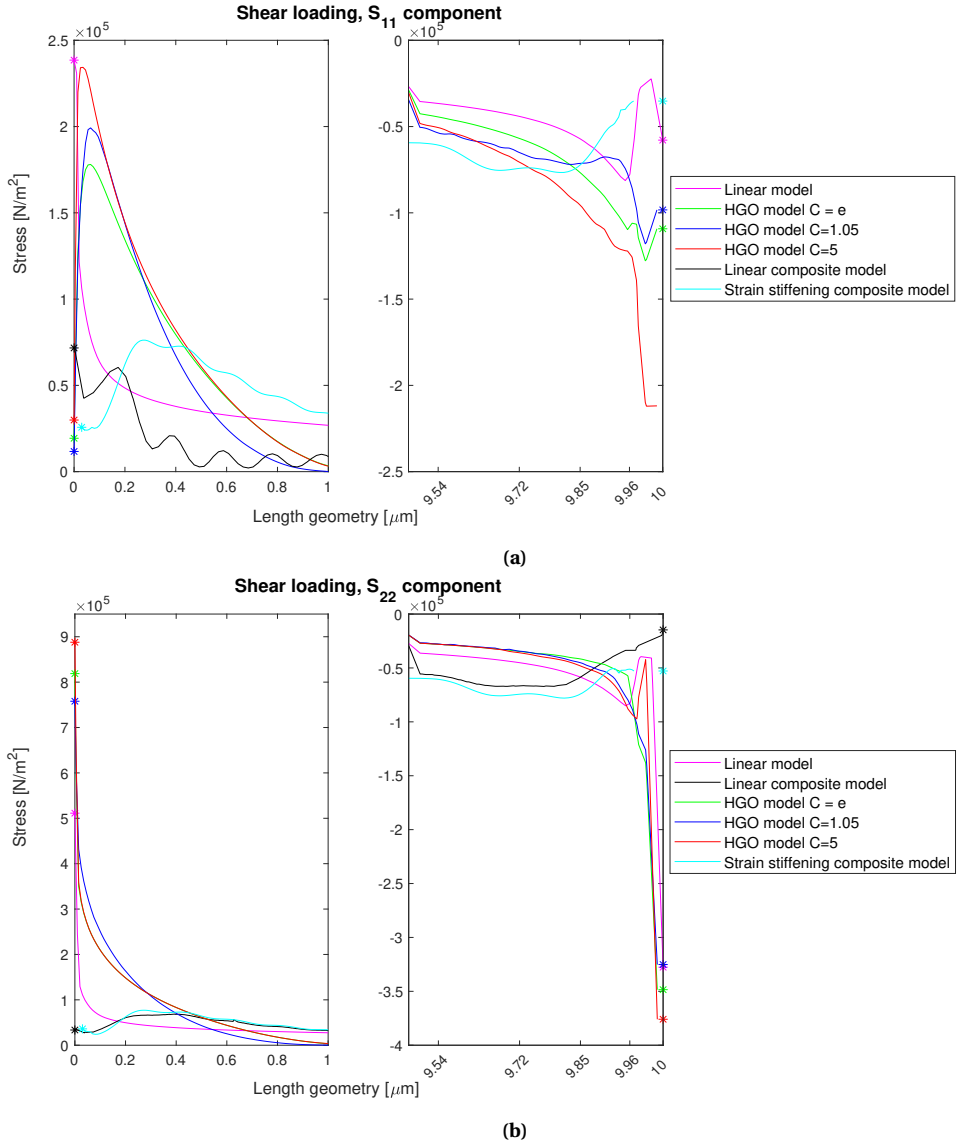

Figure 3.10: The S_{11} and S_{22} stress components in the x-direction and y-direction for a shear loaded configuration of the simplified HGO model. The asterisks at the start and the end of the curves mark the value of the stress components at the outer edges of the geometry.

of the stress response near the left corner of the geometry is furthermore, larger for $R_{HGO} = 100$ than for $R_{HGO} = 10$ and $R_{HGO} = 1$. The HGO model does not incorporate strain stiffening behaviour when the material is compressed and acts as a homogeneous hyperelastic material for compressive loads which explains the stress response in the right corner of the geometry which differs from the response in the left corner. The stress response in the right corner is not further considered since a sample is not likely to detach from the substrate when loaded in compression.

The magnitude of the S_{22} stress component at the left corner of the geometry is larger for larger values of R_{HGO}. The benefit of a larger value of the fibre-matrix stiffness ratio, as shown for the discrete fibre models for both normal and shear loading configurations, is therefore not observed for the shear loaded HGO model. The S_{11} component for the shear loaded HGO model does benefit from a higher value of R_{HGO} but this is not reflected in the S_{22} component which is higher for larger values of R_{HGO} for shear loading. A possible explanation for this observation is that for a smaller value of R_{HGO}, the deformation of the geometry is increased by the moment that is imposed on the geometry by the shear load. A higher value of R_{HGO} does not decrease the forces in the y-direction but it does decrease the strain in the geometry, and with that, the magnitude of

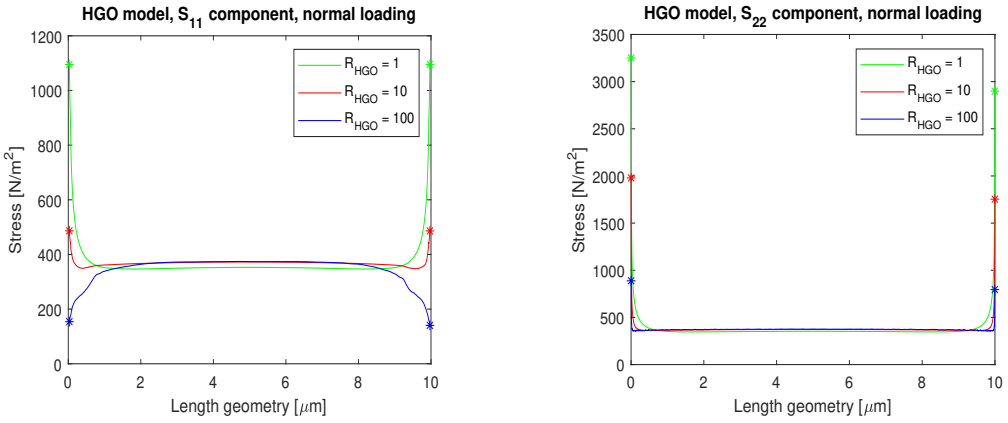

Figure 3.11: The S_{11} and S_{22} force components measured at the lower boundary of the geometry in (a) and (b) respectively. The asterisks show the magnitude of the stress components at the right and left edges of the geometry.

the S_{11} component.

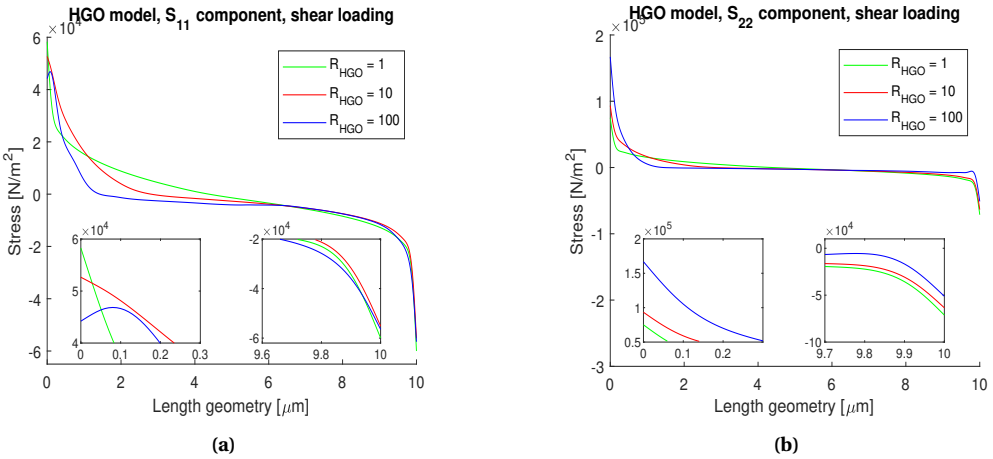

Figure 3.12: The S_{11} and S_{22} force components measured at the lower boundary of the geometry in (a) and (b) respectively. The inserts show a close-up of the stress components at the left and right edges of the geometry.

3.4. HGO models: model IV

3.4.1. Epithelial cell stresses

The epithelial cell model is used to evaluate the effects of strain-dependent material properties. These properties, together with the boundary conditions discussed in Section 2.4.4, determine the load on each micro-pillar in the epithelial layer of the tree frog. The mechanical behaviour of the epithelial cell is shown in Figure 3.13 which shows the Von Mises stress in the epithelial cell which is mainly determined by the S_{22} stress component.

The strain stiffening behaviour in the geometry follows the streamlines of the curvilinear coordinates implemented in the model as shown in Figure 2.10. The stress concentration along the left outer geometry edge marked with (1) in Figure 3.13 follows these streamlines. Furthermore, the tension along the left boundary of the geometry causes a stress concentration in the leftmost micro-pillar marked with (2). Such stress concentrations are also observed in the left corners of the other micro-pillars of the epithelial cell and are marked with (4).

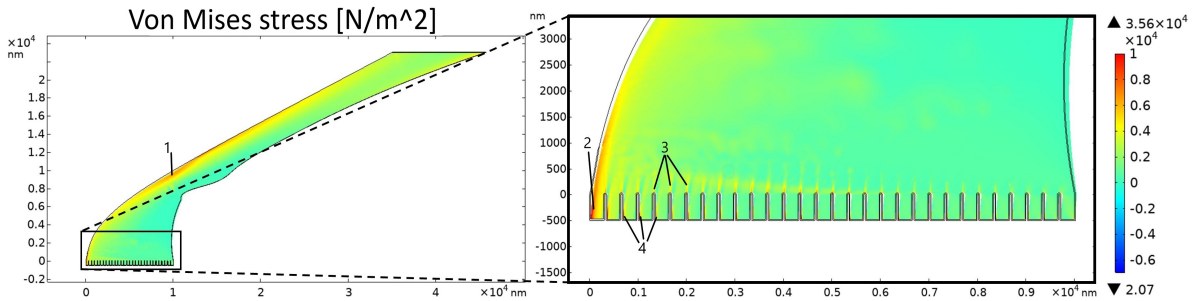

Figure 3.13: The Von Mises stress in the geometry of the epithelial cell for $R_{HGO} = 100$. The right picture shows a close-up of the lower boundary of the cell. The deformation is shown with the solid dark lines which indicate the initial position of the geometry. The magnitude of the deformation is multiplied with a factor 10 to enhance the visualisation. The stress concentrations in the geometry are highlighted with numbers 1 - 4.

Figure 3.13 shows the observed stress concentrations above the spaces between the micro-pillars. These stress concentrations, which are marked with (3) in Figure 3.13, are most likely caused by a combination of the 'bottleneck' effect that acts on the stress distribution and the strain stiffening behaviour of the HGO model. These effects are not expected to be present in the real epithelial cell since the keratinous fibres are split up in bundles which are diverted around the spaces between the micro-pillars.

The S_{11} and S_{22} stress components of the response in the cell body are shown in Figures 3.14a & 3.14b respectively. The stress peak in the left corner of Figure 3.14b for $R_{HGO} = 100$ is caused by the same stress concentration as highlighted with (2) in Figure 3.13. For $R_{HGO} = 10$ and $R_{HGO} = 1$, the magnitude of the S_{22} component of the stress in the left corner of the geometry is considerably lower than for $R_{HGO} = 100$.

In the right half of the geometry, the S_{22} stress component is smaller than zero for $R_{HGO} = 10$ and $R_{HGO} = 100$. The compression in this area of the epithelial cell is not observed for $R_{HGO} = 1$ for which the S_{22} component stays just above zero along the whole length of the cell bottom layer.

The S_{11} stress component shown in Figure 3.14a stays above zero for $R_{HGO} = 1$ while for $R_{HGO} = 10$ and $R_{HGO} = 100$ the value of this component is below zero along the entire length of the epithelial cell bottom apart from an initial stress peak at the left edge of the geometry. A probable cause for the negative values of the S_{11} component as shown in Figure 3.14a is that the tension along the left edge of the geometry causes a compressive force in the region of the epithelial cell which is marked with (2) in Figure 3.15.

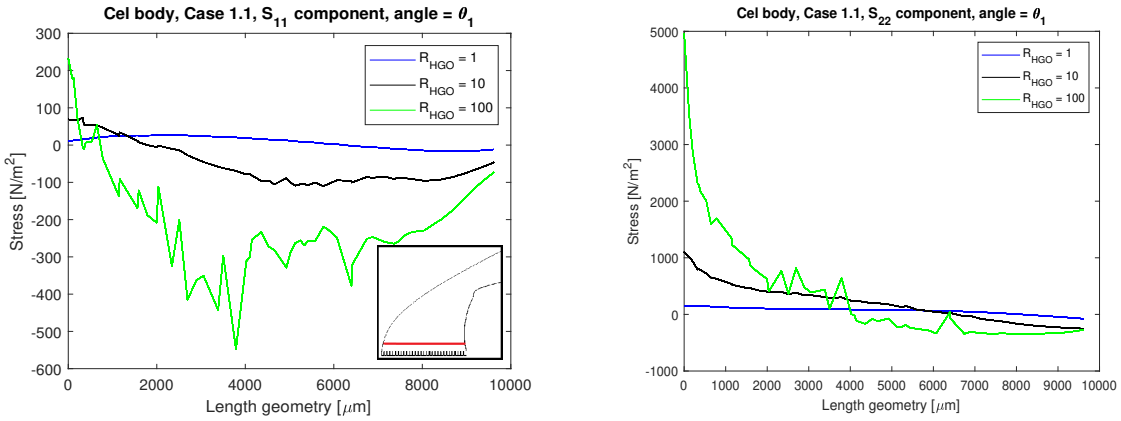

(a) (b)

Figure 3.14: S_{11} and S_{22} stress response components measured in the horizontal line shown in the insert in Figure 3.14a. The load on the epithelial cell is the load from Case 1.1. The non-smooth behaviour shown for $R_{HGO} = 100$ is most probable caused by numerical deviations of the solution.

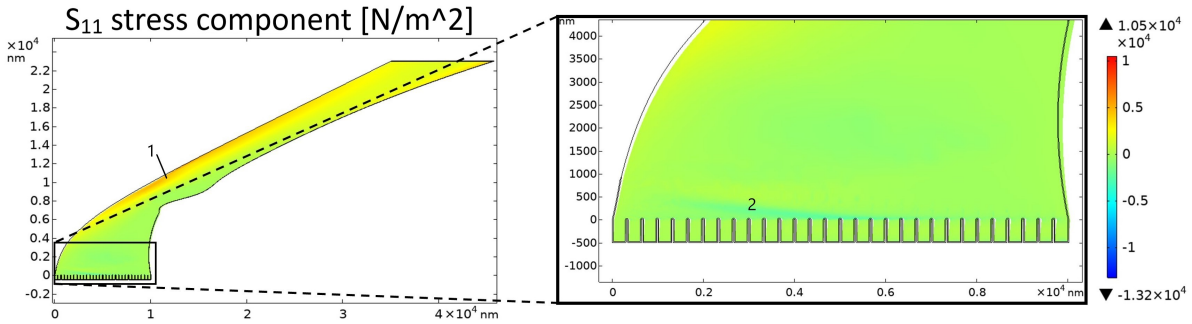

Figure 3.15: The S_{11} stress component in the epithelial cell for $R_{HGO} = 100$. The stress is measured in the red line shown in the geometry of the epithelial cell as shown in the insert in the right bottom corner of Figure 3.14a. The zone in which the largest negative stresses are present is highlighted with (1). The relatively high stresses present in (2) are most probable caused by strain stiffening which follows the direction of the curvilinear coordinates of the HGO model.

3.4.2. Tree frog behaviour: inter-case differences

The loading cases as defined in Section 2.4 each lead to a stress distribution in the epithelial cell shown for θ_3 in Figures 3.16 & 3.17. The main differences between the loading cases are:

1. The highest values for S_{11} are found in the front limb for Case 1.2.
2. The S_{22} stress component is larger for the front limbs (Case 1.2, 2.2, 3.2) when compared to the hind limbs (Case 1.1, 2.1, 3.1). This effect gets stronger when the angle θ is increased.
3. The largest magnitude of S_{22} is observed for θ_3 for Case 1.2 in Figure 3.17b. The magnitude of the S_{22} component for Case 2.2 is only slightly lower than the magnitude found for Case 1.2.
4. The effect of the proximal pulling of the tree frog on the stress response is observed in the difference in the response when comparing the response for Case 1 with the response for Case 2. The difference in the stress response between these cases is relatively small compared to the difference between Case 3 and the other cases.

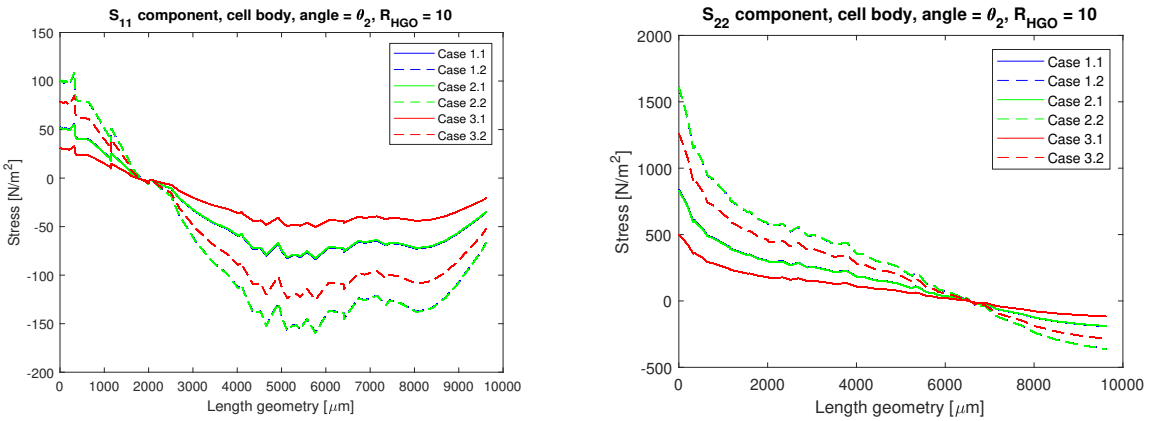

(a) **(b)**

Figure 3.16: The inter-case difference for θ_2 and $R_{HGO} = 10$ shown in (a) and (b) for the S_{11} and S_{22} component respectively. The results from Case 1.1 & Case 1.2 and from Case 1.2 & Case 2.2 are plotted on top of each other and therefore hard to distinguish from each other.

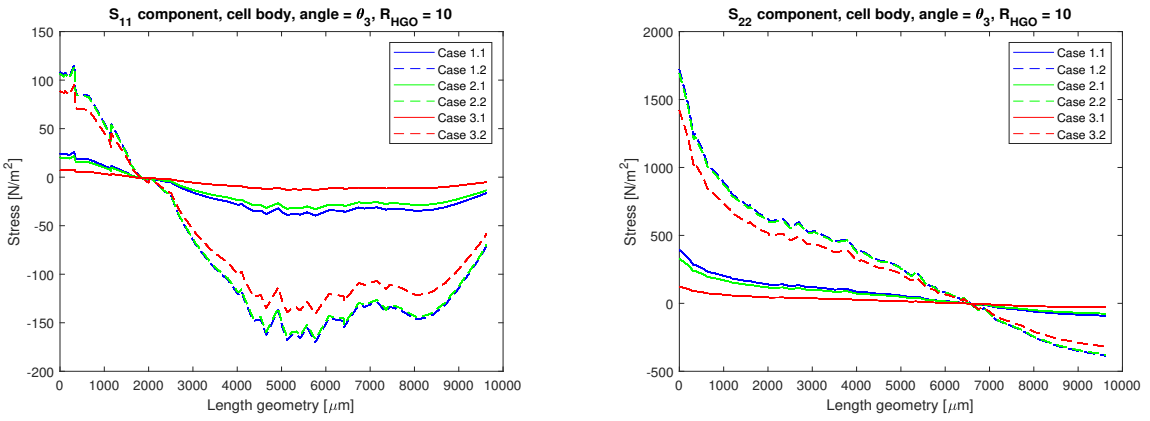

(a) **(b)**

Figure 3.17: The inter-case difference for θ_3 and $R_{HGO} = 10$ shown in (a) and (b) for the S_{11} and S_{22} component respectively. The difference in the results between Case 1.1 & Case 1.2 and Case 1.2 & Case 2.2 is relatively small compared to the difference between Case 3 and the other cases.

4
Experiments: methods

The goal of the experiments was to validate the modeling results on the influence of the fibre-matrix stiffness ratio and the fibre density. Six different samples were fabricated as shown in Table 4.1. The matrix material stiffness values in this table are an approximation of the non-linear hyperelastic material 'stiffness'.

Table 4.1: Properties, coding and process parameters for the fabricated samples. The mixing ratio is expressed in the (elastomer volume: curing agent volume). The indexes shown for the curing duration and temperature are for the first, second, third and fourth process step respectively.

Sample	Sample coding			Process parameters		
Stiffness	Reference, no fibres	Coarse fibres	Thin fibres	Mixing ratio	Curing time [h]	Curing temperature [$^{\circ}C$]
1 [MPa]	R_1MPa	C_1MPa	T_1MPa	1:10	48,48,[-],48	20,20,[-],20
3 [MPa]	R_3MPa	C_3MPa	T_3MPa	1:5	48,48,72,48	20,20,80,20

4.0.1. Fabrication

The fibers implemented in the samples were cut from 1 [mm] thick ABS material (S-Polytec, Germany) with a Lion Merlin laser system (Lion Laser Systems B.V., The Netherlands). The fibers were attached to a base as shown in Figure 4.1a. The assembly of the fibrous part of a single sample is shown in Figure 4.1b. The parts shown in Figure 4.1b were glued together (Bison code 6305952, Bison, Goes, The Netherlands). Further information about the dimensions of the parts used for the fibrous part of the samples can be found in Appendix B.5 - B.8.

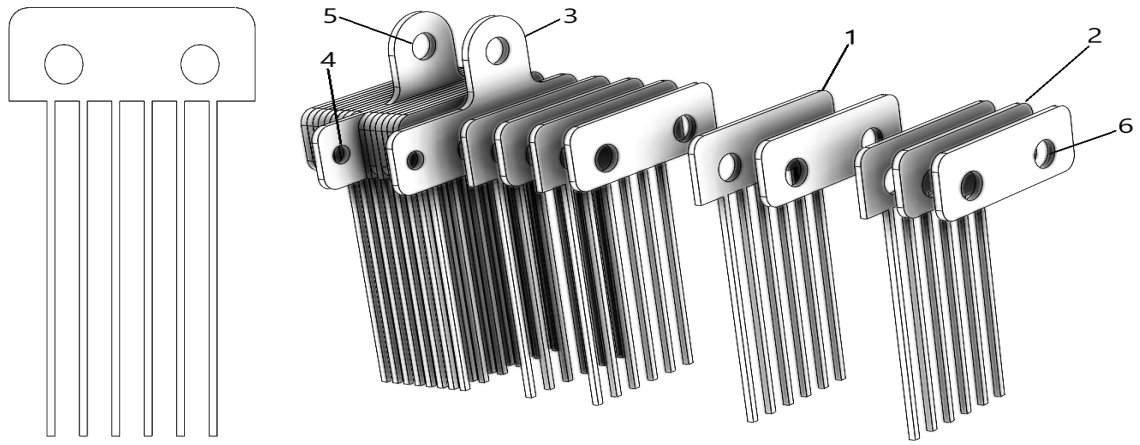

(a) **(b)**

Figure 4.1: Fabrication of the fibrous part of samples *C_1MPa* & *C_3MPa*. Figure 4.1a shows a single fibrous assembly part, marked with (1) in Figure 4.1b. The fibrous assembly parts were spaced with separator plates (2&3). Some of these plates had attachment points (4&5) for force application. All the parts had alignment holes (6) which were used during assembly.

To incorporate the fibers in the base material, a series of moulds was made (Appendix B.1 - B.4). The mould parts were 3D printed using an Ultimaker 2+ (Ultimaker, Geldermalsen, The Netherlands) with Ultimaker PLA filament. The moulds were sanded for a smooth finish. The mixing ratio of the base component and curing agent and the curing duration and temperature are shown in Table 4.1. The mixing ratio's were measured by volume using syringes.

Implementing the fibers in the silicone elastomer base material (SYLGARD® 184, Dow Corning, Midland, USA) involved a series of steps:

1. First, the moulds were partly filled with an uncured layer of PDMS of about 3 [mm] in height. The fibers were inserted into the mould. Just above the PDMS layer, ABS separator plates were inserted to fixate the relatively flexible fibers during the curing process. The bottom of the mould was formed by a perplex plate. The smooth surface of this plate ensured that the bottom of the sample was smooth. The PDMS was thoroughly mixed and poured into the mould. The whole assembly was then cured for 48 [h] at room temperature. To prevent sticking, a thin layer of petroleum jelly was applied to the walls of the mould. To prevent bubbles in the PDMS, the uncured PDMS was degassed in a vacuum chamber until all visible air bubbles were removed. The mould assembly for this step is shown in Figure 4.2a.
2. After finishing the curing of the first step, the partly finished sample was removed from the mould and put in another mould as shown in Figure 4.2b. In this mould, the ABS separator plates were removed from the assembly. After assembly, the mould was filled until the final height of the PDMS section of the sample was reached.
3. This step was only applied for the high stiffness samples and involved a curing cycle in which the samples were cured at 80 [$°C$] for 72 [h]. The samples were removed from the moulds for this curing cycle since the PLA moulds could not resist such temperatures.
4. The purpose of the last step was to smooth the bottom of the samples. The samples were placed on a thin layer of uncured PDMS that was applied on a flat piece of acrylic plastic. Due to gravity and capillary forces, a thin layer of uncured PDMS remained between the samples and the substrate. The samples were again cured for 48 [h] at room temperature. The components involved in this step are shown in Figure 4.2c.

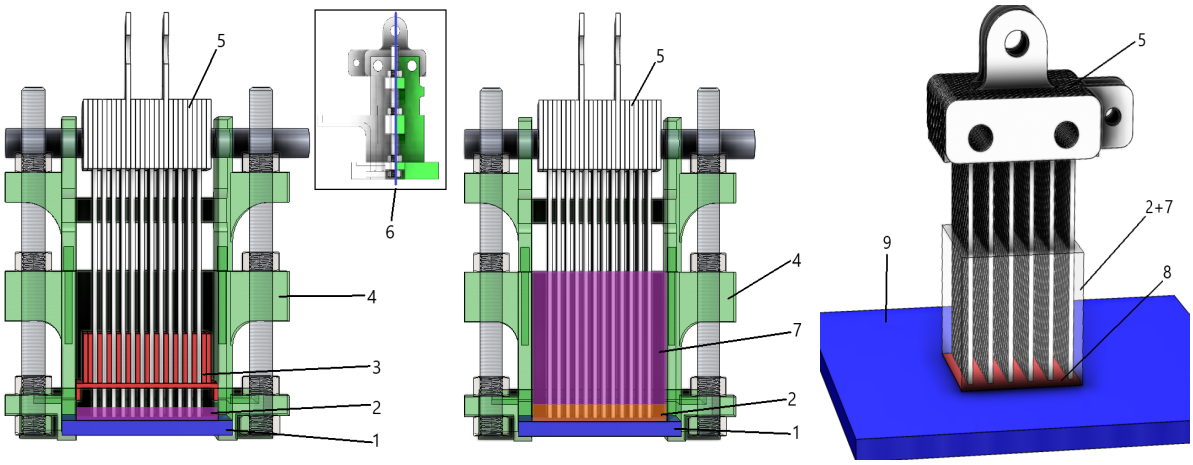

(a) (b) (c)

Figure 4.2: Fabrication of the samples. The mould assembly contained the 3D printed mould parts (Appendix B.4) shown in green (4) and an acrylic plate (1). In the first fabrication step in Figure 4.2a, the first layer of PDMS (2) was poured in the mould. The fibers of sample (5) were kept in place by a series of separator plates (3) which are coloured red in Figure 4.2a. The second fabrication step shown in Figure 4.2b, involved the removal of the separator plates and the insertion of the second layer of PDMS (7). The final step shown in Figure 4.2c involved the addition of a thin layer of PDMS (8) that cured between the bottom of the sample and an acrylic plate (9). The insert in the top right corner of Figure 4.2a shows the cut plane used for the section view of Figures 4.2a & 4.2b.

4.0.2. Experimental setup

The measurement setup shown in Figure 4.3 had two configurations. The configuration shown in Figure 4.3a was used for the adhesion force measurements and the configuration shown in Figure 4.3b was used for the friction force measurements. Further information about the measurement setup components can also be found in Appendix A.

The setup consisted of a rigid frame made from aluminium profiles and was placed on another, wooden frame which accommodated the camera setup. A Thorlabs Z825B (Thorlabs Inc., United States) linear actuator with a translational stage was used for the linear actuation. The actuator was controlled with a KDC101 controller and the Kinesis software. The linear motion of the actuator was transferred to the sample with a nylon wire with a cross-section of 3 [mm]. For shear force application, a pulley was used to guide the nylon wire from the mounting part to the translational stage.

The loads were measured with a load cell (Model FLLSB200, Feteris Components, The Netherlands) and the displacement of the actuation stage was measured with a laser range finder (OptoNCDT 1420, model ILD1420-200, Micro Epsilon, Ortenburg, Germany). The camera setup involved two cameras (Logitech C920, Logitech, The Netherlands) which were placed below and next to the sample as shown in Figure 4.3a. A 6 [mm] thick glass plate was connected to the setup with a set of aluminum clamping parts.

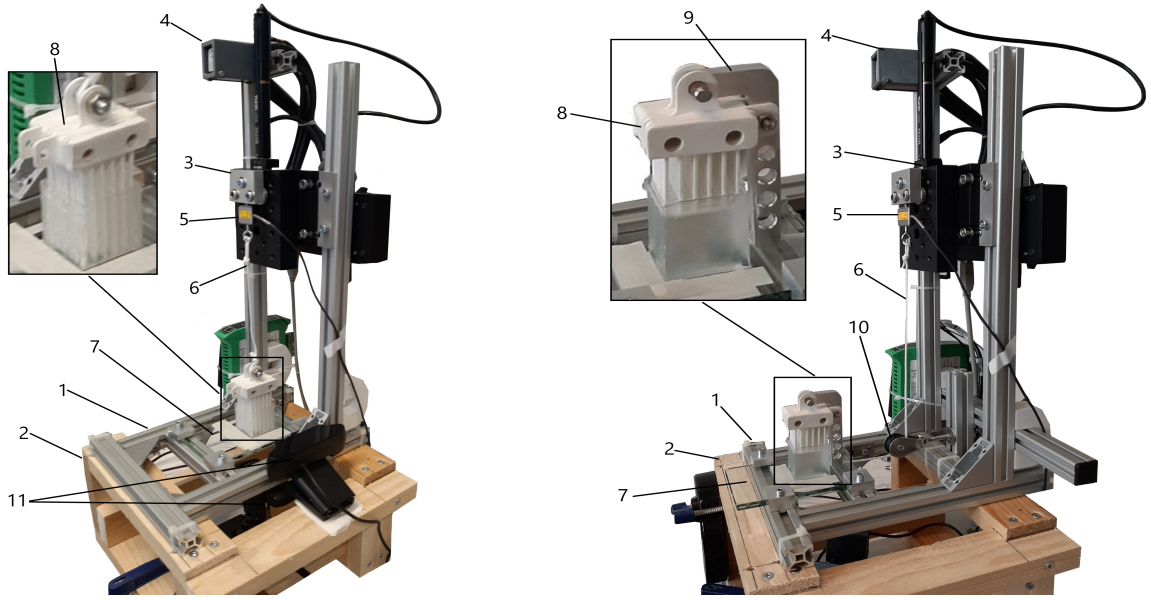

(a) **(b)**

Figure 4.3: Measurement setup for measuring the response of the samples. The setup configuration for measuring the adhesion and s friction forceis shown in (a) and (b) respectively. The frame (1) was made from aluminium extrusion profiles and placed on a wooden base frame (2) which enabled the installation of camera's (11) which were placed below and besides the sample. The substrate consisted of a glass plate (7) which was mounted to the aluminium frame. The forces from the motorized translational actuator (3) were transferred to the sample with a nylon wire (6). A laser distance sensor (4) was used to measure the displacement of the translational stage and a load cell (5) was used to measure the force on the sample. The insert in Figure 4.3a shows the direct attachment of the wire to the top of the sample for normal force measurements. The insert in Figure 4.3b shows the L-shaped mounting part (9) used for the shear force measurements.

4.0.3. Experimental conditions

For adhesion force measurements, the nylon wire was directly connected to the attachment point at the top of the sample. For friction force measurements, The load was transferred to the sample with a relatively stiff aluminum L-shaped mounting part (Appendix A.1). The samples were placed directly on the glass sub-

strate. Preloading was used to ensure the establishment of an initial adhesional bond between the sample and the substrate. All samples detached from the substrate within the range of the linear actuator.

4.0.4. Experimental procedure

The fabrication of the samples was timed such, that the samples for each batch with similar base material stiffness were simultaneously finished and tested. This measure countered variance between similar stiffness samples since the PDMS curing did proceed in time. The samples were tested for both normal and shear loading conditions in randomized order. Each sample was tested 10 times for both loading conditions. The adhesion measurements were performed first and when these were finished, the configuration of the experimental setup was changed and the friction measurements were performed. For the measurements, the following steps were taken:

1. A sample was placed on the substrate and preloaded by placing a 500 [gr] weight on the sample for 10 [s].
2. The sample was loaded and the response was recorded. The maximum acceleration and velocity of the linear translational stage were set to 0.5 [mm/s^2] and 0.5 [mm/s] respectively.
3. After the separation of the sample from the substrate, the sample was cleaned. The bottom of the sample was first rinsed using a paper towel and alcohol. The sample was subsequently rinsed with tap water and left to dry.
4. The glass substrate was cleaned with alcohol when all six samples were tested. Additional cleaning was performed when the substrate was visually polluted.

4.0.5. Data processing

The experimentally obtained data was processed using Matlab 2020b. A one-way Anova analysis with $DoF_1 = 1$ & $DoF_2 = 18$, a reference F-value of $F_{ref} = 4.41$ and a p-value that should be below 0.05 was used to determine the effect of the independent variables.

Some of the elements of the measurement setup, such as the nylon wire and the load cell were relatively compliant compared to the samples and the other elements of the measurement setup. The compliance of these elements influenced the measured force-displacement ratio. The measured data was calibrated to compensate for this deviation in the response. The details of the calibration are described in Appendix D.

5
Experiments: results

The maximal adhesional and frictional forces measured for the samples is shown in Figure 5.1. The statistical interpretation of the differences between the different samples and loading configurations is shown in Table 5.1. In Section 5.3, some observations are described which give additional information on the sample degradation, the sample deformation and the sample detachment.

5.1. Fibre-matrix stiffness ratio

5.1.1. Adhesion force measurements

The differences between samples *R_1MPa* & *R_3MPa*, *C_1MPa* & *C_3MPa* and *T_1MPa* & *T_3MPa* show the influence of the matrix stiffness for samples with a similar fibre configuration. The samples with the 1 MPa matrix stiffness exhibited a significantly higher adhesional forces compared to the samples with the 3 MPa matrix material stiffness.

5.1.2. Friction force measurements

For the shear loading, the force response of the samples is shown in Figure 5.1b. For the 1 MPa matrix stiffness samples, the difference in the measured forces is the lowest between sample *R_1MPa* and *T_1MPa*. The highest friction force is measured for sample *R_1MPa* and the lowest friction force is measured for sample *C_1MPa*.

5.2. Fibre density

5.2.1. Adhesion force measurements

For the normal loading of the samples with the low base stiffness, sample *C_1MPa* exhibited a higher adhesional force than sample *R_1MPa*. Sample *T_1MPa* has the highest adhesional force response in the normal direction among the samples with the 1 MPa matrix stiffness.

For the normal loading of the samples with the 3 MPa matrix stiffness, sample *R_3MPa* exhibited the highest adhesional force. The difference between sample *R_3MPa* & *C_3MPa* is relatively low as can be seen in Table 5.1. Furthermore, it should be noted that the measured forces for sample *C_3MPa* are lower than the forces measured for sample *R_3MPa* and *T_3MPa*.

5.2.2. Friction force measurements

The frictional forces measured for the high base stiffness samples and the low base stiffness samples show a similar pattern: the highest friction forces are measured for both the reference samples. The measured forces for the thin fibre samples are slightly lower compared to the reference samples. The measured forces for the coarse fibre samples are significantly lower compared to the reference samples and the thin fibre samples.

The difference in the measured friction force among the high base stiffness samples (row 4-6 in Table 5.1) is relatively low compared to the difference in force response among the low base stiffness samples (row 1-3 in Table 5.1). This is arguably caused by the outliers in the data for the frictional force measurements for sample *C_3MPa*.

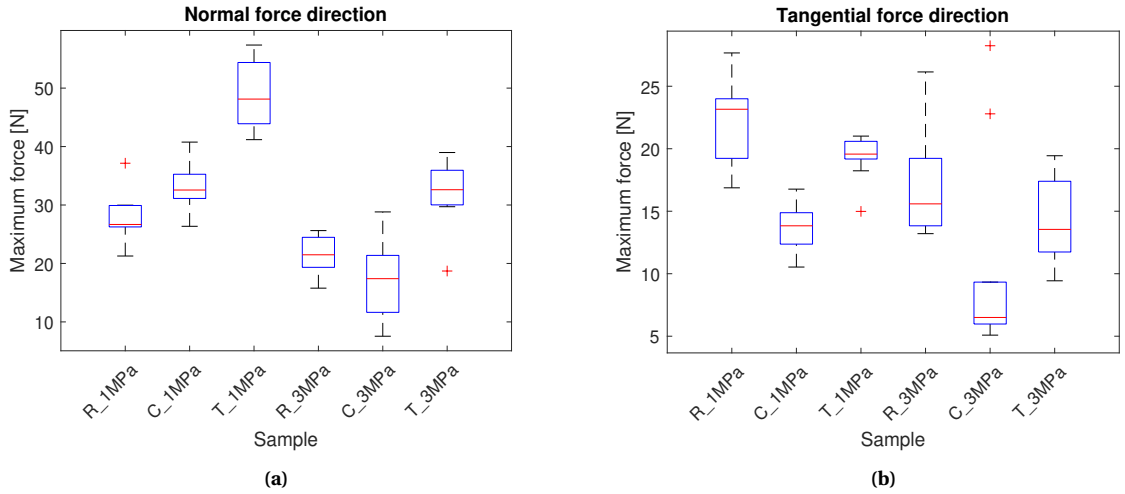

Figure 5.1: Boxplots showing the experimental data obtained on the frictional (Fig. 5.1a) and adhesional (Fig. 5.1b) performance of the different samples.

Table 5.1: Statistical significance of the difference in force response between the different samples. The one-way Anova method is used to determine the parameters p & F.

Samples	Adhesion measurements		Friction measurements	
	p	F	p	F
R_1MPa & T_1MPa	2.0008e-08	89.9742	0.0224	6.2407
R_1MPa & C_1MPa	0.0090	8.5555	1.8139e-06	47.8765
C_1MPa & T_1MPa	7.7069e-07	54.3332	3.4435e-06	43.4297
R_3MPa & T_3MPa	6.5175e-05	26.6680	0.1131	2.7738
R_3MPa & C_3MPa	0.0728	3.6327	0.0321	5.3950
C_3MPa & T_3MPa	2.7426e-05	31.0408	0.1765	1.9792
R_1MPa & R_3MPa	0.0011	14.9473	0.0113	7.9558
C_1MPa & C_3MPa	2.2270e-06	46.4182	0.1989	1.7791
T_1MPa & T_3MPa	2.7338e-06	44.9942	3.9398e-04	18.8410

5.3. Experimental observations

5.3.1. Sample degradation

The samples were directly placed on the glass substrate and were therefore dependent on the smoothness of the lower surface for attachment to the substrate. The smoothness of the lower surface, however, could degrade with the number of testing cycles performed on the samples. As could be visually observed, the cause of the sample degradation was the detachment of the bottom layer which was applied in the fourth fabrication step as described in Section 4.0.1.

Figure 5.2 shows the measured force response for successive testing cycles for samples *R_1MPa*, *C_1MPa* and *T_1MPa* for normal and tangent force loading conditions in Figure 5.2a & 5.2b respectively. As shown in Figure 5.2, the performance of the 1 MPa matrix stiffness samples shows a gradual decline with the number of testing cycles performed.

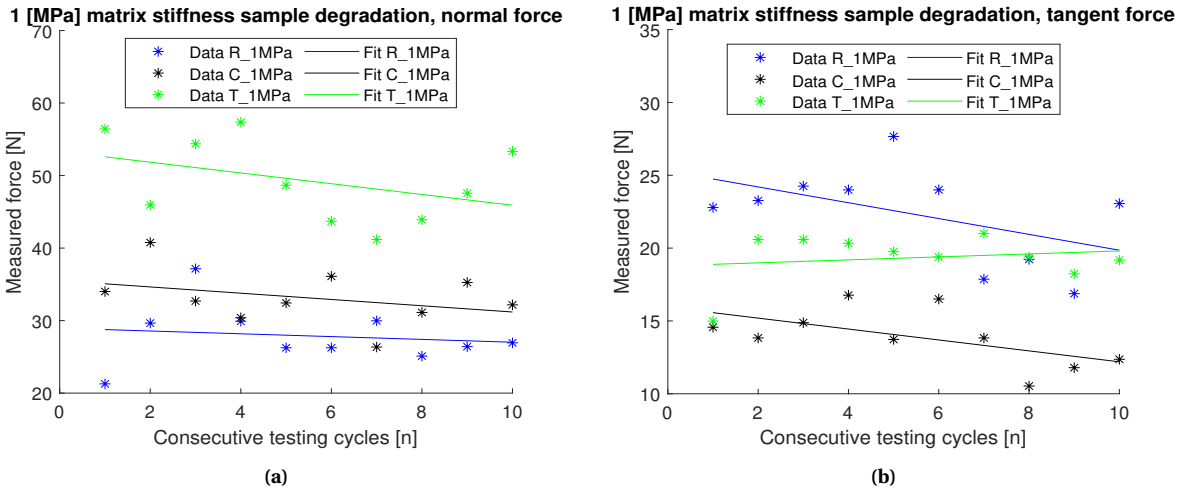

Figure 5.2: The sample degradation of the low stiffness samples. A first degree polynomial fit is used for visualize a trend in the sample performance. The gradual incline of the performance of sample *T_1MPa* for tangent loading conditions is caused by the outlier for n = 1.

The extend of the sample degradation for the 3 MPa matrix stiffness samples is shown in Figure 5.3. The degradation in performance for the 3 MPa matrix stiffness samples is considerably higher than the degradation in performance of the low stiffness samples. The largest degradation in performance is observed for sample *C_3MPa* for normal and shear loading configurations.

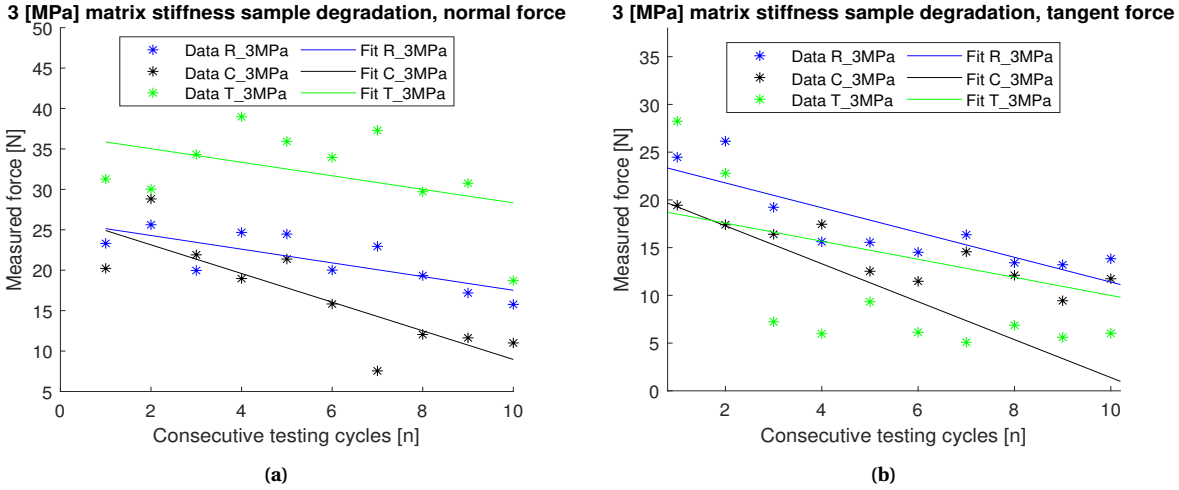

Figure 5.3: The sample degradation of the high stiffness samples. A first degree polynomial fit is used for visualize a trend in the sample performance.

5.3.2. Sample deformation

For the tangential loading conditions, there is a difference between the deformation of the different samples. The deformation of the samples is calculated using the calibration procedure described in Section 4.0.5. The calibrated deformation and stiffness in the horizontal plane of the different samples are shown in Table 5.2.

The stiffness of the reference samples is higher than the stiffness of the fibrous samples and the samples with the coarse embedded fibres have a higher resistance to deformation than the samples with the thin fibres. Samples *T_1MPa* & *T_3MPa* are deformed the most which is caused by the relatively low sample stiff-

ness and the relatively high tangential detachment forces (shown in Figure 5.1b) of the thin fibre samples compared to the reference and coarse fibre samples.

Table 5.2: Calibrated deformation and average stiffness of the samples measured for tangential loading configuration.

Sample	R_1MPa	C_1MPa	T_1MPa	R_3MPa	C_3MPa	T_3MPa
Deformation [mm]	9.642	6.947	12.131	12.040	9.618	15.053
Stiffness [N/m]	1.968	1.270	1.063	1.961	1.545	1.214

5.3.3. Sample detachment

The detachment of sample *T_1MPa* for tangential loading conditions is shown in Figure 5.4. In this figure can be observed that the detachment is initialized at the fibre tips. Therefore, it can be concluded that the fibres play a considerable role in the stress distribution for normal force loading configurations. For tangential loading, the initial detachment also occurs below the fibres for the fibrous samples. Detachment for the reference samples starts at one of the edges of the sample-substrate interface. Further information on the detachment of the different samples for adhesion and friction force measurements can be found in Appendix E.

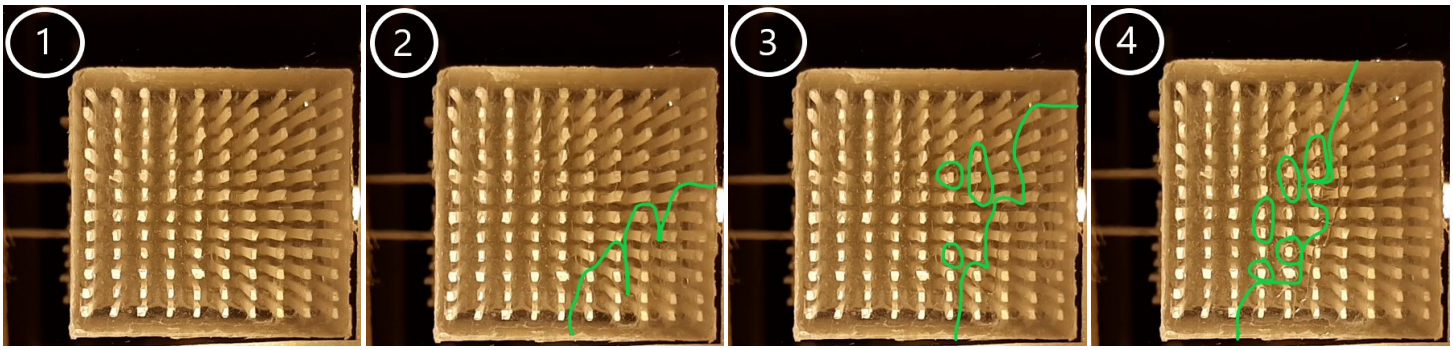

(a) **(b)** **(c)** **(d)**

Figure 5.4: The detachment of sample *T_1MPa* for normal loading condition in steps. The detachment boundaries are visualised with the green lines. Figure 5.4a shows the unloaded sample and Figures 5.4b - 5.4d show the development of the detachment of the sample from the substrate.

6 Discussion

6.1. Modeling assumptions

Models I-III as described in Chapter 2 involve a simplified geometry that does not directly resemble the geometry of the epithelial layer of the tree frog. Model IV, on the other hand, is focused on resembling the properties of an epithelial cell. The assumptions and boundary conditions of this model are discussed in this section.

6.1.1. Material properties

The adhesional and frictional forces required for the tree frog to prevent detachment from a substrate are purely imposed by gravity while the evaluated loading configurations assume a static situation. The stationary models described in this report do not involve materials with viscoelastic properties. These properties are time-dependent and can therefore not be modelled with the models described in this report.

The epithelial layer of the tree frog adhesional pads is well-hydrated and can therefore be expected to have some viscoelastic properties[5, 58]. For a situation in which a static equilibrium is present, these viscoelastic properties do not influence the validity of the modeling results. For more dynamic situations, however, these properties can play a role. The exact extent of this role, however, is not quite clear from the available literature.

The stiffness implemented for the keratinous fibres in the epithelial model is derived from the stiffness measurements found in the literature for the tree frog adhesive pads, as shown in Table 1.1. The stiffness values in this table are not all in the same range and the implemented stiffness is therefore an estimation.

The stiffness implemented for the HGO model is significantly higher than the values used by others who have used the HGO method to model the mechanical properties of other animal tissues [12, 36]. These tissues, however, mainly consist of collagen while the structure of the epithelial cell is mainly composed of keratinous fibres.

The results of the epithelial cell model show that the stress in the corners of the micro-pillars decreases when the stiffness of the cornified cell layer is set to a lower value than the stiffness of the internal structure of the epithelial cell. In literature, the stiffness of the cornified cell layer is argued to be higher than the stiffness of the material directly under this outer cell layer [5, 53] while others describe the opposite [62]. The results described in this report agree with the observations described by Scholz et al.[62].

6.1.2. Boundary conditions

The boundary conditions and applied forces implemented for the epithelial cell model include a constraint on the top boundary of the cell that restricts deformation and rotation while an evenly distributed load acts on this boundary. These boundary conditions are an approximation of reality in which all cell boundaries have some degree of compliance. The material between the upper cell boundary and the lower cell boundary (where the forces are measured), will probably smooth out potential unrealistic effects caused by the boundary conditions on the cell top boundary.

The boundary condition imposed upon the right border of the epithelial cell is dependent on the deformation of the geometry and independent of the material stiffness of the epithelial cell. This leads to a larger role for the force on the boundary for lower values of R_{HGO}, which leads to an increased deformation of the geometry. The increased magnitude of the boundary force compensates the load on the cell and with that, reduces the stress in the other regions of the cell. This partly explains the increased stresses in the epithelial cell for the higher values of R_{HGO}.

The strain stiffening behaviour of the HGO model is one of the causes for the differences between the discrete model and the HGO model. Strain stiffening material behaviour, however, is also encountered in other animal tissues [36, 20, 50] and may therefore be an essential part in approximating the adhesional and frictional performance of the epithelial cell.

6.2. Modeling results

The modeling results are discussed separately for the discrete models (model I & II) and for the HGO models (model III & IV). The results of model IV are compared to the tree frog behaviour. Finally, the differences between the results from the discrete models and the HGO models are discussed.

6.2.1. Discrete fibre model: model I & II

Fibre-matrix stiffness ratio

The results obtained from the discrete fibre models indicate that a high fibre-matrix stiffness ratio is beneficial for a geometry loaded in the direction of the fibres. When loaded perpendicular to the fibre direction, however, the lowest stress response is found for an intermediate value (R_s = 10) of the fibre-matrix stiffness ratio. This fibre-matrix stiffness ratio is not in agreement with the stiffness ratio between the fibres and connective tissue described in Section 1.3.2. The stiffness values of the fibres and connective tissue in the adhesive pads are therefore probably closer to each other than the values derived from the available literature as described in Section 1.3.2.

A probable explanation of the higher performance for an intermediate fibre-matrix stiffness ratio for a shear loaded discrete fibre model is that the stress in the fibres increases with the increase in the fibre-matrix stiffness ratio. For shear loading, the stress has the largest magnitude in the fibres near the edges of the material which results in a stress peak at the fibre tips near the domain edge while the stress at the edges is relatively low compared to this peak [73].

A low fibre-matrix stiffness ratio (R_s = 1) results in stresses at the edges of a shear loaded domain that are significantly higher than the stress peaks found at the domain edges for the intermediate and high (R_s = 100) values of the fibre-matrix stiffness ratio. A realistic loading configuration involves both shear and normal forces. The stress magnitudes recorded for the shear loading configuration, however, are significantly higher than the stress magnitudes found for the normal loading conditions. A fibre reinforced material loaded with a normal and a shear force which are in the same order of magnitude, is therefore argued to have the best frictional and adhesional performance for an intermediate value of the fibre-matrix stiffness ratio.

Fibre-matrix bonding

The results obtained from the discrete models for both normal and shear loading configurations show that an increase in the fibre-matrix bonding increases the fibre-matrix stress transfer and with that, reduces the magnitude of the stress components. This is in agreement with the results obtained by Xue et al. [73].

An increase in the matrix-fibre bonding, however, reduces the compliance of the geometry. The effect of this compliance reduction is not directly visible in the obtained modeling results. The compliance of the epithelial layer is considered an important property for the tree frog adhesive pads, which allows close pad-substrate proximity [45, 58]. An increase in the matrix-fibre bonding may therefore reduce the adhesive pad effectiveness.

6.2.2. HGO model: model III

Fibre-matrix stiffness ratio

For normal loading conditions, the response of the HGO model for the various fibre-matrix stiffness ratio's is similar to the response of the discrete fibre model for the various implemented fibre-matrix stiffness ratio's. For shear loading conditions, the maximum magnitude of the stress response increases with respect to the discrete model with an increase of the fibre-matrix stiffness ratio.

Fibre-matrix bonding

To model the effect of the fibre-matrix bonding with the HGO model, a reduced resistance against shear in the planes parallel to the fibres needs to be implemented. Such shear allowance cannot be implemented by varying the parameters C_m, k_1 or k_2, but requires the exclusion of the shear contributions from the location-dependent stiffness matrix which requires an adaption of the HGO model that changes how W_1 and W_4 from Equation 2.3 are calculated. Such an adaption would fundamentally change the HGO model and therefore falls outside the scope of this report.

6.2.3. HGO model: model IV

Fibre-matrix stiffness ratio

The epithelial cell model shows a highly non-uniform stress distribution at the cell-substrate interface for R_{HGO} = 100. This behaviour can be explained by the strain stiffening properties of the HGO model. The magnitude of the stress peak at the left cell edge is significantly lower for R_{HGO} = 10 which confirms the observation described in Section 3.1.2 that an 'intermediate' fibre-matrix stiffness ratio is an effective way to reduce the magnitude of the stress response at the sample-substrate interface.

Tree frog behaviour vs. modeling results

The proximal pulling on the limbs by the tree frog (the difference between Case 1 and Case 2 described in Section 1.3.3) is expected to reduce the forces needed to keep the contact between the adhesive pads and the substrate intact. An increase of the proximal force changes the forces that are in plane with the substrate while the forces acting perpendicular to the substrate are not affected since $F_{n,1}$ and $F_{n,2}$ are not dependent on the tangential force components.

The modeling results, however, indicate that the difference made by the proximal pulling on the adhesion and frictional forces required for attachment performance is only marginal. This is most noticeable for the hind limbs which are significantly longer and stronger compared to the front limbs. The main purpose of the proximal pulling may therefore not be aimed at the reduction of the required frictional and adhesive forces.

Proximal pulling is also reported as a mechanism used by animals with smooth attachment pads to thin the layer of adhesive fluids between adhesive pads and the substrate [26, 45, 62]. A thinner liquid layer at the substrate-pad interface increases the capillary forces acting between the adhesive pad and the substrate[46, 59, 74]. Proximal pulling can also bring the pad close enough to the substrate to generate dry contact interaction through Van der Waals forces [38, 22].

The absence of a significant difference between the front and hind limbs is in agreement with the absence of any observed differences in morphology between the front and hind limbs of the tree frog in the available literature. Furthermore, there is no reported difference between the mucus properties for the front and hind limbs.

The required forces at the interface between adhesive pads and substrate to maintain adhesional performance as shown in Figure 1.4 indicate that the limb spreading and positional adjustment of the tree frog can reduce the required adhesion forces while increasing the involved friction forces. These friction forces can

'load' the dermal structure of the adhesive pads and with that, increase the contact area between the pads and the substrate [53, 28]. In this way, the tree frog can simultaneously reduce the required adhesive forces and increase the adhesive and frictional properties of the adhesive pads.

The positional adjustment of the tree frog also reduces the contact angle between the adhesive pads and the substrate. A reduction of the contact angle can further increase the adhesional performance [59]. The effect of contact angle reduction is larger when the positional adjustment causes the contact angle to be reduced to a value that is smaller than the critical contact angle. The critical contact angle is around 30 degrees for flat contact surfaces[65, 55].

6.2.4. Discrete fibre model vs. HGO model

The difference in the stress response for the different values of R_{HGO} is relatively small when compared to the difference in the stress response found for a variation of R_s for the discrete fibre model. A probable cause for this is that the strain stiffening properties of the HGO model increase the stiffness in the direction of the fibres for low values of R_{HGO} which indirectly stiffens the material in the fibre direction.

Another difference between the discrete model and the HGO model is that the stress response on the level of individual fibres cannot be implemented with the HGO model. This leads to a difference in the measured stresses between both material models at the edges of the domain for non-uniform loading configurations. The decreased magnitude of the stress at the edge of the domain for the discrete fibre model is probably caused by the lower stresses in the relatively compliant matrix material between the edge of the material domain and the last fibre. The properties of the HGO model are continuous through the domain. The stress peak at the edge of the domain is for this is model probably caused by a combination of non-uniform loading conditions and the strain stiffening properties.

The HGO material model implemented in models III & IV does not incorporate discrete fibres and the results of these models are therefore not considered representative for the stresses at the level of the discrete fibres in the micro-pillars. The stresses at the discrete fibre level are more accurately represented by the fibre pattern implemented in the geometry of model I. Model I is therefore considered representative for the stress components in the micro-pillars. The results of model IV are used to evaluate the influence of the proximal pulling and positional adjustments of the tree frog.

6.3. Experimental results

The variables that are varied between the different samples are the fibre-matrix stiffness ratio and the fibre density. The experimental results on the effect of these two variables on the adhesional and frictional performance are compared with the modeling results in this section.

6.3.1. Fibre-matrix stiffness ratio

Adhesion force measurements

Based on the modeling results it was expected that the 1 MPa matrix stiffness samples would outperform the 3 MPa matrix stiffness samples which have a lower fibre-matrix stiffness ratio. The difference in performance was not expected to be very significant since the difference in stiffness ratio between these two groups is relatively low compared to the different fibre-matrix stiffness ratio's implemented in the models.

The experimental results show higher adhesional forces for the samples with relatively low matrix material stiffness compared to the samples with the relatively high matrix material stiffness. This is accordance with the expectations, but the observed difference in adhesional performance is much larger than expected from the modeling results.

A probable cause for this deviation is a difference in the stickiness of the bottom of the samples. The bottom of the 1 MPa matrix stiffness samples was observed to be more sticky than the bottom of the other

samples. The difference in bottom stickiness directly influences the adhesion performance since no further adhesive is used to improve the attachment of the samples to the substrate. An increased adhesive performance for a very soft PDMS structure compared to a stiffer PDMS structure is also described by Li et al. [48].

Friction force measurements

The difference between the modelled and experimental results for the influence of the fibre-matrix stiffness ratio as described for the adhesional measurements in the previous section is also applicable for the frictional force measurements.

6.3.2. Fibre density

Adhesion force measurements

It was expected that samples *T_1MPa* & *T_3MPa* would outperform samples *C_1MPa* & *C_3MPa* due to the better stress distribution for the relatively thin fibre pattern. Based on the modeling results, the difference between the thin and coarse fibre pattern is expected to be less for friction force measurements than for adhesion force measurements. For the adhesive force measurements, the samples with the relatively thin fibres show higher adhesional forces than the reference samples and the samples with the coarse fibre pattern which confirms the expectations.

The measured adhesional force for normal force loading conditions for sample *C_3MPa* is lower than expected from the modeling results which predicted the adhesional performance of this sample to be in between the performance of samples *R_3MPa* & *T_3MPa*. A probable cause for the lower adhesional performance of sample *C_3MPa* is the relatively large bottom surface degradation of this sample as is also shown in Figure 5.3. Degradation of the attachment performance is also observed for the other samples and plays a larger role for the samples with the 3 MPa matrix material stiffness compared to the samples with the 1 MPa matrix material stiffness. Degradation of PDMS adhesives is also described by others [15, 37].

Friction force measurements

The results on the frictional performance show that both reference samples exhibit higher frictional forces than the fibrous samples. These results are not in agreement with the modeling results, which predicted the reference samples to exhibit lower frictional forces than the fibrous samples.

A possible explanation for this deviation can be found in Table 5.2. In this table it is shown that the reference samples exhibit a higher resistance to deformation compared to the fibrous samples. This higher resistance to deformation under tangential load reduces the peeling effect which develops when the samples are tangentially loaded. The peeling effect is thus considerably stronger for the fibrous samples than for the reference samples.

A second possible cause for this deviation between the expected and obtained results is that the model (model II) used to predict the experimental results can not be used to produce an estimation of the stress for large deformations. The reason for this is the limited convergence of the model which severely restricted the magnitude of the deformation that could be implemented. Large deformations can considerably affect the stress response of the hyperelastic materials involved which are described to exhibit non-linear strain-dependent properties [52].

6.4. Recommendations & future work

6.4.1. Modeling

The material properties implemented in the different models used to obtain the modeling results are derived from studies that describe the mechanical properties of several animal tissues. These properties are considered representative for the mechanical properties of the tree frog epithelial layer. The true mechanical

properties of the different materials present in the epithelial, however, are not known and additional research is needed to determine these properties.

The modeling results are influenced by the boundary conditions. Model IV is an approximation of an actual epithelial cell and the boundary conditions of an actual epithelial cell are dependent on the mechanical properties of the other elements in the dermal structure of the terminal digit of the tree frog. The mechanical properties of these other elements are largely unknown and need further research.

One of the assumptions incorporated in the used models is that the sample-substrate attachment is static until sample detachment occurs. Some studies, however, do suggest that static attachment for animals using wet adhesion can also be dynamic[24]. Dynamic attachment is often related to the viscoelastic properties of the mucus layer between the pad and the substrate[24, 38]. The influence of mucus properties and dynamic attachment is not included in this report.

6.4.2. Experiments

The observed sample degradation relates to the fabrication method of the samples which includes several steps in which the sample is constructed from different layers of PDMS. The curing of PDMS is time-dependent which leads to differences between the mechanical properties of the different layers in the sample. A production process that involves fewer layers of PDMS would speed up sample production, increase the uniformity of the mechanical properties in the matrix material and would reduce sample degradation. A faster production process would also facilitate an increase in the sample size. A larger sample size would make re-use of samples unnecessary and with that, reduce the influence of sample degradation.

The larger deformation for the fibrous samples compared to the reference samples is a probable reason for the deviation between modeling and experimental results for tangential loading configurations. To further validate the modeling results, The reference samples should be adapted such that the resistance to deformation of these samples is in the same range as observed for the fibrous samples.

7
Conclusion

This report discusses the mechanics of an epithelial cell in a tree frog adhesive pad. The modeling steps taken provide insight into the mechanical behaviour of the fibrous domain and the micro-pillars of the epithelial cell. The analysis of the mechanical behaviour focuses on the stress distribution at the interface of the epithelial layer and a smooth substrate. The goal of this report is to answer the research question: *'Do the tilted embedded keratin fibres in the epithelial cells and nanopillars prevent the development of stress concentrations on the adhesive pads of the tree frog?'*

Using a simplified modeling approach, it is found that fibre-matrix bonding is essential for the stress distribution in a material. The fibre-matrix bonding should furthermore be equal at the entire interface between fibres and matrix material.

The modeling results indicate that for a fibre reinforced composite with a coarse fibre pattern, the largest stress concentrations at the interface between the sample and the substrate can be found at the locations of the fibre tips. However, for an increasing fibre density (more and thinner fibres), the stress components present at the interface with the substrate smooth out over the length of the interface.

The magnitude of the stress components in a composite material is found to be dependent on the fibre-matrix stiffness ratio. For loading configurations in which the load has a uniform distribution over the domain and acts in the direction of the fibres, an increase in the fibre-matrix stiffness ratio decreases the magnitude of the stress response. For non-uniform loads and loads perpendicular to the fibre direction, a more intermediate fibre-matrix stiffness is found to yield the lowest stresses at the sample-substrate interface.

The effect of the fibre-matrix stiffness ratio is also visible in the epithelial cell model. The stress distribution in the epithelial cell is calculated for the loads associated with the stages in limb spreading of the tree frog. The results of the epithelial cell model show that proximal pulling on the limbs by the tree frog has no significant effect on the stress magnitude at the pad-substrate interface. The positional adjustment of the frog, however, is argued to significantly reduce the magnitude of the maximum stress values at the pad-substrate interface. Furthermore, the behaviour of the frog is argued to reduce the required normal forces while simultaneously increasing the adhesive properties of the adhesive pads.

Bibliography

[1] BB Aaron and JM Gosline. “Elastin as a random-network elastomer: A mechanical and optical analysis of single elastin fibers”. In: *Biopolymers: Original Research on Biomolecules* 20.6 (1981), pp. 1247–1260.

[2] Alan T Asbeck et al. “Climbing walls with microspines”. In: *IEEE ICRA*. Fla. 2006, pp. 4315–4317.

[3] Elina Auzina. “Exploring the possibility and need of making a spider inspired footpad for robotic legs using a 3D printer for use in a low energy system”. In: *2015 IEEE 3rd Workshop on Advances in Information, Electronic and Electrical Engineering (AIEEE)*. IEEE. 2015, pp. 1–5.

[4] W Jon P Barnes et al. “Comparative Cryo-SEM and AFM studies of hylid and rhacophorid tree frog toe pads”. In: *Journal of morphology* 274.12 (2013), pp. 1384–1396.

[5] W Jon P Barnes et al. “Elastic modulus of tree frog adhesive toe pads”. In: *Journal of Comparative Physiology A* 197.10 (2011), p. 969.

[6] WJP Barnes, P Perez-Goodwyn, and SN Gorb. “Mechanical properties of the toe pads of the tree frog, Litoria caerulea”. In: *Comparative Biochemistry and Physiology. Part A: Molecular and Integrative Physiology* 141.3 Supp (2005), S145–S145.

[7] JE Bertram and JM Gosline. “Functional design of horse hoof keratin: the modulation of mechanical properties through hydration effects”. In: *Journal of Experimental Biology* 130.1 (1987), pp. 121–136.

[8] RH C BONSER. “The Young’s modulus of ostrich claw keratin”. In: *Journal of Materials Science Letters* 19.12 (2000), pp. 1039–1040.

[9] GJ Cameron, Tim J Wess, and RHC Bonser. “Young’s modulus varies with differential orientation of keratin in feathers”. In: *Journal of structural biology* 143.2 (2003), pp. 118–123.

[10] Rui Chen. “A gecko-inspired electroadhesive wall-climbing robot”. In: *IEEE Potentials* 34.2 (2015), pp. 15–19.

[11] Rui Chen et al. “A gecko-inspired wall-climbing robot based on vibration suction mechanism”. In: *Proceedings of the Institution of Mechanical Engineers, Part C: Journal of Mechanical Engineering Science* 233.19-20 (2019), pp. 7132–7143.

[12] MJ Collins et al. “Mechanical properties of suprarenal and infrarenal abdominal aorta: implications for mouse models of aneurysms”. In: *Medical engineering & physics* 33.10 (2011), pp. 1262–1269.

[13] Niall Crawford, Thomas Endlein, and W Jon P Barnes. “Self-cleaning in tree frog toe pads; a mechanism for recovering from contamination without the need for grooming”. In: *Journal of Experimental Biology* 215.22 (2012), pp. 3965–3972.

[14] Dirk M Drotlef et al. “Morphological studies of the toe pads of the rock frog, Staurois parvus (family: Ranidae) and their relevance to the development of new biomimetically inspired reversible adhesives”. In: *Interface focus* 5.1 (2015), p. 20140036.

[15] Dirk-Michael Drotlef et al. “Insights into the adhesive mechanisms of tree frogs using artificial mimics”. In: *Advanced Functional Materials* 23.9 (2013), pp. 1137–1146.

[16] William E Duellman and Linda Trueb. *Biology of amphibians*. JHU press, 1994.

[17] Pavel Dutov et al. “Measurement of elastic modulus of collagen type I single fiber”. In: *PloS one* 11.1 (2016), e0145711.

[18] Thomas Endlein et al. “Sticking like sticky tape: tree frogs use friction forces to enhance attachment on overhanging surfaces”. In: *Journal of The Royal Society Interface* 10.80 (2013), p. 20120838.

[19] Thomas Endlein et al. “The use of clamping grips and friction pads by tree frogs for climbing curved surfaces”. In: *Proceedings of the Royal Society B: Biological Sciences* 284.1849 (2017), p. 20162867.

[20] Kendra A Erk, Kevin J Henderson, and Kenneth R Shull. “Strain stiffening in synthetic and biopolymer networks”. In: *Biomacromolecules* 11.5 (2010), pp. 1358–1363.

[21] Valerie V Ernst. “The digital pads of the tree frog, Hyla cinerea. I. The epidermis”. In: *Tissue and Cell* 5.1 (1973), pp. 83–96.

[22] Walter Federle, Werner Baumgartner, and Bert Hölldobler. “Biomechanics of ant adhesive pads: frictional forces are rate-and temperature-dependent”. In: *Journal of Experimental Biology* 207.1 (2004), pp. 67–74.

[23] W Federle et al. “Wet but not slippery: boundary friction in tree frog adhesive toe pads”. In: *Journal of the Royal Society Interface* 3.10 (2006), pp. 689–697.

[24] Leonid Frantsevich et al. “Adhesive properties of the arolium of a lantern-fly, Lycorma delicatula (Auchenorrhyncha, Fulgoridae)”. In: *Journal of insect physiology* 54.5 (2008), pp. 818–827.

[25] Maren Freutel et al. “Finite element modeling of soft tissues: material models, tissue interaction and challenges”. In: *Clinical Biomechanics* 29.4 (2014), pp. 363–372.

[26] Ling Gong et al. “Observation of micro-topography of newt toe pads and investigating on wet adhesive properties of microstructured surface of PDMS”. In: *Bioinspiration, Biomimetics, and Bioreplication VIII*. Vol. 10593. International Society for Optics and Photonics. 2018, p. 105930M.

[27] Ling Gong et al. “Wet-adhesion properties of microstructured surfaces inspired by newt footpads”. In: *Smart Materials and Structures* 27.11 (2018), p. 114001.

[28] Pablo Perez Goodwyn et al. “Material structure, stiffness, and adhesion: why attachment pads of the grasshopper (Tettigonia viridissima) adhere more strongly than those of the locust (Locusta migratoria)(Insecta: Orthoptera)”. In: *Journal of comparative physiology A* 192.11 (2006), pp. 1233–1243.

[29] Stanislav N Gorb et al. “Insects did it first: a micropatterned adhesive tape for robotic applications”. In: *Bioinspiration & biomimetics* 2.4 (2007), S117.

[30] John Gosline et al. “Elastic proteins: biological roles and mechanical properties”. In: *Philosophical Transactions of the Royal Society of London. Series B: Biological Sciences* 357.1418 (2002), pp. 121–132.

[31] Colin A Grant et al. “Tuning the elastic modulus of hydrated collagen fibrils”. In: *Biophysical journal* 97.11 (2009), pp. 2985–2992.

[32] Matthias Greuter et al. “Toward micro wall-climbing robots using biomimetic fibrillar adhesives”. In: *Proceedings of the 3rd International Symposium on Autonomous Minirobots for Research and Edutainment (AMiRE 2005)*. Springer. 2006, pp. 39–46.

[33] GAVIN HANNA, W Jon, and WP JON BARNES. “Adhesion and detachment of the toe pads of tree frogs”. In: *Journal of Experimental Biology* 155.1 (1991), pp. 103–125.

[34] R Harley et al. “Phonons and the elastic moduli of collagen and muscle”. In: *Nature* 267.5608 (1977), pp. 285–287.

[35] Elliot W Hawkes, Hao Jiang, and Mark R Cutkosky. “Three-dimensional dynamic surface grasping with dry adhesion”. In: *The International Journal of Robotics Research* 35.8 (2016), pp. 943–958.

[36] Gerhard A Holzapfel, Thomas C Gasser, and Ray W Ogden. “A new constitutive framework for arterial wall mechanics and a comparative study of material models”. In: *Journal of elasticity and the physical science of solids* 61.1-3 (2000), pp. 1–48.

[37] Jagoba Iturri et al. “Torrent frog-inspired adhesives: attachment to flooded surfaces”. In: *Advanced Functional Materials* 25.10 (2015), pp. 1499–1505.

[38] Michael Kappl, Farzaneh Kaveh, and W Jon P Barnes. “Nanoscale friction and adhesion of tree frog toe pads”. In: *Bioinspiration & biomimetics* 11.3 (2016), p. 035003.

[39] Sangbae Kim et al. “Smooth vertical surface climbing with directional adhesion”. In: *IEEE Transactions on robotics* 24.1 (2008), pp. 65–74.

[40] Tae Kyung Kim, Jeong Koo Kim, and Ok Chan Jeong. “Measurement of nonlinear mechanical properties of PDMS elastomer”. In: *Microelectronic Engineering* 88.8 (2011), pp. 1982–1985.

[41] Moon Kyu Kwak et al. “Towards the next level of bioinspired dry adhesives: new designs and applications”. In: *Advanced Functional Materials* 21.19 (2011), pp. 3606–3616.

[42] David Labonte and Walter Federle. “Biomechanics of shear-sensitive adhesion in climbing animals: peeling, pre-tension and sliding-induced changes in interface strength”. In: *Journal of The Royal Society Interface* 13.122 (2016), p. 20160373.

[43] Julian KA Langowski et al. “Comparative and functional analysis of the digital mucus glands and secretions of tree frogs”. In: *Frontiers in zoology* 16.1 (2019), pp. 1–17.

[44] Julian KA Langowski et al. “Force-transmitting structures in the digital pads of the tree frog Hyla cinerea: a functional interpretation”. In: *Journal of anatomy* 233.4 (2018), pp. 478–495.

[45] Julian KA Langowski et al. “Tree frog attachment: mechanisms, challenges, and perspectives”. In: *Frontiers in zoology* 15.1 (2018), pp. 1–21.

[46] Pierre Simon Laplace. *Traité de mécanique céleste*. Vol. 1. de l’Imprimerie de Crapelet, 1799.

[47] LePing Li, JTM Cheung, and W Herzog. “Three-dimensional fibril-reinforced finite element model of articular cartilage”. In: *Medical & biological engineering & computing* 47.6 (2009), p. 607.

[48] Meng Li et al. “Effect of wetting case and softness on adhesion of bioinspired micropatterned surfaces”. In: *Journal of the mechanical behavior of biomedical materials* 78 (2018), pp. 266–272.

[49] MingHe Li et al. “A wet adhesion inspired biomimetic pad with direction dependence and adaptability”. In: *Chinese Science Bulletin* 56.18 (2011), pp. 1935–1941.

[50] Mo Li et al. “Comparative research on morphology and mechanical property of integument of Rana dybowskii, Xenopus laevis and Ambystoma mexicanum”. In: *Journal of the Mechanical Behavior of Biomedical Materials* (2021), p. 104382.

[51] Valentin Lulevich et al. “Single cell mechanics of keratinocyte cells”. In: *Ultramicroscopy* 110.12 (2010), pp. 1435–1442.

[52] Melvin Mooney. “A theory of large elastic deformation”. In: *Journal of applied physics* 11.9 (1940), pp. 582–592.

[53] Masato Nakano and Tomoyuki Saino. “Light and electron microscopic analyses of the high deformability of adhesive toe pads in White’s tree frog, Litoria caerulea”. In: *Journal of morphology* 277.11 (2016), pp. 1509–1516.

[54] Raymond W Ogden. *Non-linear elastic deformations*. Courier Corporation, 1997.

[55] MJ Orchard, Mika Kohonen, and Stuart Humphries. “The influence of surface energy on the self-cleaning of insect adhesive devices”. In: *Journal of Experimental Biology* 215.2 (2012), pp. 279–286.

[56] Anne M Peattie et al. “Ancestrally high elastic modulus of gecko setal β-keratin”. In: *Journal of The Royal Society Interface* 4.17 (2007), pp. 1071–1076.

[57] Zhilong Peng, Cong Wang, and Shaohua Chen. “The microstructure morphology on ant footpads and its effect on ant adhesion”. In: *Acta Mechanica* 227.7 (2016), pp. 2025–2037.

[58] BNJ Persson. “Wet adhesion with application to tree frog adhesive toe pads and tires”. In: *Journal of Physics: Condensed Matter* 19.37 (2007), p. 376110.

[59] Jin Qian and Huajian Gao. “Scaling effects of wet adhesion in biological attachment systems”. In: *Acta biomaterialia* 2.1 (2006), pp. 51–58.

[60] Carl Runge. “Über empirische Funktionen und die Interpolation zwischen äquidistanten Ordinaten”. In: *Zeitschrift für Mathematik und Physik* 46.224-243 (1901), p. 20.

[61] Dan Sameoto, Yasong Li, and Carlo Menon. “Multi-scale compliant foot designs and fabrication for use with a spider-inspired climbing robot”. In: *Journal of Bionic Engineering* 5.3 (2008), pp. 189–196.

[62] Ingo Scholz et al. “Ultrastructure and physical properties of an adhesive surface, the toe pad epithelium of the tree frog, Litoria caerulea White”. In: *Journal of Experimental Biology* 212.2 (2009), pp. 155–162.

[63] WS Simpson. “51—A COMPARISON OF METHODS OF MEASUREMENT OF YOUNG’S MODULUS FOR KERATIN FIBRES”. In: *Journal of the Textile Institute Transactions* 56.12 (1965), T675–T683.

[64] Matthew J Spenko et al. “Biologically inspired climbing with a hexapedal robot”. In: *Journal of field robotics* 25.4-5 (2008), pp. 223–242.

[65] Yewang Su et al. “Concave biological surfaces for strong wet adhesion”. In: *Acta Mechanica Solida Sinica* 22.6 (2009), pp. 593–604.

[66] Yilin Su et al. “A study of the microstructure modification of a space crawling robot adhesive feet based on discrete element method”. In: *Journal of the Brazilian Society of Mechanical Sciences and Engineering* 41.11 (2019), p. 533.

[67] Kenji Suzuki et al. “Insect-inspired wall-climbing robots utilizing surface tension forces”. In: *Journal of Advanced Mechanical Design, Systems, and Manufacturing* 4.1 (2010), pp. 383–390.

[68] Ozgur Unver and Metin Sitti. “Flat dry elastomer adhesives as attachment materials for climbing robots”. In: *IEEE transactions on robotics* 26.1 (2009), pp. 131–141.

[69] Ozgur Unver et al. “Geckobot: A gecko inspired climbing robot using elastomer adhesives”. In: *Proceedings 2006 IEEE International Conference on Robotics and Automation, 2006. ICRA 2006.* IEEE. 2006, pp. 2329–2335.

[70] Pho Van Nguyen, Ngoc Van Huynh, Tue Trong Phan, et al. “Soft grasping with wet adhesion: Preliminary evaluation”. In: *2018 IEEE International Conference on Soft Robotics (RoboSoft).* IEEE. 2018, pp. 418–423.

[71] Zhongyuan Wang, Gongxun Sun, and Zhendong Dai. “Trajectory optimization for robot crawling on ceiling using dry elastomer adhesive”. In: *Advances in Reconfigurable Mechanisms and Robots II.* Springer, 2016, pp. 593–601.

[72] Marco PE Wenger et al. “Mechanical properties of collagen fibrils”. In: *Biophysical journal* 93.4 (2007), pp. 1255–1263.

[73] Longjian Xue et al. “Hybrid surface patterns mimicking the design of the adhesive toe pad of tree frog”. In: *ACS nano* 11.10 (2017), pp. 9711–9719.

[74] Xiong Yi et al. “Dynamic Contact Model of Bio-Adhesive Pads of Animals: Simulation Experiments”. In: *Advanced Tribology.* Springer, 2009, pp. 867–868.

[75] Zhiwei Yu et al. “Design and analysis of a bionic adhesive foot for gecko robot climbing the ceiling”. In: *International Journal of Robotics and Automation* 33.4 (2018).

A
Measurement setup

This appendix includes the files that provide additional information about the measurement setup. Section A.1 contains the L-shaped mounting part used for the friction force measurements. Section A.2 provides information about the load cell used in the measurement setup.

A.1. L-shaped mounting part

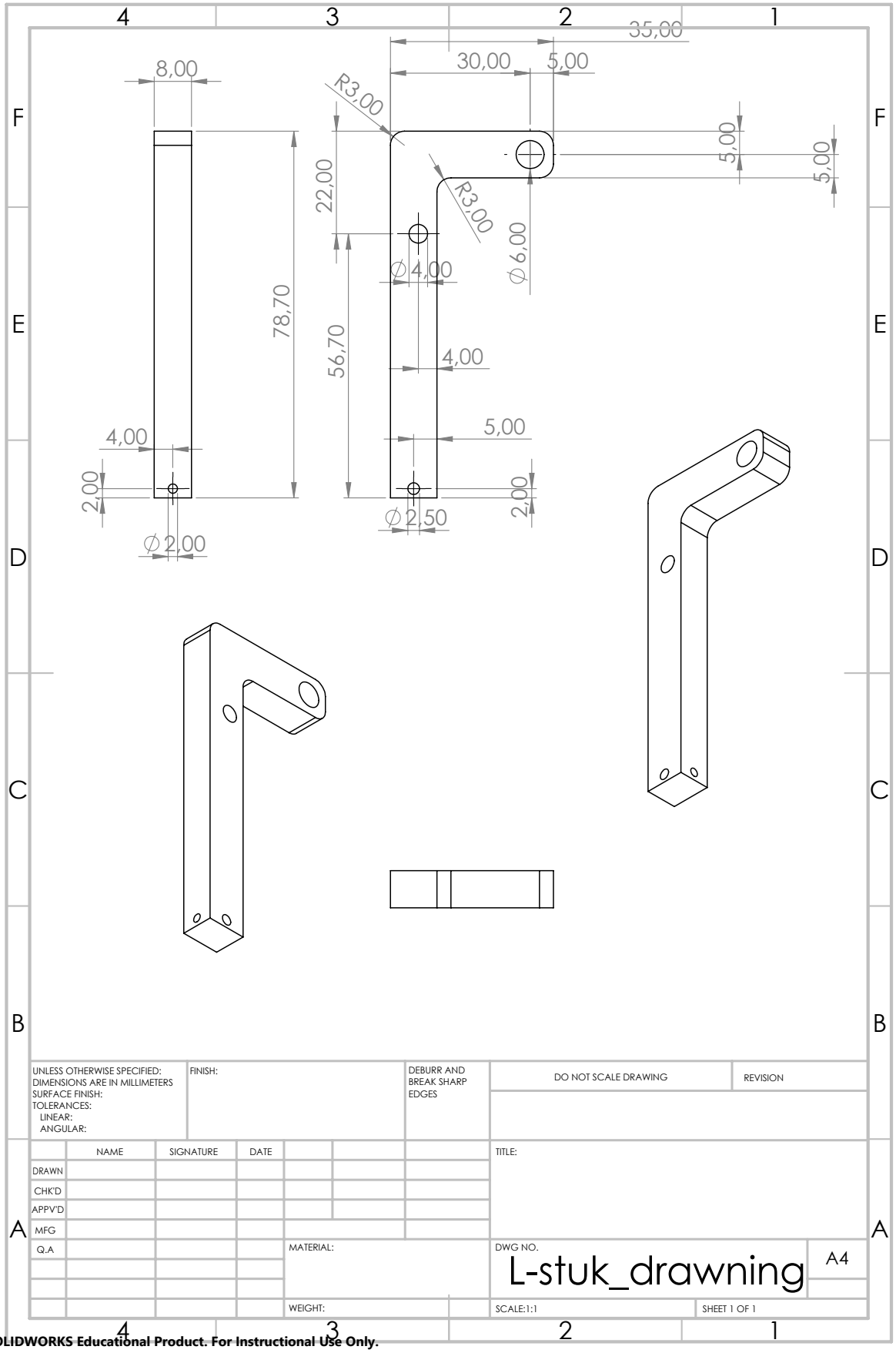

A.2. Load cell

MODEL FLLSB200 S-BEAM Junior Loadcell

Drawing Number: FI1041-C

INCH [mm] | R.O.= Rated Output

WIRING CODE (WC1)

+Excitation	-Excitation	+Signal	-Signal
RED	BLACK	GREEN	WHITE
Shield			
FLOATING			

DESIGNED FOR INLINE LOADING IN TENSION & COMPRESSION
AVAILABLE IN #4-40 AND M3x0.5 METRIC THREADS

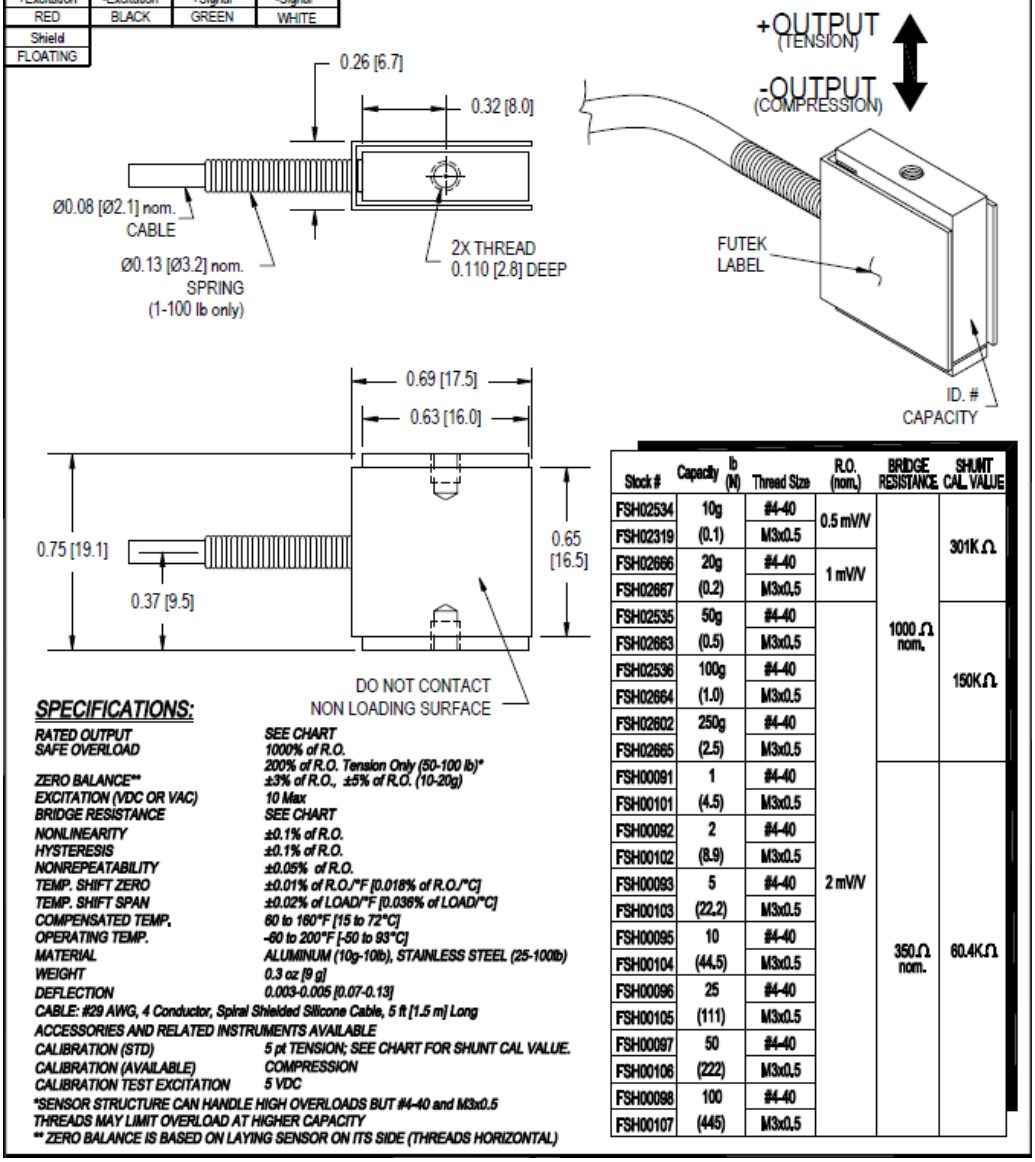

Stock #	Capacity	lb (N)	Thread Size	R.O. (nom.)	BRIDGE RESISTANCE	SHUNT CAL VALUE
FSH02534	10g		#4-40	0.5 mV/V	1000 Ω nom.	301K Ω
FSH02319	(0.1)		M3x0.5			
FSH02666	20g		#4-40	1 mV/V		
FSH02667	(0.2)		M3x0.5			
FSH02535	50g		#4-40	2 mV/V		150K Ω
FSH02663	(0.5)		M3x0.5			
FSH02536	100g		#4-40			
FSH02664	(1.0)		M3x0.5			
FSH02602	250g		#4-40			
FSH02665	(2.5)		M3x0.5			
FSH00091	1		#4-40		350 Ω nom.	60.4K Ω
FSH00101	(4.5)		M3x0.5			
FSH00092	2		#4-40			
FSH00102	(8.9)		M3x0.5			
FSH00093	5		#4-40			
FSH00103	(22.2)		M3x0.5			
FSH00095	10		#4-40			
FSH00104	(44.5)		M3x0.5			
FSH00096	25		#4-40			
FSH00105	(111)		M3x0.5			
FSH00097	50		#4-40			
FSH00106	(222)		M3x0.5			
FSH00098	100		#4-40			
FSH00107	(445)		M3x0.5			

SPECIFICATIONS:

RATED OUTPUT	*SEE CHART*
SAFE OVERLOAD	*1000% of R.O.* *200% of R.O. Tension Only (50-100 lb)**
*ZERO BALANCE***	*±3% of R.O., ±5% of R.O. (10-20g)*
EXCITATION (VDC OR VAC)	*10 Max*
BRIDGE RESISTANCE	*SEE CHART*
NONLINEARITY	*±0.1% of R.O.*
HYSTERESIS	*±0.1% of R.O.*
NONREPEATABILITY	*±0.05% of R.O.*
TEMP. SHIFT ZERO	*±0.01% of R.O./°F [0.018% of R.O./°C]*
TEMP. SHIFT SPAN	*±0.02% of LOAD/°F [0.036% of LOAD/°C]*
COMPENSATED TEMP.	*60 to 160°F [15 to 72°C]*
OPERATING TEMP.	*-60 to 200°F [-50 to 93°C]*
MATERIAL	*ALUMINUM (10g-10lb), STAINLESS STEEL (25-100lb)*
WEIGHT	*0.3 oz [9 g]*
DEFLECTION	*0.003-0.005 [0.07-0.13]*

CABLE: #29 AWG, 4 Conductor, Spiral Shielded Silicone Cable, 5 ft [1.5 m] Long

ACCESSORIES AND RELATED INSTRUMENTS AVAILABLE

CALIBRATION (STD)	*5 pt TENSION; SEE CHART FOR SHUNT CAL VALUE.*
CALIBRATION (AVAILABLE)	*COMPRESSION*
CALIBRATION TEST EXCITATION	*5 VDC*

**SENSOR STRUCTURE CAN HANDLE HIGH OVERLOADS BUT #4-40 and M3x0.5 THREADS MAY LIMIT OVERLOAD AT HIGHER CAPACITY*
*** ZERO BALANCE IS BASED ON LAYING SENSOR ON ITS SIDE (THREADS HORIZONTAL)*

B
Sample fabrication

This appendix includes the files that provide additional information about the fabrication of the samples. The drawings from the mould base, middle and top section are shown in Section B.1, B.2 and B.3 respectively. Section B.4 displays an exploded view of the complete mould assembly. The fibrous part of the samples is represented by Section B.5 - B.8.

B.1. Mould base

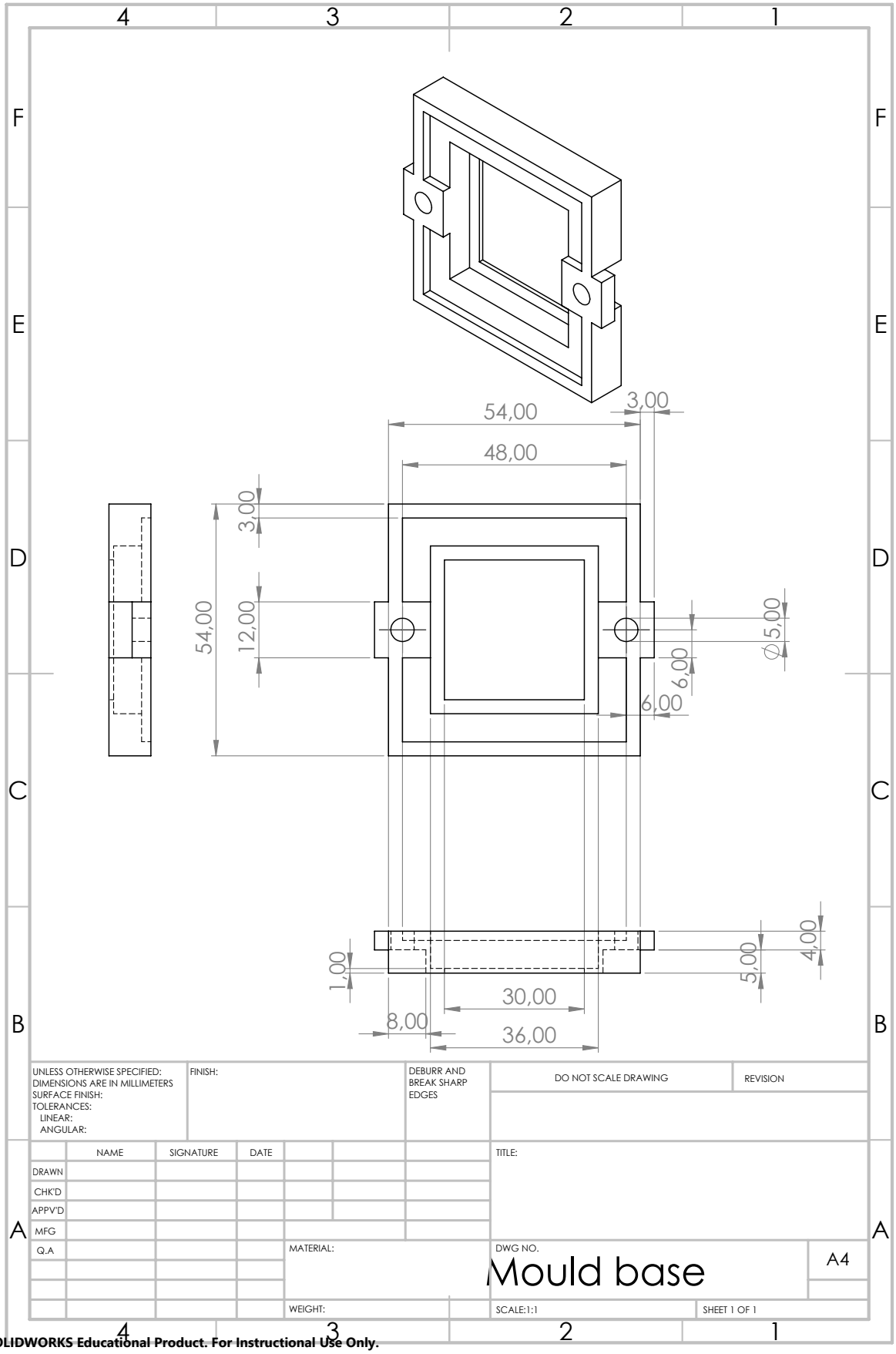

B.2. Mould middle section

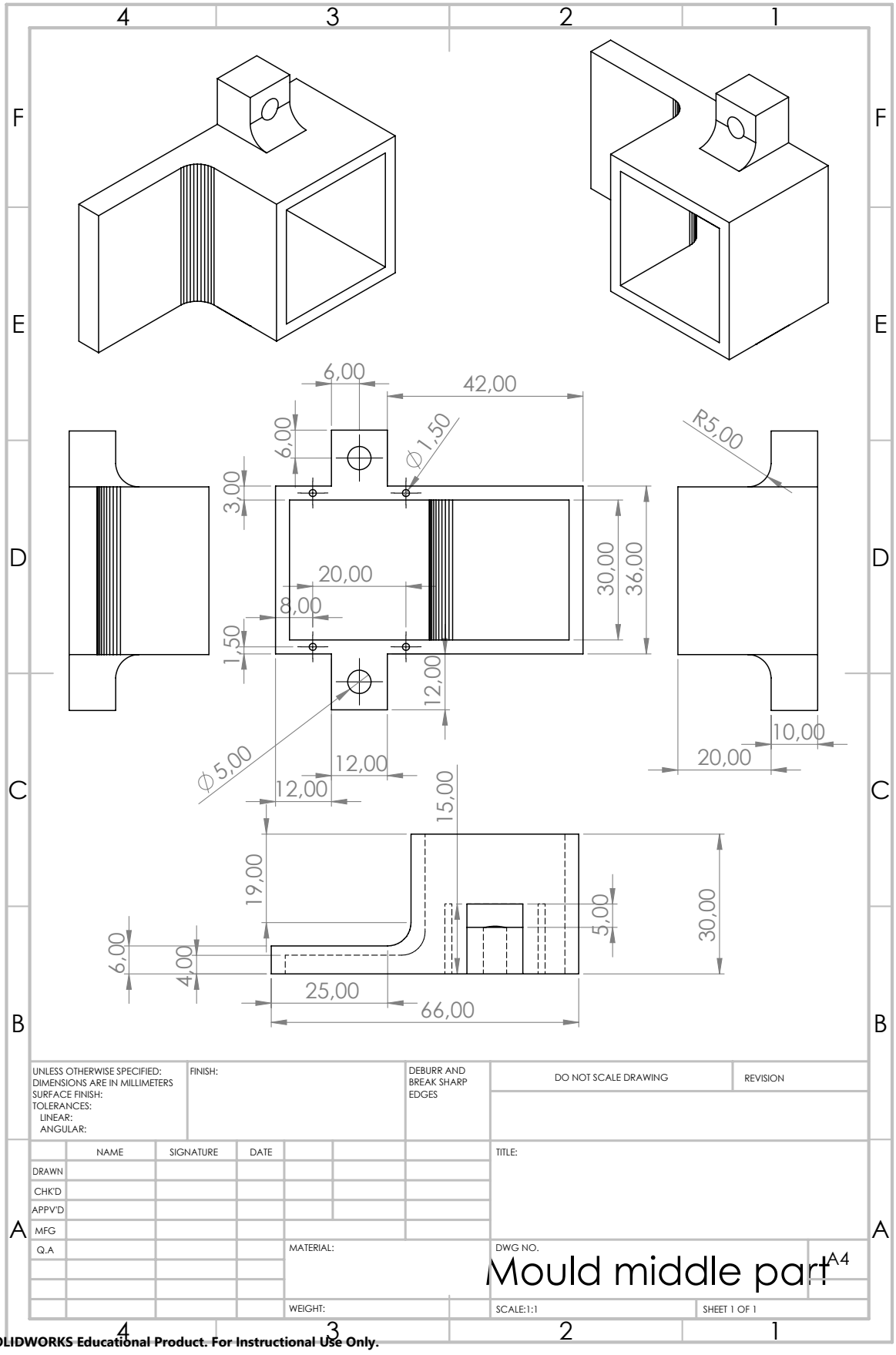

B.3. Mould top section

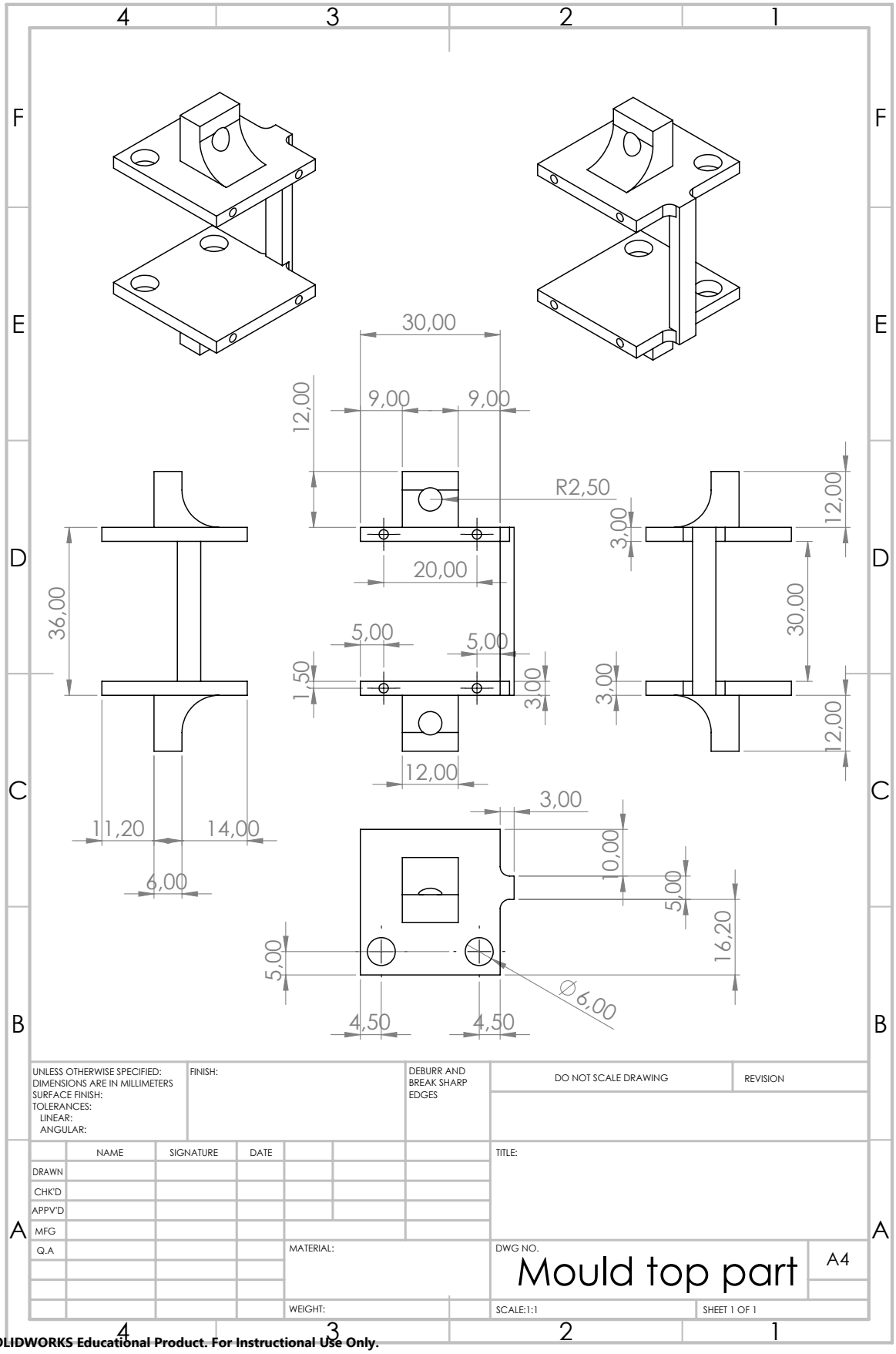

B.4. Mould assembly

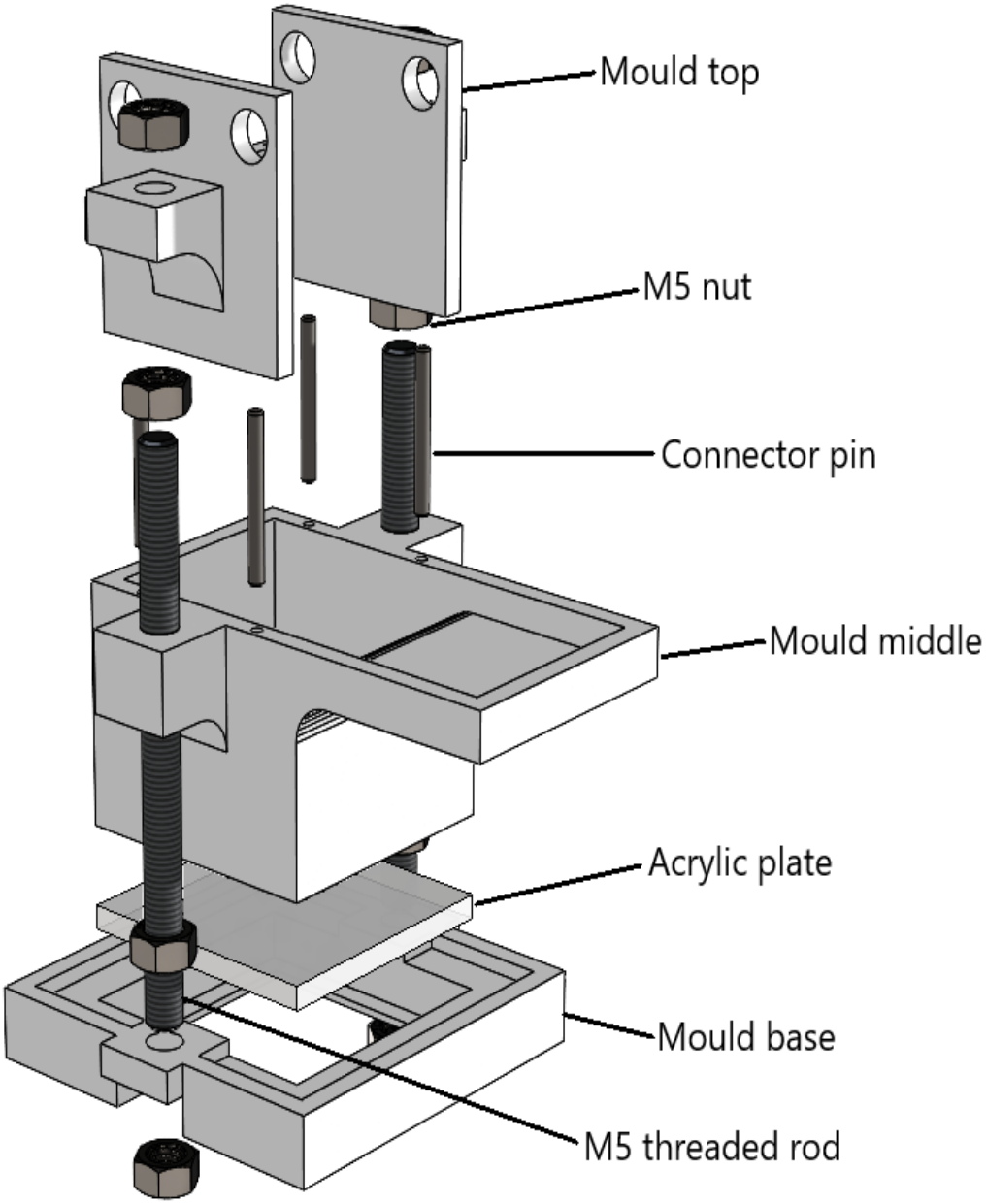

B.5. Spacer with attachment points

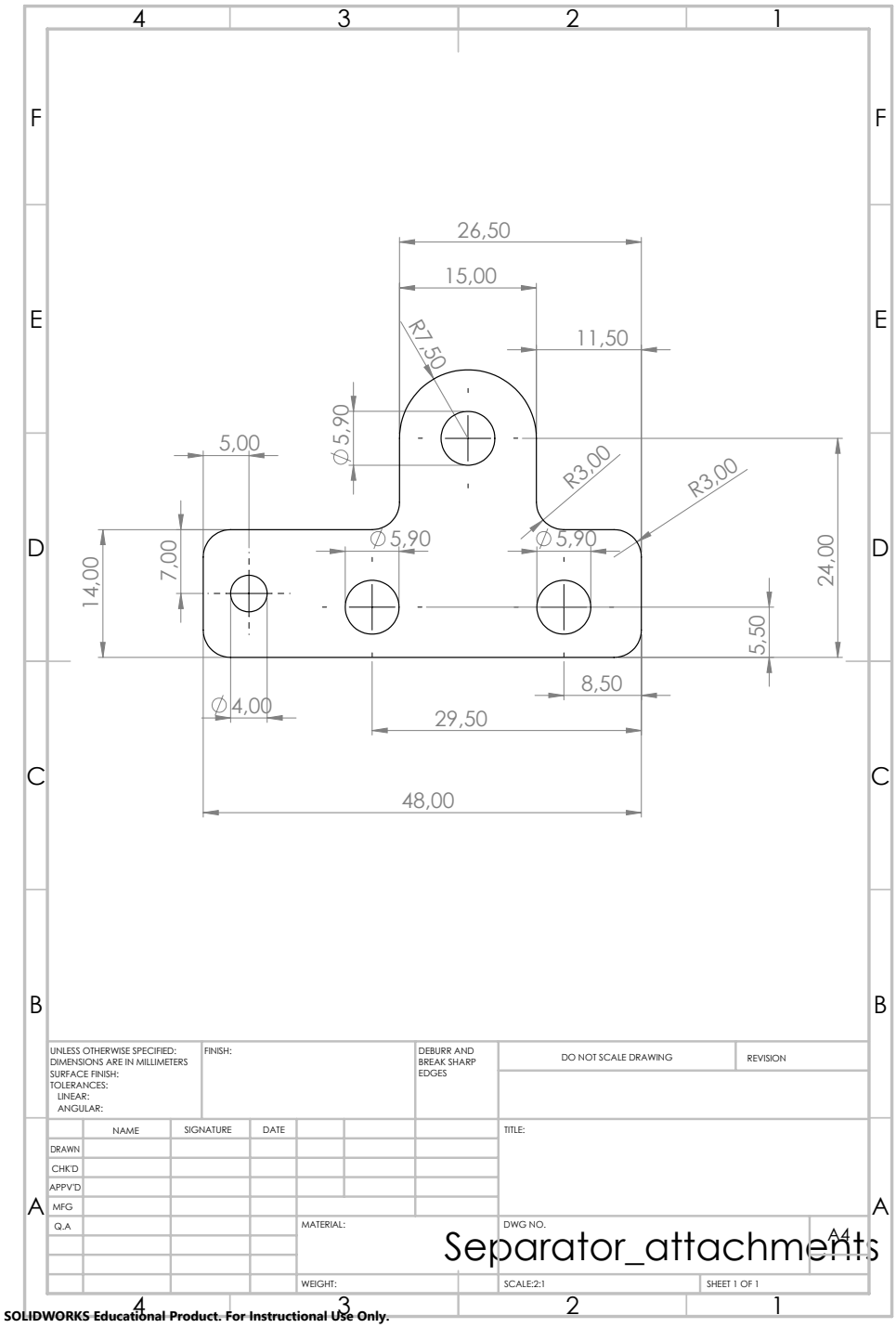

B.6. Spacer standard

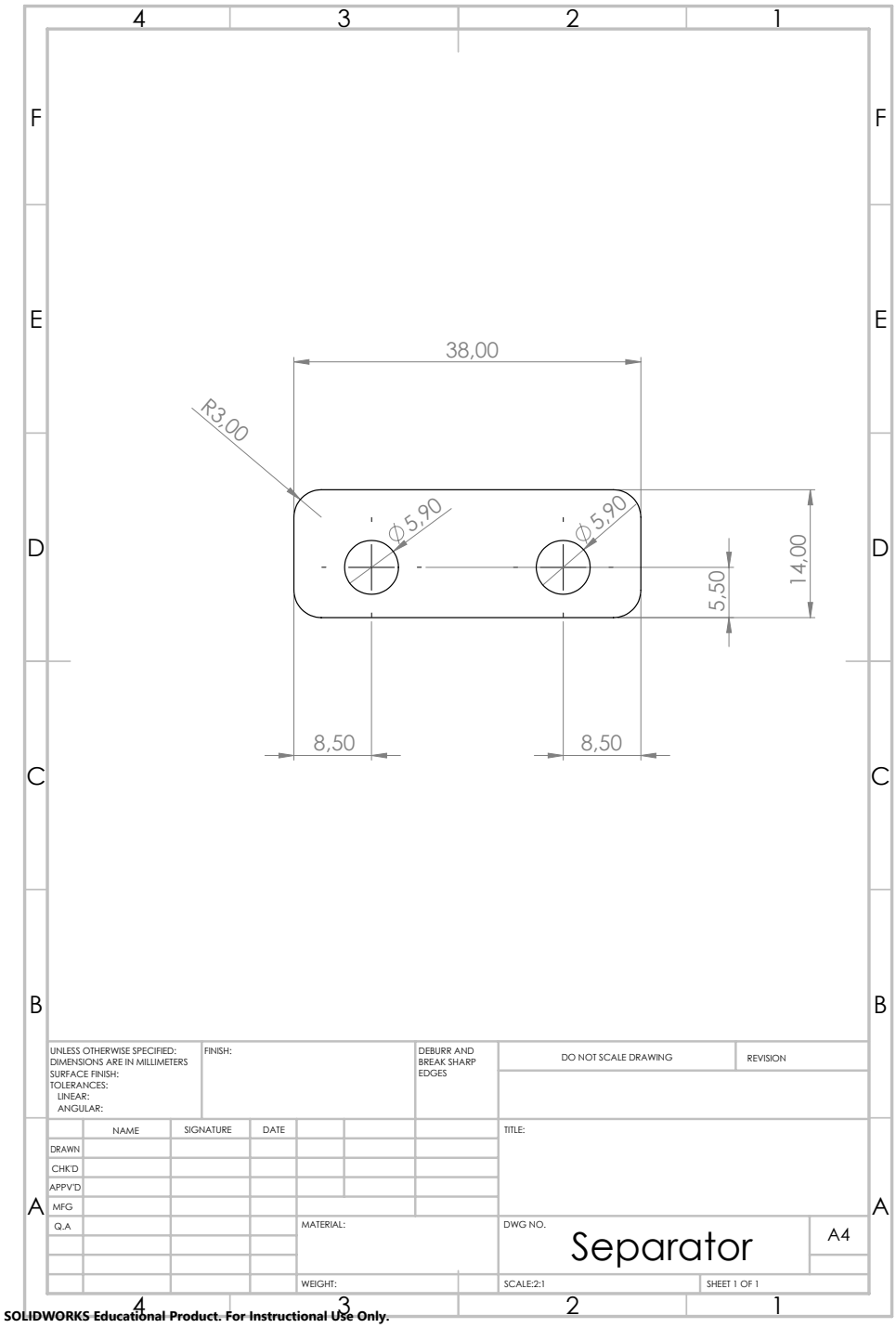

B.7. Part thin fibers

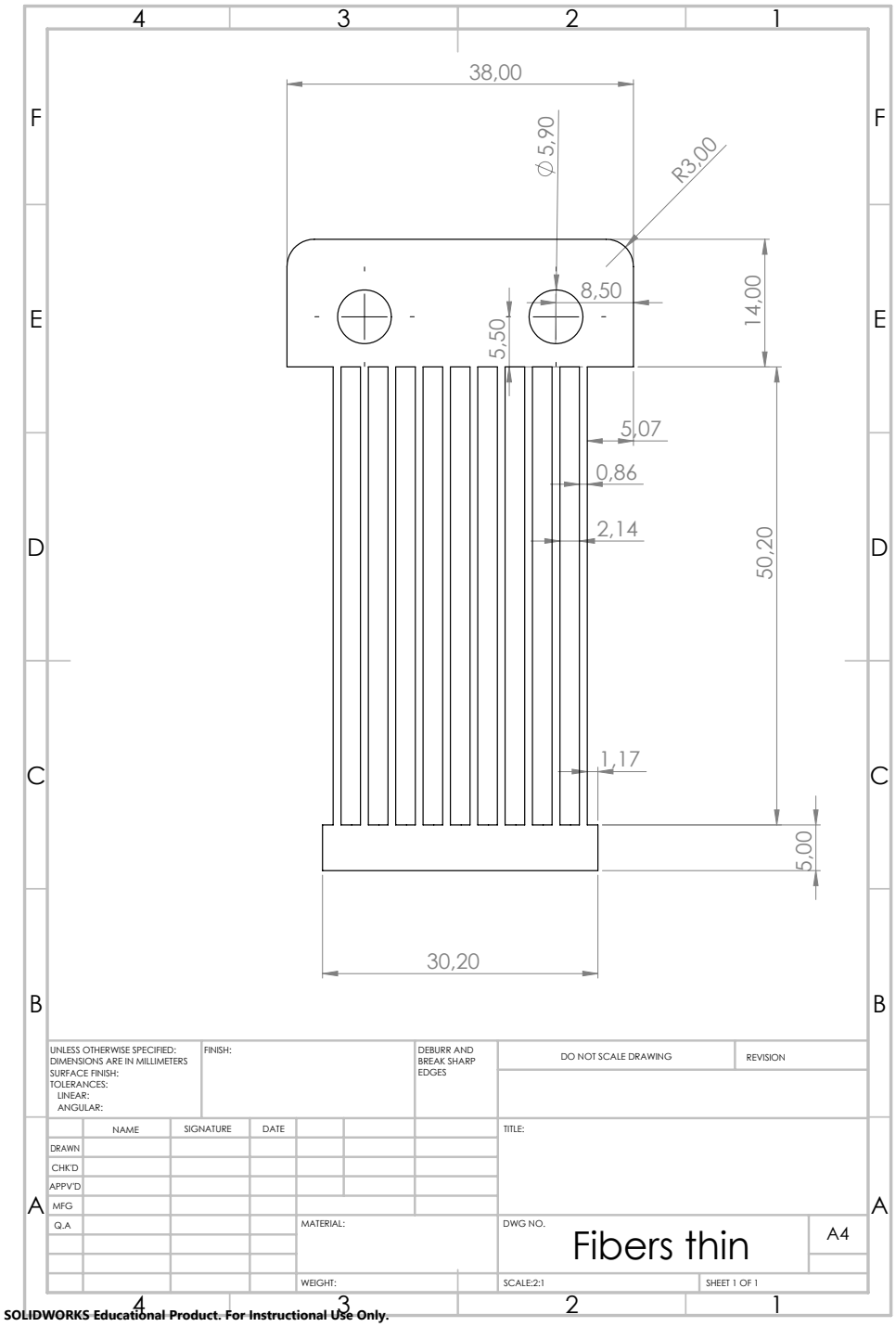

B.8. Part coarse fibers

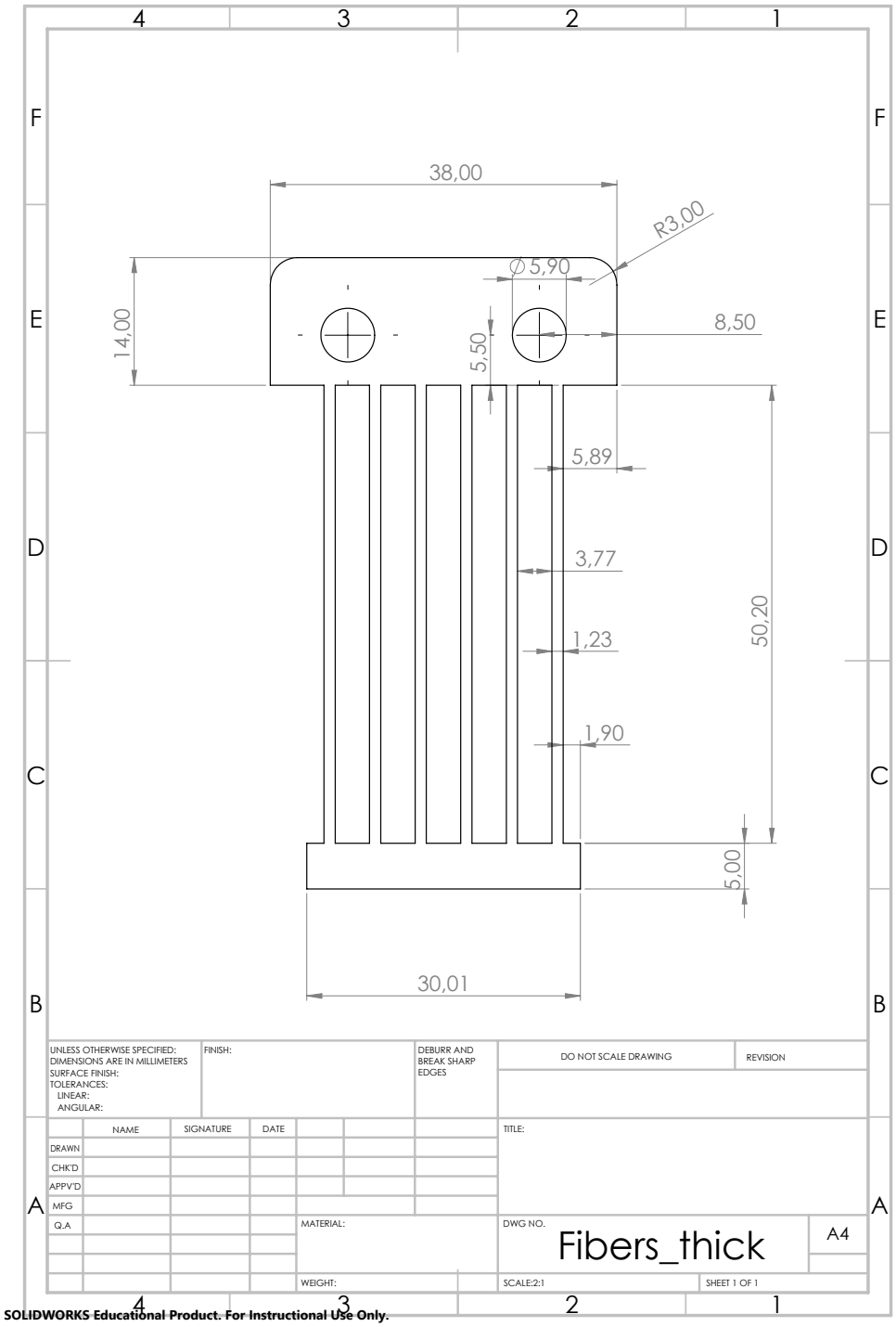

C
Modeling results: model II

This appendix describes the results of model II which is described in Section 2.2.

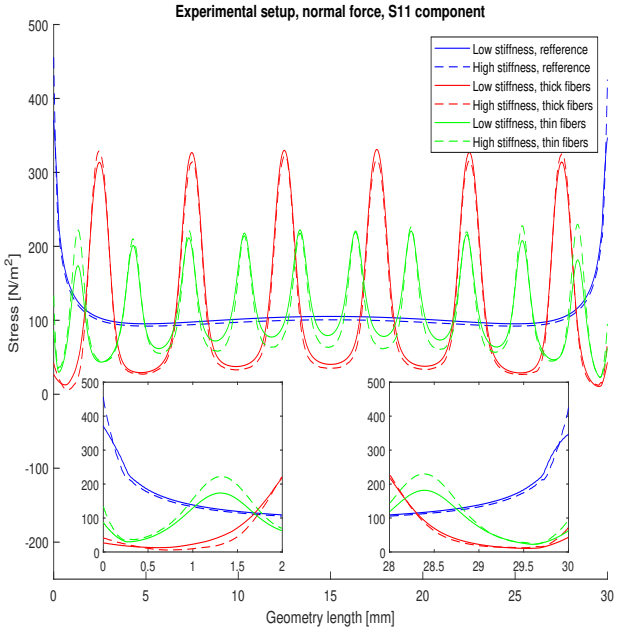

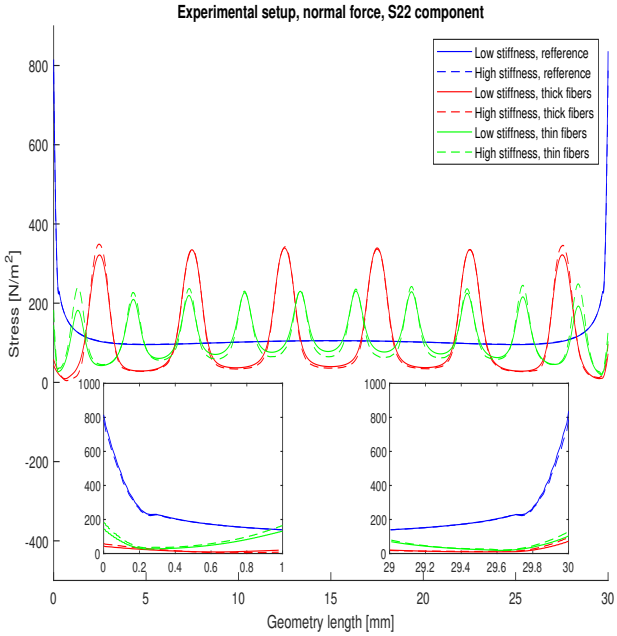

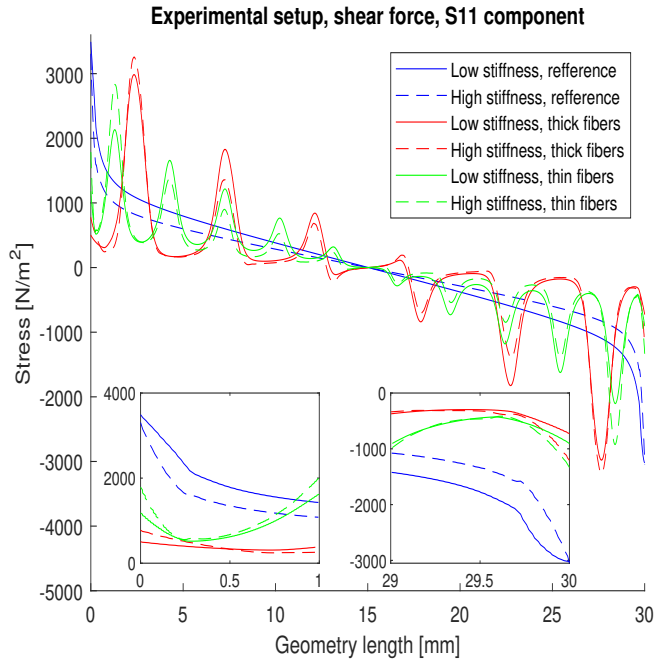
Experimental setup, shear force, S11 component
Low stiffness, refference
High stiffness, refference
Low stiffness, thick fibers
High stiffness, thick fibers
Low stiffness, thin fibers
High stiffness, thin fibers
Stress [N/m^2]
Geometry length [mm]

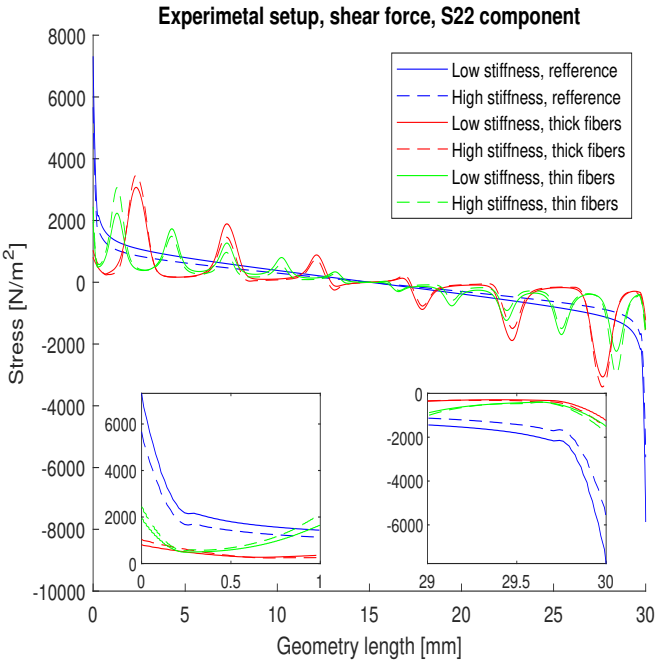
Experimetal setup, shear force, S22 component
Low stiffness, refference
High stiffness, refference
Low stiffness, thick fibers
High stiffness, thick fibers
Low stiffness, thin fibers
High stiffness, thin fibers
Stress [N/m^2]
Geometry length [mm]

D
Data calibration

The calibration of the measured response is necessary to calibrate the measured deformation of the samples as discussed in Section 5.3. The sample deformation is only evaluated for the results of the tangential loading configuration. The calibration is therefore only performed for the measurements for the tangential loading configuration.

The experimental setup shown in Figures 4.3a & 4.3b can be modelled as a system of springs as shown in Figure D.1. The stiffness of the measurement setup is represented by the parameter k_e and the stiffness of the sample is given by the parameter k_s. These two springs are linked in series while an additional spring with stiffness k_p is situated parallel to the other two springs. The total deformation of the measurement setup and the force input are represented by the parameters dL and F respectively.

The stiffness of the measurement setup is expected to be larger than the stiffness of the samples. The stiffness of the parallel component is dependent on the difference in loading between the measurement setup and the sample. An example of such a difference is friction in the pulley used for the tangential loading which causes lower force transfer between the pulley and the sample compared to the force transfer between the pulley and the translational stage. These effects, however, are not expected to play a large role. The system shown in Figure D.1 can therefore be reduced to a system in which two springs are present with stiffness k_s and k_e. These springs are connected in series.

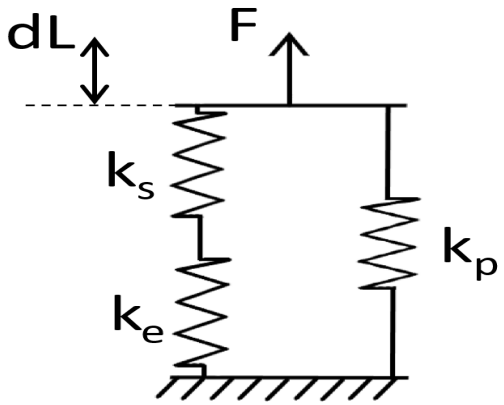

Figure D.1: Schematic representation of the resistance to deformation of the experimental setup with k_s for the stiffness of the sample and k_e for the stiffness of the measurement setup. k_p represents a parallel stiffness which directly couples the force input(F) with the displacement(dL).

The response of the total system can be calculated with the relations shown in Equations D.1 - D.3. The value of parameter k_e is calculated using calibration data. The calibration data is measured using the experimental setup in which the wire is not connected to a sample but instead, directly attached to the aluminium frame. The data measured using this setup contains a displacement S_{cal} and a force F_{cal}.

$$k_e = \frac{\delta S_{cal}}{\delta F_{cal}} \tag{D.1}$$

The stiffness of the sample can be calculated from the measured response obtained with the testing configurations. The stiffness of the 'raw' measured data(k_{raw}) is calculated with the relation shown in Equation D.2 which uses the measured 'raw' displacement and force response which are represented by S_{raw} and F_{raw} respectively. The stiffness of the sample, k_s can be calculated using the relation from Equation D.3.

$$k_{raw} = \frac{\delta S_{raw}}{\delta F_{raw}} \tag{D.2}$$

$$k_s = \frac{1}{\frac{1}{k_{raw}} - \frac{1}{k_e}} \tag{D.3}$$

Figure D.2 shows the result of the calibration of the data. The calculated response of the sample shows a higher sample stiffness than the stiffness of the measured response which can be explained with the stiffness of the experimental setup. The experimental setup stiffness is higher than the sample stiffness but does still influence the total system response since the stiffness of the sample and the setup are in series.

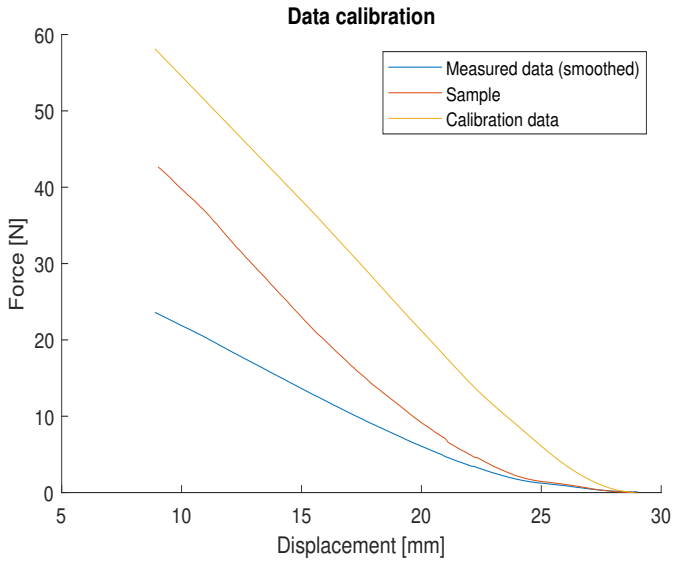

Figure D.2: Force-displacement relations for the calibration data, the 'raw' measured data and for the calculated sample response. The stiffness is derived from the slopes of the curves in this figure as shown in Equations D.1 & D.2.

E
Sample detachment & deformation

This appendix provides images taken from different angles from the samples for different loading configurations. The first section shows the development of the detachment at the sample-substrate interface and the second section shows the deformation of the samples for the friction force measurements.

E.1. Sample detachment

E.1.1. Adhesion force measurements

- **Sample *R_1MPa***: detachment started in the bottom left and the top right corner and grew from the corners inwards until full detachment was reached.
- **Sample *C_1MPa***: detachment was first observed at a few locations below the fibres in the middle of the interface. Detachment occurred when the detached zones merged. The detachment process was relatively quick compared to the detachment process of the reference samples which showed a more gradual detachment pattern with very clear detachment boundaries.
- **Sample *T_1MPa***: detachment was observed to start at the fibre tips in the lower left corner of the geometry. From there, the detachment developed through the interface. It was observed that detachment always occurred first at the fibre tips for this sample.
- **Sample *R_3MPa***: initial detachment was observed at the right edge of the interface. The detachment boundary traveled from left to right along the interface until full detachment occurred.
- **Sample *c_3MPa***: initial detachment was observed below the fibres in the right top edge of the geometry. From there, the detachment developed relatively quick as described above for sample *C_1MPa*.
- **Sample *T_3MPa***: for this sample, the influence of the individual fibres on the detachment boundary was observed as described for the other fibrous samples. The influence of individual fibres, however, was less pronounced than was observed for samples *C_1MPa* and *T_1MPa*.

The detachment of the 1 MPa matrix stiffness samples for adhesion force measurements is shown in Figures E.1, E.2 and E.3. The detachment of samples *R_1MPa*, *T_1MPa* and *C_3MPa* for friction force measurements is shown in Figures E.4, E.5 and E.6. All samples showed surface degradation in the form of some PDMS residue left on the substrate after sample detachment as shown in Figure E.6.

E.1.2. Friction force measurements

- **Sample *R_1MPa***: a gradual detachment was observed which started from the opposite edge from the pulling site. The detachment grew from a small disconnected zone at the left bottom which was not attached to the substrate from the start of the measurement. The detachment gradually grew until about half of the interface was disconnected from the substrate after which full detachment occurred.
- **Sample *C_1MPa***: initial detachment was observed in the middle of the interface. The stress then developed through the interface until it reached the interface edges.
- **Sample *T_1MPa***: detachment was first observed at the fibre tips of some fibres in the top left corner of the interface. The detachment than developed inward until full detachment occurred when the detachment reached the edges of the interface. The lower left corner of the sample was observed to be detached from the substrate from the start of the measurement. This partial detachment did not considerably influence the sample performance since the detachment was not observed to develop from this location.

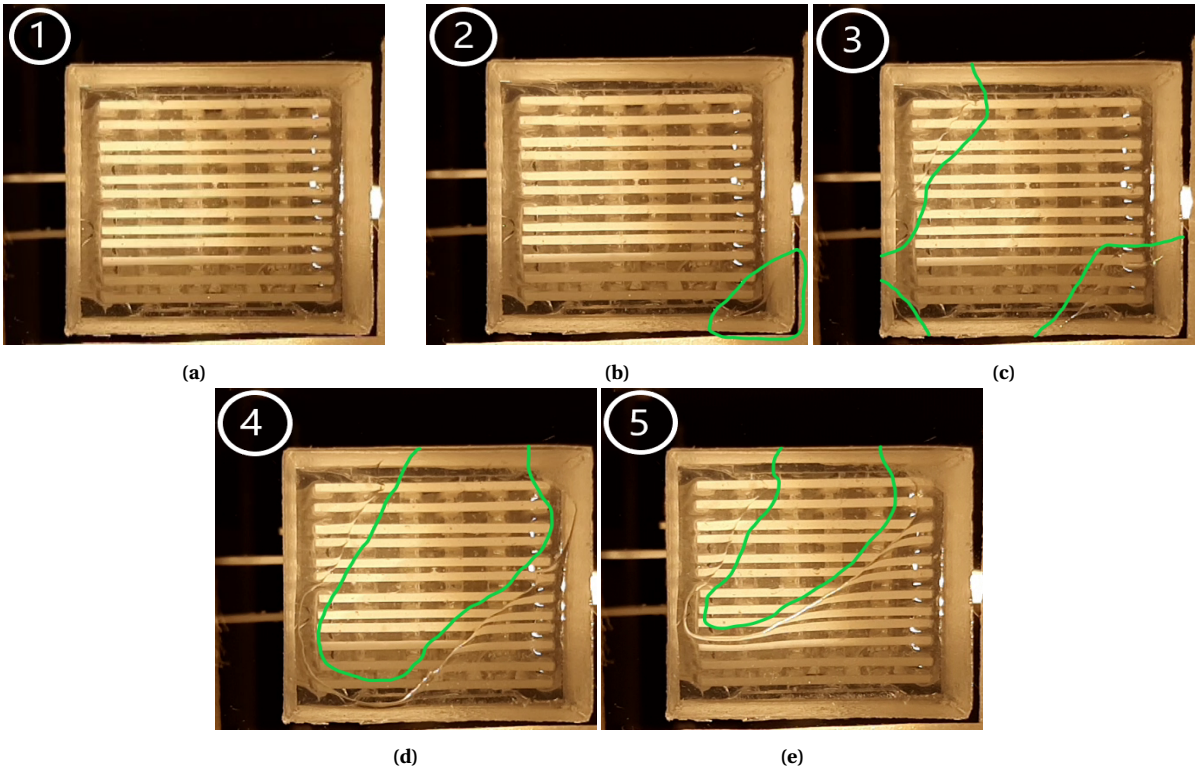

Figure E.1: The detachment of sample *R_1MPa* for normal loading condition in steps. The detachment boundaries are visualised with the green lines. Figure E.1a shows the unloaded sample and Figures E.1b - E.1e show the development of the detachment of the sample from the substrate.

- **Sample *R_3MPa***: the detachment of this sample was very similar to the detachment of sample *R_1MPa*.
- **Sample *C_3MPa***: detachment started under the fibres in the left half of the interface. The detached areas under these fibres expanded and than merged with each other. Total detachment was observed when the detachment reached the edge of the geometry on the pulling side.
- **Sample *T_3MPa***: initial detachment was observed below the fibres in the top right corner. The detachment grew from that point until full detachment was observed.

It is shown in Figures E.5 & E.6 that the detachment for the fibrous samples was initiated at the fibre tips. There was no sign of a direct peeling effect which would have caused an increase in the stress at the edge opposite to the L-shaped attachment piece used for the friction force measurements.

E.2. Sample deformation

The samples showed considerable deformation for for the friction force measurements. The fibrous samples displayed less resistance to deformation than the reference samples. The largest deformation was observed for sample *T_1MPa* and the smallest deformation was observed for sample *R_3MPa*. The deformation for samples *R_1MPa*, *C_1MPa* and *T_1MPa* is shown in Figures E.7a, E.7b and E.7c. The deformation in these figures is the deformation of the samples just before separating from the substrate.

The friction force measurement setup was sensitive for the development of peeling effects due to the indirect application of the load. The L-shaped attachment piece was developed to prevent the development of a moment at the sample-substrate interface. The effectiveness of this attachment piece was confirmed with the observation of no direct peeling effect. Due to the compliance of the fibres, however, an indirect peeling effect was observed for large deformations of the fibrous samples as shown in Figure E.8.

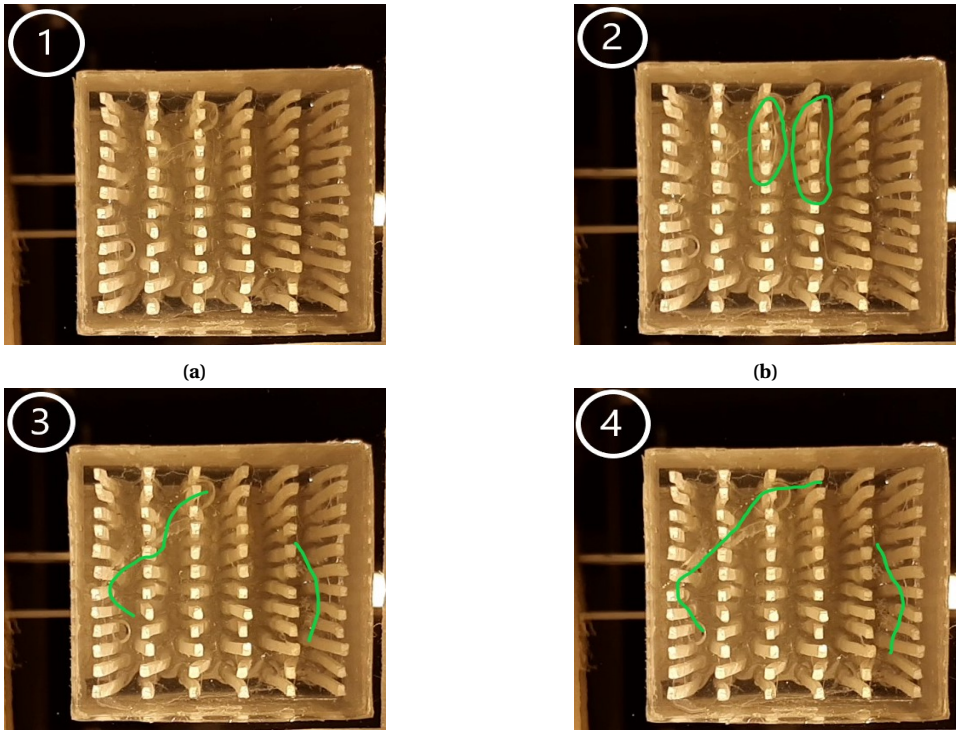

(a) (b)

(c) (d)

Figure E.2: The detachment of sample *C_1MPa* for normal loading condition in steps. The detachment boundaries are visualised with the green lines. Figure E.2a shows the unloaded sample and Figures E.2b - E.2d show the development of the detachment of the sample from the substrate.

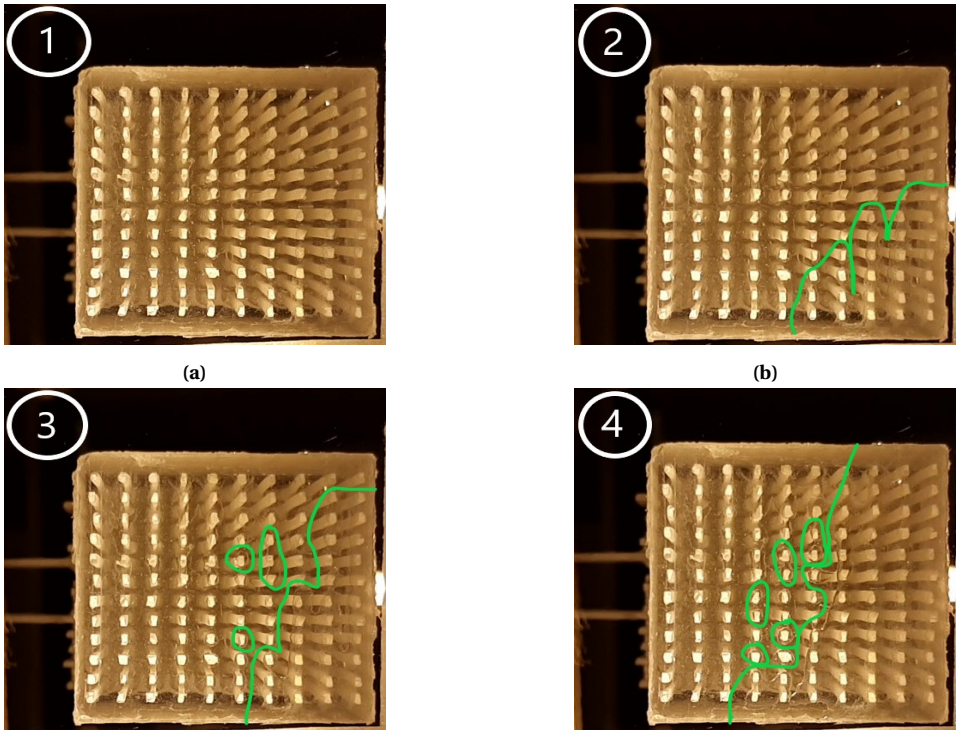

(a) (b)

(c) (d)

Figure E.3: The detachment of sample *T_1MPa* for normal loading condition in steps. The detachment boundaries are visualised with the green lines. Figure E.3a shows the unloaded sample and Figures E.3b - E.3d show the development of the detachment of the sample from the substrate.

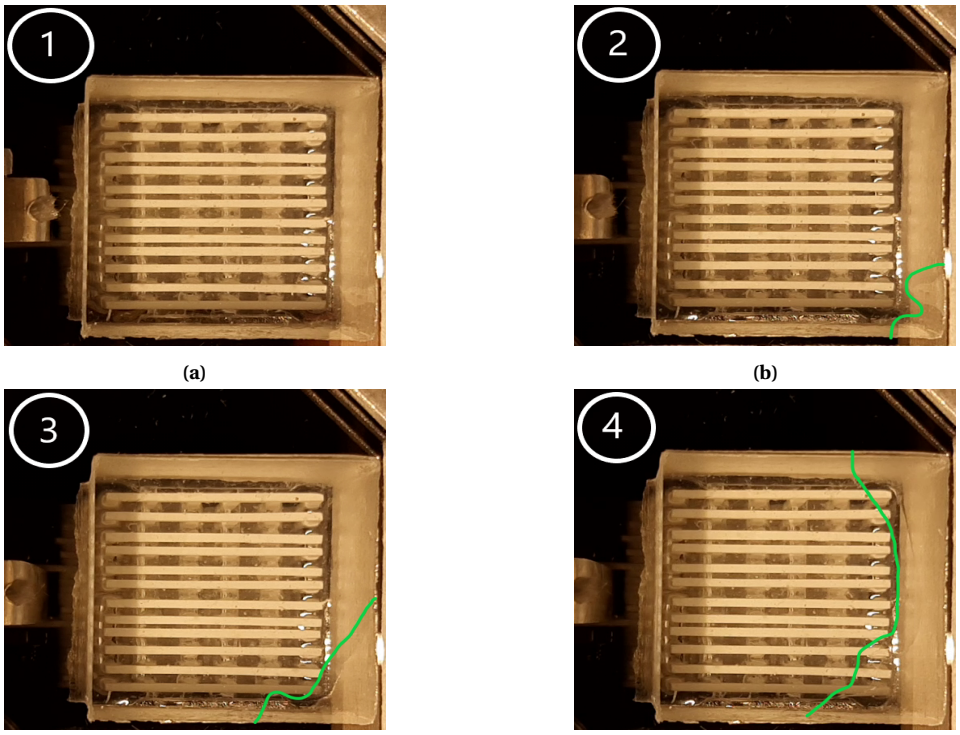

(a) **(b)**

(c) **(d)**

Figure E.4: The detachment of sample *R_1MPa* for the friction force measurements in steps. The detachment boundaries are visualised with the green lines. Figure E.4a shows the unloaded sample and Figures E.4b - E.4d show the development of the detachment of the sample from the substrate.

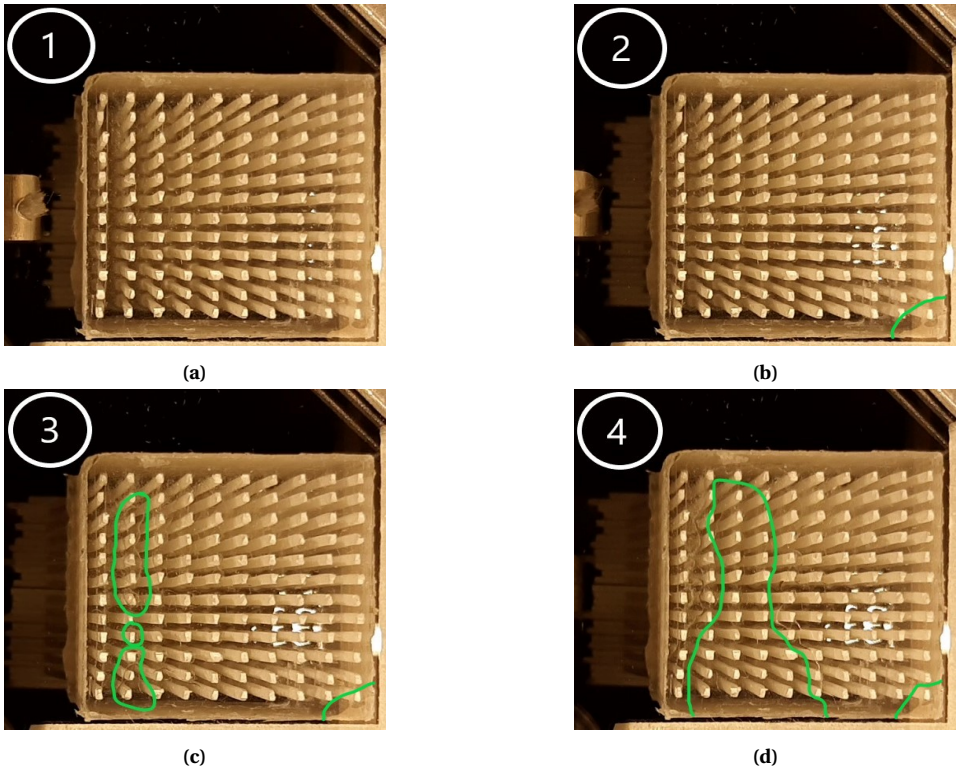

(a) **(b)** **(c)** **(d)**

Figure E.5: The detachment of sample *T_1MPa* for the friction force measurements in steps. The detachment boundaries are visualised with the green lines. Figure E.5a shows the unloaded sample and Figures E.5b - E.5d show the development of the detachment of the sample from the substrate. The detached zone in the lower right corner of the interface did not grow with the increasing load which showed that the stress below the fibres in the left-mid area of the interface was considerably higher than the stress in the lower right corner of the interface.

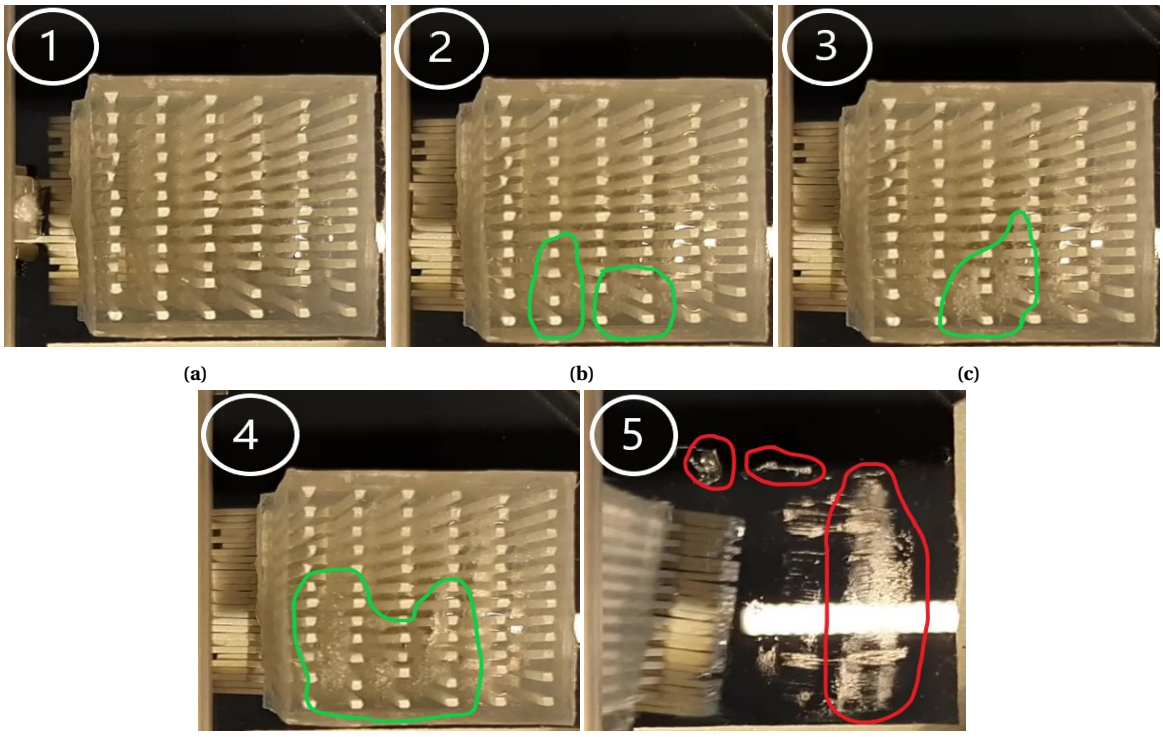

(a) (b) (c)

(d) (e)

Figure E.6: The detachment of sample *C_3MPa* for the friction force measurements in steps. The detachment boundaries are visualised with the green lines. Figure E.6a shows the unloaded sample and Figures E.6b - E.6e show the development of the detachment of the sample from the substrate. The sample degradation is shown in Figure E.6e. The PDMS residue left on the substrate after sample detachment is highlighted with the red lines.

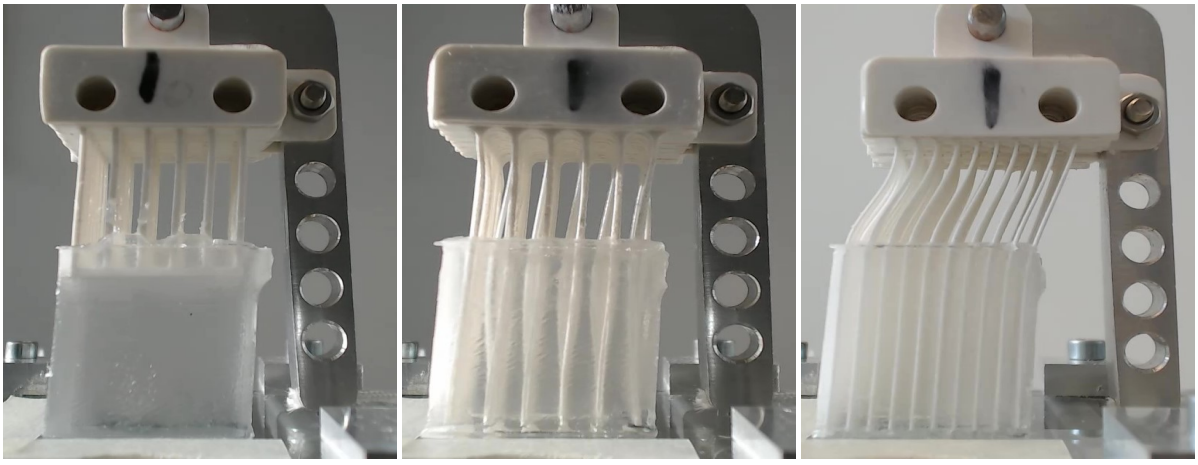

(a) (b) (c)

Figure E.7: The deformation for friction force measurements for samples *R_1MPa*, *C_1MPa* and *T_1MPa* in Figure E.7a, E.7b and E.7c respectively. The fibrous samples had a lower resistance to deformation compared to the reference samples. The sample with the thin fibres had the lowest resistance to deformation.

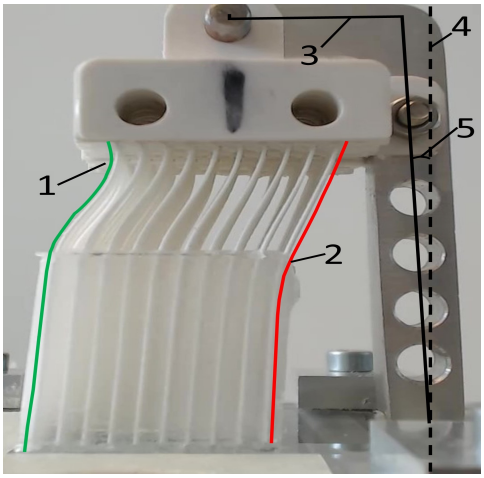

Figure E.8: A peeling effect developed in sample *T_1MPa* for friction force measurements. Due to the asymmetric nature of the applied load and backlash in the assembly of the sample and the attachment piece, the L-shaped attachment piece deviated from the vertical (4). The angle (5) between the centerline (3) of the attachment piece and the vertical caused tension in the fibres close to the attachment piece (2). The fibres at the opposite side (1) were loaded in compression.